MULTI-PHYSICS MODELING OF PHOTOVOLTAIC MODULES AND ARRAYS WITH AUXILIARY THERMAL COLLECTORS

BY

MUHAMMAD USAMA SIDDIQUI

A Thesis Presented to the
DEANSHIP OF GRADUATE STUDIES

KING FAHD UNIVERSITY OF PETROLEUM & MINERALS
DHAHRAN, SAUDI ARABIA

In Partial Fulfillment of the
Requirements for the Degree of

MASTER OF SCIENCE
In
MECHANICAL ENGINEERING

DECEMBER 2011

KING FAHD UNIVERSITY OF PETROLEUM & MINERALS
DHAHRAN, SAUDI ARABIA

DEANSHIP OF GRADUATE STUDIES

This thesis, written by **Muhammad Usama Siddiqui** under the direction of his thesis advisor and approved by his thesis committee, has been presented to and accepted by the Dean of Graduate Studies, in partial fulfillment of the requirements for the degree of **MASTER OF SCIENCE in MECHANICAL ENGINEERING**.

Thesis Committee

Thesis Advisor
Prof. Dr. Abul Fazal M. Arif

Member
Prof. Dr. Syed M. Zubair

Department Chairman
Prof. Dr. Amro M. Al-Qutub

Member
Dr. Khaled Saleh Al-Athel

Dean of Graduate Studies
Dr. Salam A. Zummo

2/1/12
Date

Dedicated to my mother, my mother, my mother, my father, my sister and my teachers

ACKNOWLEDGEMENTS

In the Name of Allah, the Most Beneficent, the Most Merciful.

> Praise belongs to Allah, the Lord of all the worlds (2) The All-Merciful, the Very-Merciful. (3) The Master of the Day of Requital. (4) You alone do we worship, and from You alone do we seek help. (5) Take us on the straight path (6) The path of those on whom You have bestowed Your Grace, Not of those who have incurred Your wrath, nor of those who have gone astray. (7)
>
> Al-Fatiha

I begin with the name of Allah, the most beneficent, the most merciful. May Allah bestow peace on our beloved Prophet Mohammed (*peace and blessings of Allah be upon him*), and his family. I would not have able to complete this work without the help of Allah who endowed me with health, courage, aptitude and patience.

During this work my parents were a constant source of motivation and support. Their prayers, love and encouragement helped me to arrive at this milestone. I would like to thank my teacher Mr. Sagheer Ahmed. The things I learnt with him are some of the most important lessons of my life.

Acknowledgements are due to *King Fahd University of Petroleum and Minerals* which gave me the opportunity to pursue a graduate degree and also for all the support I received in carrying out this research. I am also grateful to the *Center for Clean Water and Clean Energy* at *KFUPM* (DSR project # R6-DMN-08) and *MIT* for its support during this research.

I would like to express my gratitude to my thesis advisor Prof. Abul Fazal M. Arif for all he taught me, for his patience when I couldn’t get things done and for his help when I needed it. I am also very thankful to my thesis committee members Prof. Syed M. Zubair and Dr. Khaled Saleh Al-Athel for their involvement and encouragement. I would also like to thank Prof. Anwar K. Sheikh and Prof. Moustafa Elshafei for their helpful comments during the development of this work. I would also like to thank Prof. Steven Dubowski from MIT for his helpful comments during this work.

Special thanks to my friend Shoieb Arshad for all the “technical resources” he provided without which this work would not have been possible. Thanks also to Syed Faraz Ahmed for introducing me to the wonderful reference management system *Mendeley*. It has helped me a lot. Thanks also to all my colleagues in the Mechanical Engineering department for making my time in ME graduate room memorable.

TABLE OF CONTENTS

LIST OF TABLES .... **xi**

LIST OF FIGURES .... **xiii**

THESIS ABSTRACT (ENGLISH) .... **xviii**

THESIS ABSTRACT (ARABIC) .... **xix**

CHAPTER 1 INTRODUCTION **1**

- 1.1 Introduction to Photovoltaics 2
  - 1.1.1 Working of PV cells 2
  - 1.1.2 PV Cells, Modules and Arrays 3
  - 1.1.3 PV Cell Technologies 4
  - 1.1.4 Electrical Performance of PV Systems 4
  - 1.1.5 Modeling of Photovoltaic Modules and Arrays 5
- 1.2 Motivation behind Present work 6
- 1.3 Objectives of Current Work 8

CHAPTER 2 LITERATURE REVIEW **9**

- 2.1 Radiation Modeling 9
- 2.2 Electrical Modeling 10
- 2.3 Thermal Modeling 17
- 2.4 Structural Modeling 24

CHAPTER 3 ELECTRICAL MODELING **28**

- 3.1 Electrical Modeling of PV Modules 28
  - 3.1.1 Temperature and Radiation Scaling of Reference Measurements 29

3.1.2 Interpolation of I-V curves 30

3.1.3 Empirical Derivation of Correlations 30

3.1.4 Electric Circuit Modeling 31

3.2 Five Parameters Model 31

3.3 Parameters Estimation for Five Parameters Model using Multivariable Optimization 35

3.4 Electrical Models Selected for Comparison 37

3.4.1 Four Parameter PV Model 37

3.4.2 Sandia Labs PV Model 39

3.4.3 Villalva et al. Electric Circuit Model 41

3.5 Comparison of Electrical Models 43

3.5.1 Selected PV modules 43

3.5.2 Error Statistics 47

3.5.3 Parameters Calculation for the Selected Modules 47

3.5.4 Comparison of Electrical Models - Results 52

3.6 Sensitivity Analysis of 5 Parameter Model 55

3.7 Proposed Seven Parameter Electrical Model 58

3.7.1 Comparison of Proposed Seven Parameters Model with Other Models 62

3.8 Conclusions 66

CHAPTER 4 RADIATION AND OPTICAL MODELING 68

4.1 Introduction 68

4.2 Radiation & Optical Modeling 68

4.2.1 Optical Model 69

4.2.2 Radiation Models 69

4.3 Comparative study of radiation & optical models 72

4.3.1 Results and Discussion 74

4.3.2 Conclusions 81

CHAPTER 5 THERMAL MODEL 82

5.1 Thermal Modeling of PV modules 82

5.1.1 Governing Equations 83

5.1.2 Thermal Load and Boundary Conditions 85

5.1.3 Implementation of the Thermal Model for PV Panel without Cooling 87

5.1.4 Implementation of the Thermal Model for PV Panel with Cooling 89

5.2 Model Validation 90

5.2.1 Validation of Thermal Model without Cooling using Experimental Data 90

5.2.2 Validation of Thermal Model without Cooling using Manufacturer Data 93

5.2.3 Validation of Thermal Model with Cooling using Analytical Model............. 94

5.3 Parametric study - PV performance under varying atmospheric and operating conditions 94

5.3.1 Effect of Absorbed Solar Radiation on Panel Performance............................ 99

5.3.2 Effect of Ambient Temperature on Panel Performance................................ 101

5.3.3 Effect of Heat Exchanger Inlet Conditions... 103

5.3.4 Effect of Thermal Contact Resistance 105

5.3.5 Conclusion 106

CHAPTER 6 STRUCTURAL MODEL 107

6.1 Structural model.. 107

6.1.1 Implementation of Structural Model for PV Panel without Cooling............. 109

6.1.2 Implementation of structural model for cooled PV panel............................. 110

6.2 Paramteric study – Structural Performance Under Varying Atmospheric and Operating Conditions... 111

6.2.1 Conclusion 121

CHAPTER 7 MULTIPHYSICS MODEL AND TRANSIENT ANALYSIS......... 122

7.1 Overal Multi-Physics Model.. 122

7.2 Transient Analysis 125

7.2.1 Results and Discussion 127

7.2.2 Conclusions.. 148

CHAPTER 8 AUXILIARY THERMAL COLLECTOR DESIGN FOR PHOTOVOLTAIC PANEL COOLING.. 149

8.1 Introduction... 149

8.2 Performance Metrics.. 151

8.2.1 Average surface temperature 151

8.2.2 Surface Temperature Non-Uniformity.. 151

8.2.3 Heat Transfer per unit Pumping Power 152

8.3 Basic heat exchanger confiruation considered...................................... 153

8.4 Effect of Variation of Design Parameters... 154

8.4.1 Effect of number of channels... 155

8.4.2 Effect of width of header 155

8.4.3 Effect of tapered arrangement of channels 158

8.4.4 Effect of position of inlet and outlet 160

8.4.5 Effect of Series-Parallel Combinations 167

8.5 Summary of Results 169

8.6 Selection of Best Channel Layout Designs based on Performance Metrics 175

8.7 Conclusions 179

CHAPTER 9 CONCLUSIONS AND RECOMMENDATIONS 181

NOMENCLATURE 184

REFERENCES 189

VITAE 196

LIST OF TABLES

Table 3.1. Electrical characteristics of the selected modules at STC. 44

Table 3.2. Extracted I-V points for crystalline silicon modules. 45

Table 3.3. Extracted I-V points for thin film modules... 46

Table 3.4. Parameters for the Five Parameter Model (Proposed) at STC......................... 48

Table 3.5. Parameters for the Four Parameter Model at STC.. 48

Table 3.6. Parameters for Villalva et al. Model at STC... 49

Table 3.7. Parameters for the Sandia Labs PV Model... 50

Table 3.8. Normalized Sensitivity Analysis results for the Five Parameter Model.......... 56

Table 3.9. Modifications to translation equations for I_L and a. 59

Table 3.10. Module information required for parameters m and n.................................. 61

Table 3.11. Effect of the translation equations modification on maximum power prediction accuracy (RMSE)... 61

Table 3.12. Parameters m and n for the selected PV modules... 62

Table 4.1: STC Reference Parameters for SAPC-165 PV Module 74

Table 4.2. Reference Parameters for SAPC-165 PV Module for 600 W/m^2 absorbed radiation 81

Table 5.1. Material properties for PV Panel materials... 88

Table 5.2. Material properties for heat exchanger body 90

Table 5.3. Model validation for thermal model with cooling 94

Table 5.4. Electrical model reference parameters for the selected PV module. 95

Table 6.1. Required material properties for structural model.. 110

Table 8.1. Summary of Heat Exchanger Layout Design Simulation Results................. 173

Table 8.2. Best Ten Layout Designs according to Average Surface Temperature......... 176

Table 8.3. Best Five Layout Designs according to Heat Transfer per Unit Pumping Power 177

Table 8.4. Best Two Layout Designs according to Surface Temperature Non-Uniformity 177

LIST OF FIGURES

Fig. 1.1. P-N Junction of a PV Cell. 3

Fig. 1.2. PV Cells, Modules and Arrays. 3

Fig. 1.3. I-V Curve of a PV cell. 5

Fig. 2.1. Predicted IV points for Sandia Labs PV Model 12

Fig. 2.2. Equivalent electric circuit of a PV device. 12

Fig. 3.1. Equivalent circuit of a PV cell. 31

Fig. 3.2. Crystalline Silicon Modules Current and Voltage Errors. 53

Fig. 3.3. Thin Film Modules Current and Voltage Errors. 54

Fig. 3.4. Maximum Power prediction errors. (Module 1=AP-110, Module 2=S-36, Module 3=KC-40T, Module 4=MST-43LV, Module 5=ST-35, Module 6=PVL-124) ... 54

Fig. 3.5. Variation of Normalized Sensitivity Coefficients with (a) Absorbed Radiation and (b) PV Cell Temperature. 57

Fig. 3.6. Comparison of Maximum Power prediction accuracy (RMSE) of five parameter model and seven parameter model. (Module 1=AP-110, Module 2=S-36, Module 3=KC-40T, Module 4=MST-43LV, Module 5=ST-35, Module 6=PVL-124) 63

Fig. 3.7. Comparison of accuracy of seven parameter model for crystalline silicon technology. 64

Fig. 3.8. Comparison of accuracy of seven parameter model for thin film technology. .. 65

Fig. 3.9. Comparison of Maximum Power prediction accuracy for seven parameter model. (Module 1=AP-110, Module 2=S-36, Module 3=KC-40T, Module 4=MST-43LV, Module 5=ST-35, Module 6=PVL-124) 65

Fig. 4.1. POA Irradiance and ambient temperature for (a) January 17 - Clear day, (b) March 16 - Overcast day and (c) May 15 - Cloudy day. 75

Fig. 4.2. Modeled vs. Experimental Power - January 17 for (a) Isotropic model, (b) Hay & Davies model, (c) HDKR model and (d) Perez model. 76

Fig. 4.3. Modeled vs. Experimental Power – March 16 for (a) Isotropic model, (b) Hay & Davies model, (c) HDKR model and (d) Perez model. 77

Fig. 4.4. Modeled vs. Experimental Power – May 15 for (a) Isotropic model, (b) Hay & Davies model, (c) HDKR model and (d) Perez model. 78

Fig. 4.5. Daily Modeling error (RMSE) in power prediction for all days. 80

Fig. 4.6. Daily bias error (MBE) in power prediction for all days. 80

Fig. 5.1. Modes of energy transfer in a PV panel. 83

Fig. 5.2. Geometry of the model for PV panel without cooling 87

Fig. 5.3. Layers in PV module. 88

Fig. 5.4. Geometry of model with cooling. 89

Fig. 5.5. Meteorological and environmental data for the PV Site (Florida Solar Energy Center PV performance database) 91

Fig. 5.6. Wind speed data for Tallahassee, Florida on May 15, 2005 (Wolfram Mathematica Weather Data) 92

Fig. 5.7. Model validation for thermal model without cooling using experimental data . 92

Fig. 5.8. Model validation for thermal model without cooling using manufacturer data . 93

Fig. 5.9. Temperature distribution in PV cells for panel without cooling. 96

Fig. 5.10. Temperature distribution in PV cells for panel with cooling. 97

Fig. 5.11. Temperature distribution in water inside the heat exchanger. 97

Fig. 5.12. Flow Pattern of water inside the heat exchanger. 98

Fig. 5.13. PV panel performance variation with absorbed radiation. (T_{amb}=25°C, $V_{f,in}$=0.05 m/s, $T_{f,in}$=25°C) 100

Fig. 5.14. PV panel performance variation with ambient temperature. (S=800 W/m^2, $V_{f,in}$=0.5 m/s, $T_{f,in}$=25°C) 102

Fig. 5.15. PV panel performance variation with heat exchanger inlet velocity. (S=800 W/m^2, T_{amb}=25°C, $T_{f,in}$=25°C) 103

Fig. 5.16. PV panel performance variation with heat exchanger inlet temperature. (S=800 W/m^2, T_{amb}=25°C, $V_{f,in}$=0.5 m/s) 104

Fig. 5.17. PV panel performance variation with change in thermal contact resistance. (S=800 W/m^2, T_{amb}=25°C, $V_{f,in}$=0.5 m/s, $T_{f,in}$=25°C) 105

Fig. 6.1. X-Component of Stress in PV Cells. 112

Fig. 6.2. Z-Component of Stress in PV Cells. 113

Fig. 6.3. von Mises Stress in PV Cells. 113

Fig. 6.4. Location of paths for studying spatial stress variation 114

Fig. 6.5. Variation of PV cell temperature and von Mises stress along paths X1 and X2. 115

Fig. 6.6. Variation of PV cell temperature and von Mises stress along paths Z1 and Z2. 117

Fig. 6.7. Variation of PV cell temperature and von Mises stress along path P1 118

Fig. 6.8. Variation of von Mises stress in PV cells with operating and environmental conditions. 120

Fig. 7.1. Overall multi-physics model of PV modules. 123

Fig. 7.2. Input meteorological conditions for (a) January 17, 2000 (b) July 17, 2000 (c) October 15, 2000 and (d) December 10, 2000 126

Fig. 7.3. Paths for studying spatial distribution of temperature and stresses 127

Fig. 7.4. Time variation of (a) PV cell temperature (b) von Mises stress 128

Fig. 7.5. Along path 1: (a) temperature (b) von Mises stress (c) 1st Principal Stress (d) 2nd Principal stress 130

Fig. 7.6. Along path 2: (a) temperature (b) von Mises stress (c) 1st Principal Stress (d) 2nd Principal stress 132

Fig. 7.7. Along path 3: (a) temperature (b) von Mises stress (c) 1st Principal Stress (d) 2nd Principal stress 133

Fig. 7.8. Along path 4: (a) temperature (b) von Mises stress (c) 1st Principal Stress (d) 2nd Principal stress 134

Fig. 7.9. Across thickness: (a) temperature (b) von Mises stress (c) 1st Principal Stress (d) 2nd Principal stress (e) 3rd Principal stress 137

Fig. 7.10. Temporal and spatial variation of temperature and stress in PV panel for January 17, 2000. 139

Fig. 7.11. Temporal and spatial variation of temperature and stress in PV panel for October 15, 2000. 141

Fig. 7.12. Temporal and spatial variation of temperature and stress in PV panel for December 10, 2000. 143

Fig. 7.13. Variation of electrical power with time in PV panel with cooling for (a) January 17, (b) July 17, (c) October 15 and (d) December 10....................................... 145

Fig. 7.14. Variation of electrical efficiency with time in PV panel with cooling for (a) January 17, (b) July 17, (c) October 15 and (d) December 10...................................... 147

Fig. 8.1. Basic configuration of the heat exchanger 153

Fig 8.2. Channel Layout for Ten Parallel Channel Heat Exchanger 154

Fig. 8.3. Effect of Number of Channels.. 156

Fig. 8.4. Effect of Width of Header 157

Fig. 8.5. Effect of Tapered Channel Arrangement (Designs 1 and 2) 159

Fig. 8.6. Effect of Inlet and outlet position (Tapered Channel Arrangement Designs 3) 161

Fig. 8.7. Temperature Contour Plots for Tapered Channels Designs 4,5 and 6 163

Fig. 8.8. Velocity Vector Plots for Tapered Channels Designs 4,5 and 6 163

Fig. 8.9. Results for Center-to-Center Design 1 165

Fig. 8.10. Results for Center-to-Center Design 2 165

Fig. 8.11. Results for Center-to-Center Design 3 166

Fig. 8.12. Results for Series-Parallel Combination Layouts.. 168

Fig. 8.13 Average channel flow velocities for Ten Parallel Channels Layout with and without wider headers... 170

Fig. 8.14 Average channel flow velocities for Tapered Channel Arrangement 2 and 3. 171

Fig. 8.15 Average channel flow velocities for Centered-Inlet-and-Outlet layout 3 and Tapered Channel Arrangement 6 171

Fig. 8.16 Comparison of surface temperature non-uniformity and heat transfer per unit pumping power for the simulated design layouts 174

Fig. 8.17. Selected Heat Exchanger Channel Layout Designs 178

ABSTRACT (ENGLISH)

NAME: Muhammad Usama Siddiqui
TITLE: Multi-physics Modeling of Photovoltaic Modules and Arrays with Auxiliary Thermal Collectors
MAJOR FIELD: MECHANICAL ENGINEERING
DATE OF DEGREE: DECEMBER 2011

The objective of the current work was to develop a multi-physics performance prediction model for photovoltaic (*PV*) modules and arrays. The developed model is capable of predicting the electrical, thermal and structural performance of PV panels with and without cooling and includes a radiation and optical model for calculating absorbed solar radiation, three dimensional numerical thermal and structural models and a newly developed PV electrical model for calculating the electrical performance of the PV panels. Various studies were conducted using the developed models. These included studies to evaluate the electrical and thermal performance of the module under different environmental and operating conditions with and without cooling, a study to gain insight into the transient thermal, structural and electrical response of the system and studies to see the influence of PV cell technology on the accuracy of the developed electrical model and several other models from literature. The developed model was also used to optimize the design of auxiliary thermal collectors used for PV panel cooling applications.

ABSTRACT (ARABIC)

ملخص الرسالة

الاسم: محمد اسامه صديقي

عنوان الرسالة: نمذجة متعددة الفيزياء للوحدات و المصفوفات الكهروضوئية بمساعدة المستقطبات الحرارية.

التخصص: الهندسة الميكانيكية

تأريخ التخرج: 1433 هـ - (ديسمبر 2011 م)

الهدف من العمل الحالي هو تطوير نظام التنبؤ بالأداء المتعدد فيزيائيا للوحدات و المصفوفات الكهروضوئية. النموذج المطور قادر على التنبؤ بالأداء الكهربائي والحراري والهيكلي للألواح الكهروضوئية مع وبدون التبريد. ويتضمن النموذج المطور نظام إشعاعي وبصري لحساب مقدار امتصاص الاشعاع الشمسي . نماذج رقمية ثلاثية الأبعاد الهيكلية والحرارية والنموذج الكهروضوئي المطور وضعت في بيئة الماتلاب لحساب الاداء الكهربائي للألواح الكهروضوئية. وقد أجريت دراسات عديدة باستخدام النماذج المطورة .وشملت هذه الدراسات تقييم الأداء الكهربائي والحراري للنموذج تحت مختلف الظروف البيئية والتشغيلية مع وبدون التبريد، و دراسة الاستجابة الحرارية والهيكلية والكهربائية العابرة للنظام ودراسات اخرى لمعرفة تأثير تكنولوجيا الخلايا الكهروضوئية على دقة النموذج الكهربائي المطور ونماذج أخرى عديدة من الدراسات السابقة . تم استخدام النموذج المطور للحصول على التصميم المثالي لل مبادلات الحرارية المستخدمة في تطبيقات تبريد الالواح الكهروضوئية.

CHAPTER 1

INTRODUCTION

Today, the world is seeing an increase in its energy usage at alarming speeds and conventional fossil-based fuel resources are being consumed at an ever faster rate. Moreover, the uncertainty in the supply of conventional fuels has resulted in a need for more reliable and sustainable energy resources. The newer energy resources are expected to be sustainable, available in sufficient quantities, and have minimal environmental impact. Solar energy provides one such option and demonstrates all these desirable characteristics.

Solar energy can be utilized using two types of technologies, solar-thermal and photovoltaic. In a solar-thermal system, the solar energy is used to heat water to make steam which is then used to run a steam turbine. The power developed in the steam turbine can then be used to generate electricity. Photovoltaic technology, on the other hand, provides a direct method to convert solar energy into electricity. This, phenomenon, to directly convert electromagnetic radiation to electrical energy is known as the photovoltaic effect. Commercial production of PV cells began in the 1950s when Bell Laboratories developed the first commercially available solar cell. Until the 1970s, the only application of the PV technology was in spacecrafts. But, in the last few decades, decrease in the price of commercially available PV modules as well incentives by governments around the world have resulted in very fast growth in the use of PV systems.

1.1 INTRODUCTION TO PHOTOVOLTAICS

The fundamental building block of photovoltaic (PV) systems is the PV cell. The following sections describe the working, electrical performance and modeling issues related to Photovoltaics.

1.1.1 Working of PV cells

A photovoltaic cell is a semiconductor diode which when exposed to light generates charge carriers. If the PV cell is connected to an external circuit, current flows through the circuit. Charges are generated only if the energy of the incident solar photon is sufficient to detach the covalent electrons of the semiconductor material. Sun light consists of photons of different frequencies and hence different energies. Only the photons having energy greater than the band-gap energy of the semiconductor material generate charge carriers in the cell. For photons with energy greater than the band-gap of the material, only the amount of energy equal to the band-gap is utilized to generate charge carriers. The remaining part of the energy raises the cell temperature.

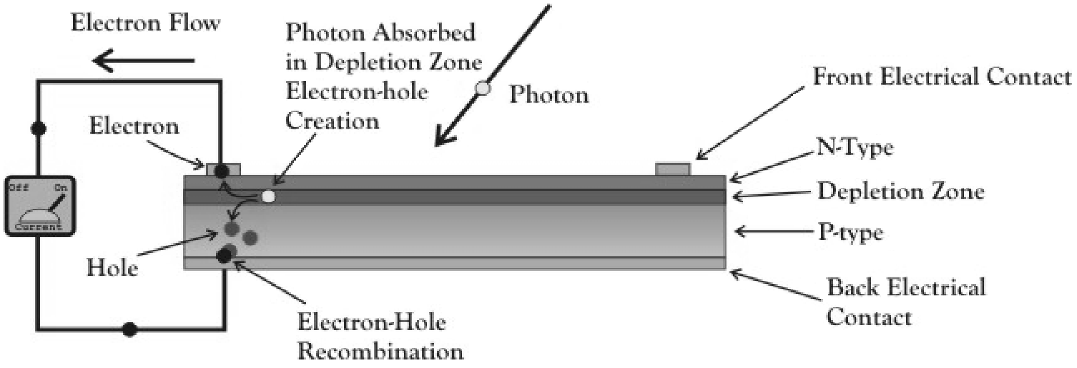

Fig. 1.1. P-N Junction of a PV Cell.

1.1.2 PV Cells, Modules and Arrays

The fundamental building block of PV systems i.e. PV cell generates an electrical power of about 0.5W in case of crystalline silicon cell which is very low. Therefore series and parallel combinations of cells are made to get the desired electrical power and voltage. Commercially, PV manufacturers mostly provide PV modules which consist of 36 or more PV cells connected in series. To develop the desired power, PV system designers make PV arrays which are series and parallel combinations of PV modules.

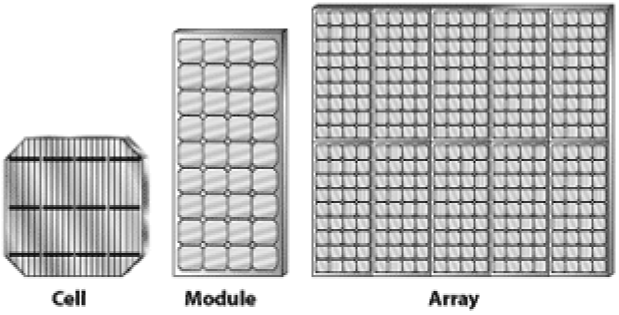

Fig. 1.2. PV Cells, Modules and Arrays.

1.1.3 PV Cell Technologies

The two basic types of commercially available solar cells are crystalline silicon solar cells and thin film solar cells.

Crystalline silicon cells further divided into sub-types depending on the crystallinity and crystal size in the cell. These sub-types are mono-crystalline silicon and poly-crystalline silicon. Mono-crystalline silicon (c-Si) cells, as the name suggests consist of only a single crystal per cell is the most efficient and most expensive of all crystalline silicon cells. Poly-crystalline silicon (mc-Si) cells utilize a slightly simpler and, thus, less expensive manufacturing process. These cells consist of multiple crystals in each cell and have efficiency lower than that of mono-crystalline silicon cell.

The main thin film solar cells technologies include amorphous silicon (a-Si), Cadmium Telluride (CdTe), Copper Indium Selinide (CIS) and Copper Indium Gallium Selinide (CIGS). These technologies have the advantage of reducing the requirement of light absorbing materials and thus are relatively less expensive than crystalline silicon technologies. Presently, the thin film market is dominated by CdTe, CIS and CIGS technologies.

1.1.4 Electrical Performance of PV Systems

The electrical performance of a PV cell, module or array is determined by the solar radiation absorbed in the cell, the cell temperature and external load attached to the cell. The current voltage relationship of a PV cell is shown in Fig. 1.3. As can be seen from the I-V curve, PV cells behave as constant current sources at low voltages and as constant voltage sources at high voltages. The maximum power output (P_{mp}) at a given radiation and cell temperature occurs at a point on the bend in the I-V curve. This point is called the maximum power point (*MPP*). The current at zero voltage is termed short-circuit current (I_{sc}) and the voltage at zero current is termed open circuit voltage (V_{oc}).

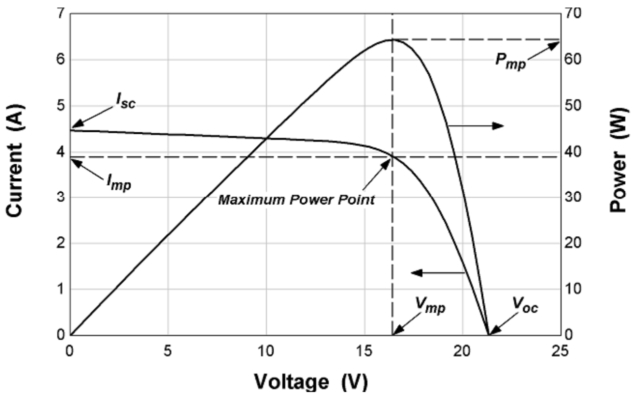

Fig. 1.3. I-V Curve of a PV cell.

When the PV cell is connected to an external load, the electrical characteristics of the load determine the actual point on the I-V curve at which the PV cell operates. PV cells are often connected to the load through a maximum power point tracker (*MPPT*) which regulates the cell voltage in order to operate the cell at maximum power point.

1.1.5 Modeling of Photovoltaic Modules and Arrays

In all applications of PV systems, accurate simulation tools are required to predict how the system would work under the operating conditions. Such tools enable designers to accurately size and design the PV systems and give investors a confidence in their investments. The main performance characteristic of the PV system is the electrical power output. To predict the electrical performance of PV systems, several electrical models of varying complexities have been developed [1–3]. But the electrical model alone is not sufficient to provide the electrical power output of the system. Two other models, a thermal model, either with cooling or without cooling, to calculate the PV cell temperature from environmental and operating conditions [4–7] and a radiation model, to calculate the solar radiation absorbed in the PV cells [8–11], are required. The outputs of the radiation and thermal models are input into the electrical model to calculate the power output. If the structural performance of the PV panel is also included, four different physics need to be solved in order to predict the thermal, electrical and structural performance of the PV system. The models are sequentially coupled together to get the overall performance of the PV system.

1.2 MOTIVATION BEHIND PRESENT WORK

Modeling of PV modules and PV systems in general is an area of very active research these days due to the increasing rate of PV systems deployment for power production around the world. In this regard, several avenues were identified where contributions to the field of PV modeling was possible.

In the electrical modeling of PV devices, it was found that several different methodologies are being used for parameter estimation for the equivalent electric circuit model. Among these techniques are some which simplify the model to make the estimation process easier but increase the modeling error while other methodologies which attempt to increase accuracy require large amount of experimental data. Such works show a possibility of development of better parameter estimation methodologies which can improve accuracy of the electrical model while requiring only manufacturer supplied data. Another motivating factor for improving the electrical model was the result of work done by Boyd et al. [12] in which they attempted to improve the electrical model by modifying the translation equations for two of the five model parameters but failed to achieve any significant improvement in prediction accuracy.

In the literature regarding thermal modeling of PV panels, it was seen that detailed three dimensional numerical thermal models of PV panels are usually studied separately and are usually not combined with electrical models. For electrical performance prediction, usually simple analytical expressions for PV cell temperatures are used. In this study, detailed three dimensional thermal models will be used in the overall performance model.

Finally, the structural modeling of PV panels is largely an unexplored area of research. Simple finite element based models can give insight into the structural response of the PV panels to thermal cycling. Such models can then be combined with reliability models to predict failures in different parts of the PV panels.

1.3 OBJECTIVES OF CURRENT WORK

The objectives of the thesis study are listed below.

- To develop a Multi-Physics Model for PV systems capable of predicting the electrical, thermal and structural performance of the system.
- To validate the model using available experimental data and previously published work.
- To use the model to:
    - Study the effect of PV cell technology on PV performance
    - Study the effect of panel cooling on the performance of PV panels under different environmental and operating conditions
    - Study the effect of thermal cycling on PV system’s performance
    - Optimize the design of PV heat exchanger for better PV system performance

CHAPTER 2

LITERATURE REVIEW

Models of PV systems can be sub-divided into several sub-models each covering a different physics of the PV system. These include the electrical, thermal, radiation and the structural models. The following sections discuss the state of the art for each of these models.

2.1 RADIATION MODELING

The accuracy of the absorbed solar radiation which is input in the electrical model is very important for accurate electrical performance prediction of the PV system. A variety of radiation models [8,10,11,13] of varying complexities have been developed over the years to calculate the solar radiation falling on the surface of the PV panels and are combined with optical models [14] to calculate the absorbed solar radiation. The difference between the various radiation models is in the way the diffuse solar radiation is treated. The simplest radiation model, the isotropic sky model [8] treats only the isotropic component of diffuse radiation. The Hay & Davies model [13] treats two components, isotropic and circumsolar, of diffuse radiation while Perez model [11] and the Hay-

Davies-Klutcher-Reindl (*HDKR*) model [10] also treat the final component, horizon brightening diffuse radiation. Cameron et al. [15] compared the accuracy of several radiation models. They computed the total radiation falling on the PV panels using measured beam and total radiation as well as beam and diffuse radiation on horizontal surfaces using the isotropic sky model, Hay & Davies model, *HDKR* model and the Perez model. They found that predicted plane-of-array (*POA*) radiation for all the models was higher when the total and diffuse radiations were used as inputs. They also concluded that the predictions of all models except the isotropic sky model were more conservative for summer months than winter months. In another study, Mondol et al. [16] compared the accuracy of the four radiation models when only the total horizontal radiation was used as the input. They also used several total-diffuse radiation correlations to calculate the horizontal diffuse radiation and also proposed a new correlation. They concluded that the accuracies of all the models were higher in summer than in winter. In winter, the isotropic sky model was the most accurate while the Perez model had the highest overall accuracy.

2.2 ELECTRICAL MODELING

Modeling of the electrical performance of PV systems is vital for system designers in making efficient PV systems. Over the years, various electrical models to predict instantaneous as well as long term performance of PV systems have been developed. These include models that are based on the analytical knowledge of how a PV cell behaves, empirical models use simple correlations and models which combine the two approaches. King et al. [2] developed an empirical model for simulation of PV systems called the Sandia Labs PV Model. The model includes its own thermal and radiation models. It takes the incident solar irradiance, ambient temperature and wind speed as inputs and calculates the currents and voltages at five key points on the I-V curve. These five points are shown in Fig. 2.1. To predict the performance of any PV module, thirty empirically determined coefficients are required for the model. Sandia Labs maintains a list of constants for a large number of commercially available modules. Hishikawa et al. [17] developed a methodology for translating the I-V curves from one irradiance level to another. Marion et al. [3] extended their work by presenting the bilinear interpolation model. Their method used four experimentally determined I-V curves at two different irradiances and two different temperatures. To get the I-V curve at operating conditions, the four experimentally determined I-V curves were first interpolated with respect to open-circuit voltage to account for PV module temperature, and second with respect to short-circuit current to account for irradiance. A validation of the modeled I-V curves for 26 different PV modules showed that the modeled curves compared closely with measured curves.

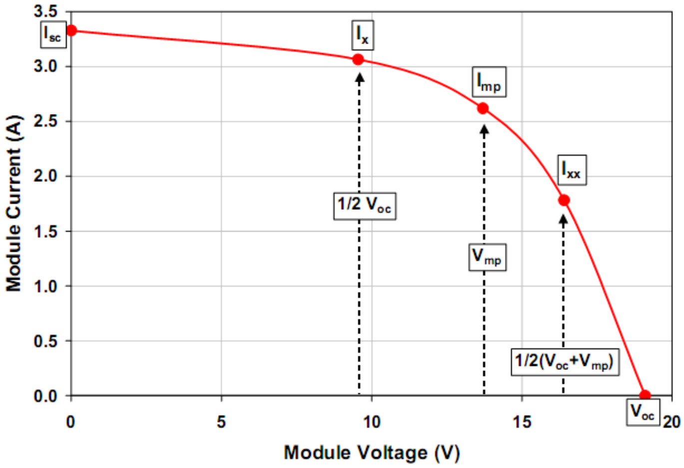

Fig. 2.1. Predicted IV points for Sandia Labs PV Model [2].

Another approach to model the electrical behavior of PV systems is to represent them with an equivalent electric circuit. The circuit consists of a light-controlled current source, a p-n junction diode and two electrical resistances. It is shown in Fig. 2.2.

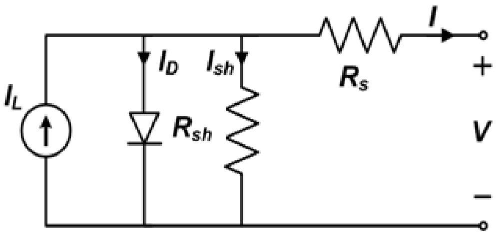

Fig. 2.2. Equivalent electric circuit of a PV device.

Townsend [18] developed a equivalent electric circuit model for predicting the performance of direct coupled PV systems. His model, widely known as the 4 Parameters Model, requires only data available in manufacturer datasheets to determine parameters for an equivalent electric circuit that can predict the electrical performance of PV systems. In the 4 Parameters model, it is assumed that the shunt resistance R_{sh} connected in parallel to the current source is infinite and therefore neglected. Chenni et at. [19] presented a method to implement the 4 Parameters model in the MATLAB programming environment. The modeling process and configuration of the computer simulation were presented. The required inputs for the model were the absorbed solar irradiance and PV cell temperature. Although the 4 Parameter model is very easy to implement and provides satisfactory result for crystalline technologies, the model fails to predict the performance of many thin film technologies such as amorphous silicon. De Soto et al. [1] presented an improved electric circuit model for PV simulation called the 5 Parameters model. The additional parameter considered in their model was the shunt resistance which was considered to have a finite value. They also presented a comparison of model prediction results, experimental data from a building integrated photovoltaic facility at the National Institute of Standards and Technology (NIST) and the prediction results of the Sandia Labs PV model for four different cell technologies (single crystalline silicon, poly crystalline silicon, silicon thin film, and triple-junction amorphous silicon). The predictions from the five-parameter model were shown to agree well with both the Sandia model results as well as the experimental data for all four cell technologies over a range of operating conditions. Villalva et al. [20] developed a new methodology for solving the 5 Parameters model of a PV system. In their methodology, the parameters for the model are determined by adjusting the curve at three points: open circuit, maximum power, and short circuit. Given these three points, which are provided in all commercial module datasheets, the method finds the best combination of model parameters that give the least error at the three points. Valerio et al. [21] developed a new variation of the 5 parameters model capable of more accurately accounting for changes in operative temperature and solar irradiance. To find the model parameters for a given PV module, a system of I-V equations was solved based on data issued by manufacturers for module performance at standard rating conditions (STC) with a trial and error process. To minimize the modeling error in the 5 Parameters model for amorphous silicon PV cell type modules, Merten et al. [22] developed an improved equivalent circuit for hydrogenated amorphous silicon (a-Si:H) solar cells and modules. The circuit was based on the combination of a diode with an exponential current–voltage characteristic, a photocurrent source and a new term representing additional recombination losses in the i-layer of the device. The presented model was shown to match the current–voltage curves of a typical laboratory amorphous silicon cell for a wide range of illumination levels varying over six orders of magnitude. Campbell [23] proposed a simple piecewise linear PV device model for dynamic and transient analysis of the PV system. The model utilized piecewise linear diodes to approximate the slope of the I-V curves of PV systems. Because of its piecewise linear nature, the model was much easier to implement than many other nonlinear PV models. Boyd et al. [12] studied the predictive capabilities of the 5 Parameters model for crystalline silicon as well as thin film cell types and attempted to improve the model. They found out that the inclusion of a Plane-of-Array irradiance correction factor reduces the errors caused by the radiation model significantly. To improve the electrical model itself, they tried two different approaches. In the first approach, the included two additional parameters to improve the translation equations for I_o and R_s and in the second approach, a current sink was added in parallel with the electric circuit. From their study, they concluded that the two approaches provided neither significant nor consistent improvement in the prediction accuracy of the electrical model.

One of the most difficult tasks in the implementation of the equivalent electric circuit models of PV systems is the determination of the model parameters. Because of the highly nonlinear nature of the current voltage relationship, direct simultaneous solution of the I-V equations written at various points on the I-V curve is very difficult. To overcome this difficulty, several approaches have been adapted. De Soto [1] and Boyd [12] used a specialized nonlinear simultaneous equation solver to solve five equations to determine the model parameters. Villalva et al. [20] and Townsend [18] assumed one of the parameters explicitly and solved for the remaining parameters using iterative processes. Carrero et al. [24] used an iterative procedure to find the values of all five parameter. Their method only requires the I-V data of three points i.e. the short circuit, open circuit and maximum power points. Their method uses simplified forms of the I-V equation written at the three points and provides fast convergence. They validated their model against catalogue data from the manufacturer as well as experimental data and found the errors at the current and voltage at the maximum power point to be less than 0.1% for crystalline silicon cell type. Another approach used for finding the model parameters is to use optimization techniques to minimize the error in the model I-V prediction. Ikegami et al. [25] used the Levenberg-Marquardt multivariable optimization method to minimize the error in model current prediction using experimentally measured I-V points. Zagrouba et al. [26] used an approach similar to Ikegami et al. but used genetic algorithms for the optimization.

The electrical models discussed so far assume perfect homogeneity in solar cells as well as in operating conditions. The models can, however, be extended to include the effects of such inhomogeneities. Chouder et al. [27] analyzed the effect of cell mismatch losses on the electrical power prediction of a PV system. They implemented the 5 Parameters model using array parameters and using module parameters and found up to 10% difference between the two. Kaushika and Rai [28] studied the effect of mismatch losses in ageing PV cells. They discussed various possible reasons for cell mismatch such as manufacturer tolerances, structural defects and module shading and developed a methodology to calculate the fractional power loss in PV arrays due to cell mismatch. Karatepe et al. [29] developed an ANN based methodology to predict the electrical performance of partially shaded PV arrays. They concluded that due to partial shading, the I-V characteristics of the PV system are modified, the P-V curve gets multiple peaks and the maximum power point is shifted. Patel and Agarwal [30] developed a MATLAB based tool for predicting the I-V and P-V characteristics of PV arrays and inhomogeneous shading conditions. They used the tool to study the electrical performance of partially shaded PV systems under various shading patterns. Their results showed that in case of shading multiple peaks occur in the P-V characteristics from which they concluded that existing maximum power point trackers (MPPTs) cannot accurately track the maximum power point (MPP) of shaded PV arrays. Grabitz et al. [31] proposed a model to simulate spatially inconsistent solar cells i.e., combinations of cells whose electrical performance vary from each other. The proposed model is based on an equivalent circuit having 2 diodes. From the analysis they conducted, they concluded that the overall performance deteriorates with increasing inhomogeneity.

2.3 THERMAL MODELING

The performance of PV systems is directly affected by the operating temperature of the PV cells. As the cell temperatures increase, the electrical conversion efficiency of the PV cells decrease. Skoplaki and Palyvos [32] provided a very good discussion on the dependence of the electrical performance of PV systems on operating temperature. They also presented various correlations that relate the conversion efficiency and the output power of the PV systems with the operating temperatures. In most performance prediction cases of PV systems, the temperature variation of PV cells under operating conditions is unknown and has to be estimated from environmental and operating conditions such as absorbed solar radiation, wind speeds, ambient temperature, PV electrical characteristics and if cooling is present, the type of type and operating conditions of the cooling system.

To determine the PV cell temperature for PV panels without cooling, several different approaches have been used. Jones and Underwood [4] developed an analytical transient model to determine the temperature of PV modules. They assumed uniform temperature in the PV module and considered convection and radiation energy transfer to the environment and electrical energy transfer to the load in their model. King et al. [2]

proposed an empirical model to predict the module back surface and the PV cell temperatures as a function of ambient temperature, wind speed and incident solar irradiance. Their model required two empirical coefficients which depended on the front and back cover materials of the PV module. Notton et al. [33] developed a 1-Dimensional transient model that considered three material layers, front cover, PV cell and back sheet and solved the transient thermal balance for the three layers using finite differences. They also studied the accuracy of various combinations of forced and natural convection correlations for modeling the convective heat transfer to the environment and found that the use of only the forced convection correlation provided the best results. Tina and Scrofani [34] developed an analytical model to calculate the temperature of PV cells. In their model, they assumed the PV panel to consist of three layers, namely a front cover, PV cells and back sheet. Uniform temperature distribution was assumed in each layer and the heat capacitance effects were ignored. These assumptions results in three steady state energy equation for the three layers which when solved gave the temperatures of the three layers. Bigot et al. [35] developed a detailed thermal model of PV panels that was integrated in the building simulation code ISOLAB. In their model, radiation exchange to the environment and between various layers in the PV panel, conduction between the panel layers and convection to the environment are all treated in detail. Acciani et al. [5] used the finite element method to study the steady state thermal performance of poly crystalline and amorphous silicon PV cells. In their study, they considered the various material layers present in the PV cell and thermal behavior under only radiative load, only Joule’s heating effect and the combination of the two have been studied. Skoplaki and Palyvos [36] presented a survey of various implicit and explicit correlations found in literature for determining the PV cell operating temperature.

At present, the maximum reported conversion efficiency for commercial PV modules is 22.4% [37]. The remaining solar energy absorbed into the panel is converted to heat and increases the panel temperature. Moreover, an increase in the module temperature causes the module efficiency to decrease [32]. Therefore, decreasing the cell temperature can lead to better conversion efficiency for the PV cells and thus to more electricity generation. A number of studies have been done to combine the photovoltaic panel and the flat plate collector into a single collector called the photovoltaic/thermal (PV/T) collector. The additional flat plate collector has a two-fold purpose. Firstly, it cools the PV panel which improves its efficiency and secondly, it collects thermal energy which otherwise would have been wasted. For PV panels working under solar concentration, the requirement of cooling becomes even greater. Under concentration, PV panels experience not only high efficiency drops due to very high temperatures but may also develop structural defects.

Several studies have been conducted to see the effect of cooling on the performance of PV systems. These include studies in which off-the-shelf PV panels are cooled by heat exchangers (air or water-type) [38–40] and studies of custom-made PV/T collectors specially designed for thermal energy collection along with electricity generation [41–43]. PV/T collector performance modeling is also an important area of research. Most experimental studies done on PV/T collectors are accompanied by analytical modeling.

Apart from these, many researchers have focused specifically on developing PV/T analytical models of varying complexities that are capable of predicting the system’s electrical and thermal performance for specified environments. Teo et al. [38] designed and developed an air cooled PV/T system using a commercially available PV panel and a custom made air collector attached to it. They analyzed the performance of the system using an analytical models as well as experiments and found that the electrical efficiency of the PV panel improved by as much as 5% when the panel was cooled. Shahsavar and Ameri [39] designed a directly coupled air cooled PV/T collector and developed an analytical model for predicting its performance. They conducted studies to understand the effect of changing mass flow rate on the system’s electrical, thermal and overall efficiency. They found that the thermal efficiency increased with increasing mass flow rate. The electrical efficiency, on the other hand, first increased but then decreased because of additional electrical power consumption by the fans. They also studied the effect of glass covers on system performance and found that the thermal efficiency increased while the electrical efficiency decreased when a glass cover was placed over the system. Tiwari et al. [40] investigated the performance of a commercially available PV module integrated with an air duct for cooling. They developed an analytical model to determine the system performance by writing the energy balance equations for each component. They calculated the system performance and validated it experimentally for three cases, first without forced air flow in the duct, second with forced convection using a single fan and third with forced convection in the duct using two fans which gives more air flow rate through the duct. They found good agreement between the model and experimental results. Huang et al. [41] presented the design of a water-type PV/T collector called the Integrated PhotoVoltaic Thermal System (IPVTS). Through experiments, they studied the performance of the IPVTS collector and found the system to have primary-energy conversion efficiency better than solar thermal collector and PV panel separately. Tonui and Tripanagnostopoulos [42,43] designed air cooled PV/T collectors and studied the effects of two low cost performance improvements. In the first improvement, a thin metal sheet was placed horizontally in the middle of the channel and in the second, fins were added to the lower surface of the channel. They developed analytical model to calculate the thermal efficiency of the system and experimentally validated the model. Using this model, they conducted various parametric studies to study the effect of channel depth, duct length and mass flow rate on the thermal and electrical efficiencies of the system and the pressure drop in the duct. There results show that reducing the channel depth and increasing the mass flow rate increases the thermal and electrical efficiency of the system but increasing the fan’s power requirement. Increasing the duct length increases the thermal efficiency but reduces the electrical efficiency of the system. Tiwari and Sodha [44] developed an analytical model for the IPVTS collector and validated its performance against the experimental data of Huang et al. [41]. To model the electrical performance of the system, they used a simple model to scale the efficiency of the PV panel with temperature change. For the thermal model, they used an energy approach to develop equations for PV cell, PV back surface, storage tank fluid and fluid outlet temperatures and useful energy collector through the fluid. The final form of their model is similar to the Hottel-Whiller equations for flat plate solar thermal collectors. An improvement to this model was suggested by Sarhaddi et at. [45]. They suggested that the accuracy of the model could be improved by using the equivalent electric circuit model to determine the electrical performance of the system and by using more detailed expressions for determining the thermal resistances within the system. They applied their model to the air-type PV/T collector developed by Joshi et al. [46] and found better agreement with the experimental measurements than the model presented by Joshi et al. [46]. Dubey and Tiwari [47] developed an analytical model for PV/T collectors partially covered by PV cells. Using their model, they compared the performance of three design cases, first in which PV cells completely cover the thermal collector, second in which PV cells cover 50% of the collector and last in which the cells cover 30.56% of the collector. The result of their study showed that the improvement in instantaneous efficiency of the system from the first case to the last one was 31%. Dubey and Tiwari [48] developed a mathematical model for calculating the performance in PV/T collectors in series and parallel combinations. Using their model, they studies the instantaneous performance as well as monthly yield of four different combinations of PV/T collectors, a series combination of PV/T collectors partially covered by PV cells, a series of combination of PV/T collectors completely covered with PV cells and glass, a series of combination of PV/T collectors completely covered with only PV cells and a system of an array of PV/T collectors completely covered with PV cells in series and parallel combination. The results of their study suggested that the first type of system perform best when the primary concern is thermal energy collection while the fourth types performed best when the primary concern is electricity generation. Kalogirou [49] used the system analysis software TRNSYS to develop a model for PV/T collectors. Using the typical meteorological year (TMY) data for Nicosia, Cyprus, he simulated the performance of the system for the whole year. Optimization of the mass flow rate of water was also done to maximize the system efficiency. Zondag et al. [50] conducted an extensive study to see the effect of the complexity of the model on prediction accuracy. They developed four numerical models, a 3D transient and three steady state (1D, 2D and 3D) models. They compared the results of the models with experimental measurements. Their findings suggested that the effect of including dynamical effects on day's energy output prediction was less than 1% but error in steady state model increased for smaller periods of time. A comparison of the various models showed that the simple 1D model performs satisfactorily for long term energy output prediction while reducing the computation time by as much as 70 times compared to the 3D model. But Zondag et al. argued that the more complex 2D and 3D models are much more equipped to handle complex flow patterns and for PV/T design optimization tasks. For further study on PV/T systems, the reader is referred to the works of Charalambous et al. [51], Zondag [52] and Ibrahim et al. [53] who have done extensive reviews of PV/T technology in general and its types, working theory and modeling approaches for various types of PV/T collectors.

For PV panels working under solar concentration, the requirement of cooling becomes even greater. Under concentration, PV panels experience not only high efficiency drops due to very high temperatures but may also develop structural defects. Othman et al. [54] developed a double pass air-type PV/T collector with compound parabolic collectors (CPC) for solar concentration and fins for better heat transfer. They developed a steady state model for the system and validated the model under laboratory conditions. Coventry [55] developed the combined heat and power solar (CHAPS) collector. The CHAPS system consisted of a linear parabolic trough concentrator that concentrated 37 suns on to mono-crystalline PV cells. The cells were cooled by water that flowed in tubes behind the cells. Royne et al. [56] did a review of the possible cooling mechanisms for PV systems under various types of solar concentration.

2.4 STRUCTURAL MODELING

As far as structural performance of PV panels is concerned, the main approach used is using finite element methods [57–60]. In an effort to optimize the design of PV cell interconnects to reduce thermal stresses, Eitner et al. [57] developed a structural model for a string to PV cells laminate using finite element method. Their model consisted of two sub-models: a three dimensional model for the PV cells string and a two dimensional model for the cell interconnects. The model was exposed to uniform temperature loads from 150°C to -40°C and the thermal stresses were calculated in a static time-independent analysis. Gonzalez et al. [58] used an FEA based model to study the effect of encapsulent and adhesive materials and PV cell size on the thermal stresses developing in the cells and their interconnects. Using the developed model, they conducted a parametric study to see the effect of encapsulent material, encasulent thickness, adhesive thickness and cell thickness on the thermal stresses developing in the cell. They concluded that the stresses were minimum for a soft encapsulent material, thin encapsulent layer and thick solar cells. They also studied the effect of thermal loading on the cell interconnects by changing the laminate temperature from -40°C to 150°C. Meuwissen et al. [59] developed a finite element model for a single PV cell laminate to study the structural response of adhesive cell interconnects. Using the developed FE model, they studied the effect of adhesive interconnect on the stresses developing in the cell interconnects by reducing the laminate temperature uniformly from 150°C to 20°C. They also studied the effect of the presence of EVA on the stresses developing in the interconnects by heating up the laminate uniformly from 80°C to 150°C. Dietrich et al. [60] presented a finite element based modeling methodology which consisted of an overall model of the entire panel and several sub-models for studying the effects of thermal and mechanical loads on the PV module. They studied the stresses developing in the module during the lamination process and during thermal cycling between -40°C and 150°C.

One of the most important factors which affect the prediction accuracy of finite element models is the accuracy of the material models. PV modules consist of several materials and capturing the accurate behavior of all of these materials is important. Eitner et al. [61] discussed material modeling issues for the various materials present in PV modules. They laid special emphasis on the modeling of the encapsulent material, EVA. For EVA, they considered temperature-independent linear elasticity, temperature-dependent linear elasticity as well as viscoelasticicty material models. By comparing the model results with experimental measurements, they concluded that for the temperature range of -40°C to 150°C, the viscoelasticity model best represented the behavior of EVA. In a previous work, Eitner et al. [57] used linear elastic material models for all the materials present in a PV module. Gonzalez et al. [58], on the other hand, used isotropic, linear elastic and temperature-independent material models for front glass, silicon cells, encapsulent and a elastic, perfectly-plastic for copper interconnects. Meuwissen et al. [59] in their study of the effect of adhesive interconnects on the stresses in PV modules developed a viscielasticity model for the adhesive material. They used linear elastic models for the remaining materials. Dietrich et al. [60] used a viscoelasticity model for encapsulent and linear elastic models for the remaining materials for the temperature range of -40°C to 150°C.

Another important factor which affects the results of thermal stress analyses is the selection of strain-free temperature. Eitner et al. [57,61] assumed a strain-free temperature of 150°C to study the thermal stresses developing in thermal cycles. Gonzalez et al. [58] assumed a strain-free temperature of 100°C for their study. Dietrich et al. [60] used a strain-free temperature of 150°C for the simulation of the lamination process and 20°C for thermal cycling. This suggests that no standard strain-free temperature is available and various values of strain-free temperature have been used in previous work.

In all previous work discussed so far, the focus was to study the stresses developing in the module during the lamination process and/or the IEC 61215 standard thermal cycle. Additionally, the structural models were not combined with a thermal model to first determine the temperature distribution inside the module which would have extended the model capabilities to simulate the effect of real-life environmental conditions on the module performance. Instead, uniform temperature load was applied to the entire model.

CHAPTER 3

ELECTRICAL MODELING

3.1 ELECTRICAL MODELING OF PV MODULES

In order for engineers to design efficient PV systems, methods to predict the electrical performance of the PV system under different environmental and operating conditions are required. To make this possible, various electrical models have been developed for predicting the electrical behavior of PV cells and PV systems in general. These range from very simple systems such as Maximum Power Scaling with changing operating conditions that require only one parameter to predict the PV performance to the very complex models such as Sandia Lab's PV Model which requires 30 experimentally determined parameters. The inputs for all of these models are the absorbed radiation and the PV cell operating temperature. The four most common methodologies used in PV electrical models are given below.

- Temperature and Radiation scaling of reference measurements
- Interpolation of I-V curves
- Empirical derivation of correlations
- Electrical circuit modeling

3.1.1 Temperature and Radiation Scaling of Reference Measurements

The most basic electrical performance modeling method for PV modules and arrays is to scale the power output of the PV system to account for the changes in cell temperature and absorbed radiation. *PVFORM* is a very popular PV electrical performance model which employs this method. The required data about the module include maximum power P_{mp} at standard test condition (*STC*) and the temperature coefficient of maximum power. The required inputs are the cell operating temperature and the absorbed radiation. *PVFORM* model is given by equations (3.1) and (3.2) [62]. The advantage of the *PVFORM* model is that it requires very small amount of data about the module and is relatively easy to implement. Its disadvantage is that it only provides PV electrical performance data at one point, i.e. the maximum power point.

$$P_{mp} = \frac{S}{S_{ref}} P_{mp,ref}(1+\gamma(T-T_{ref})) \qquad S > 125W/m^2 \tag{3.1}$$

$$P_{mp} = \frac{0.008S^2}{S_{ref}} P_{mp,ref}(1+\gamma(T-T_{ref})) \qquad S < 125W/m^2 \tag{3.2}$$

where P_{mp} is the maximum power output, S is the absorbed radiation, γ is the maximum power temperature coefficient and T is the cell temperature. The subscript *ref* represents the reference condition for which the measured PV data is reported in datasheet.

3.1.2 Interpolation of I-V curves

Interpolation methods use experimentally determined I-V curves to determine the electrical performance of the PV system at other operating conditions. Hishikawa et al. [17] presented an interpolation model that utilized two experimentally determined I-V curves at different irradiances to calculate the I-V curve at some other irradiance. Marion et al. [3] extended this work to include the effect of change in temperature. Their Bilinear Interpolation model uses four I-V curves at two different temperatures and two different irradiances to determine the electrical performance of a PV system. The Bilinear Interpolation method gives highly accurate results with RMS errors remaining below 2% for most cases but requires four experimentally determined I-V curves.

3.1.3 Empirical Derivation of Correlations

The most popular empirical model for determining the electrical performance of a PV system is the Sandia Lab’s PV model. The Sandia Labs PV model was developed by King [2] and determines the I-V characteristics of a PV system at five key points on the I-V curve. These points are short circuit, maximum power, open circuit, midway between short circuit and maximum power, and midway between maximum power and open circuit. The Sandia Lab’s model requires thirty experimentally determined parameters to calculate the I-V characteristics of the PV system. The Sandia lab’s model also includes an empirical radiation model as well as an empirical thermal model. Sandia Labs maintains a database of parameters for commercially available modules.

The Sandia Labs model provides accurate results and requires very low computational effort to determine the electrical performance of a PV system. The required inputs are the beam and diffuse radiation, ambient temperature and wind speed. The disadvantage of this model is that it requires experimental parameters and these parameters might not be available in the Sandia Lab's database.

3.1.4 Electric Circuit Modeling

Any PV element, whether it is a PV cell, module or an entire array, can be represented by an equivalent electric circuit [63]. The equivalent circuit, shown in Fig. 3.1, comprises of a light dependent current source, a p-n junction diode and two resistances. It should be noted that the equivalent circuit of Fig. 3.1 is based on the physics of crystalline silicon cell.

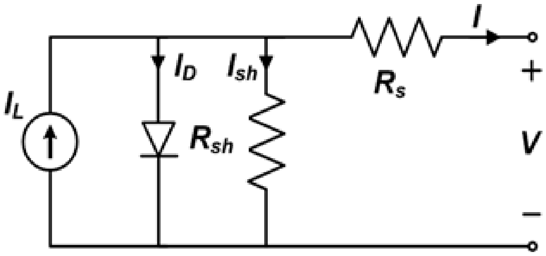

Fig. 3.1. Equivalent circuit of a PV cell.

3.2 FIVE PARAMETERS MODEL

The current-voltage relationship of the PV device represented by the equivalent circuit of Fig. 3.1 is described by equation (3.3) and is governed by five model parameters (I_L, I_o, a, R_s and R_{sh}). The electrical model that describes the electrical performance of a PV device using equation (3.3) is called the five parameter model.

$$I = I_L - I_o \cdot \left(exp\left(\frac{V + I \cdot R_s}{a} \right) - 1 \right) - \frac{V + I \cdot R_s}{R_{sh}} \tag{3.3}$$

where I and V are the output current and voltage, I_L is the light-dependent current, I_o is the leakage current, R_s is the series resistance, R_{sh} is the shunt resistance and a is the modified diode ideality factor.

Before the equation can be used, the unknown model parameters need to be determined. De Soto et al. [1] described a methodology to find these parameters using only the data available in PV module datasheets. Module datasheets provide I-V data at three key points on the I-V curve at standard test conditions (*STC*). These points are short circuit, open circuit and maximum power points. Five equations are used to solve for these parameters. The first three equations are determined by writing equation (3.3) at short circuit condition, open circuit condition, and the maximum power point.

$$I_{sc,ref} = I_{L,ref} - I_{o,ref} \cdot \left(exp\left(I_{sc,ref} \cdot R_{s,ref} / a_{ref} \right) - 1 \right) - I_{sc,ref} \cdot R_{s,ref} / R_{sh,ref} \tag{3.4}$$

$$I_{L,ref} = I_{o,ref} \cdot \left(exp\left(V_{oc,ref} / a_{ref} \right) - 1 \right) + V_{oc,ref} / R_{sh,ref} \tag{3.5}$$

$$\begin{aligned} I_{mp,ref} = I_{L,ref} - I_{o,ref} \cdot \left(exp\left(\frac{V_{mp,ref} + I_{mp,ref} \cdot R_{s,ref}}{a_{ref}} \right) - 1 \right) \\ - \frac{V_{mp,ref} + I_{mp,ref} \cdot R_{s,ref}}{R_{sh,ref}} \end{aligned} \tag{3.6}$$

In addition, at the maximum power point, the derivative of electrical power output with respect to voltage is zero. This is used to derive the forth equation,

$$\frac{I_{mp,ref}}{V_{mp,ref}} = \frac{I_{o,ref} / a_{ref} \cdot exp\left(\dfrac{V_{mp,ref} + I_{mp,ref} \cdot R_{s,ref}}{a_{ref}}\right) + 1 / R_{sh,ref}}{1 + I_{o,ref} \cdot R_{s,ref} / a_{ref} \cdot exp\left(\dfrac{V_{mp,ref} + I_{mp,ref} \cdot R_{s,ref}}{a_{ref}}\right) + R_{s,ref} / R_{sh,ref}} \tag{3.7}$$

Module datasheets also provide the temperature coefficients of short circuit current and open circuit voltage. The open circuit voltage temperature coefficient is used to develop the fifth equation required to solve for the five parameters.

$$\mu_{Voc} = \frac{V_{oc,10} - V_{oc,ref}}{T_{10} - T_{c,ref}} \tag{3.8}$$

The subscript $_{10}$ denotes a temperature 10 degree higher than the *STC* reference temperature. $V_{oc,10}$ is determined by the equation (3.9). The other parameters required for solving (3.8) are given by equations (3.10)-(3.12).

$$0 = I_{L,10} - I_{o,10} \cdot \left(exp\left(V_{oc,10} / a_{10}\right) - 1\right) - V_{oc,10} / R_{sh,ref} \tag{3.9}$$

$$a_{10} = a_{ref} \cdot T_{10} / T_{ref} \tag{3.10}$$

$$I_{L,10} = I_{L,ref} + \mu_{isc} \cdot 10 \tag{3.11}$$

$$I_{o,10} = I_{o,ref} \cdot \left(T_{10} / T_{ref}\right)^3 \cdot exp\left(E_g \cdot q / k \cdot \left(1 / T_{ref} - 1 / T_{10}\right)\right) \tag{3.12}$$

Equations (3.4)-(3.12) form a set of nonlinear equations which need to be solved for to determine the five unknown parameters at the reference condition. Exact solution of these equations is very difficult to obtain due to highly nonlinear nature of the equations. A variety of techniques have been used to solve these equations. De Soto et al. [1] and Boyd [12] used a specialized non-linear equation solver to get a solution. Villalva et al. [20] explicitly defined one parameter, a_{ref}, and then solved for the remaining parameters. Townsend [18] simplified the model by assuming the shunt resistance to be infinite which reduces the non-linearity of the system. Carrero et al. [24] used an iterative procedure to find all five parameters. Their method only requires the I-V data of three points i.e. the short circuit, open circuit and maximum power points. Their method uses simplified forms of the I-V equation written at the three points and provides fast convergence.

Once the parameters at the reference condition are known, they can be used to calculate the I-V characteristics of the PV module at any other condition. Equations (3.13)-(3.17) are used to calculate the parameters at conditions other than *STC*. Using these parameters, equation (3.3) can be used to predict the performance of the PV module at any temperature and irradiance.

$$a = a_{ref} \, {}^{T_c}\!/_{T_{ref}} \tag{3.13}$$

$$I_L = {}^{S}\!/_{S_{ref}} \left(I_{L,ref} + \mu_{Isc}(T_c - T_{ref}) \right) \tag{3.14}$$

$$I_o = I_{o,ref} \left({}^{T_c}\!/_{T_{ref}} \right)^3 e^{\left(\frac{NCS.T_{ref}}{a_{ref}} \left({}^{E_{g,ref}}\!/_{T_{ref}} - {}^{E_g}\!/_{T_c} \right) \right)} \tag{3.15}$$

$$R_{sh} = \frac{S_{ref}}{S} R_{sh,ref} \tag{3.16}$$

$$R_s = R_{s,ref} \tag{3.17}$$

The subscript *ref* represents the parameters at STC, *T* is the temperature of the PV panel, *S* is the absorbed solar radiation, μ_{Isc} is the temperature coefficient of short circuit current, *NCS* is the number of cells connected in series and E_g is the band-gap energy of the PV cell material (E_g=1.12eV for crystalline silicon, 1.6eV for amorphous silicon and 1.04eV for Copper Indium Selenide).

Equation (3.18) can be used to calculate E_g at the new temperature. The constant 0.0003174 is for mono-crystalline silicon and De Soto [1] suggested that this value can be used for all technologies with little error.

$$E_g = E_{g,ref}\left(1 - 0.0003174\left({T_c}/{T_{ref}}\right)\right) \tag{3.18}$$

3.3 PARAMETERS ESTIMATION FOR FIVE PARAMETERS MODEL USING MULTIVARIABLE OPTIMIZATION

As shown in section 3.2, different methodologies have been used for calculating the model parameters for the five parameter single diode model. In the present study, a new methodology to determine the model parameters was developed. The method uses a multi-variable optimization technique, the Nelder-Mead simplex search algorithm [64], to minimize the error in an objective function by varying the five model parameters. The objective function is defined by equation (3.19).

$$error = \sqrt{\frac{\sum_{i=1}^{3}\left(I_m(V_i) - I_e(V_i)\right)^2}{3}} + \left|\frac{dP}{dV}\right|_{MPP} \tag{3.19}$$

The objective function calculates two errors whose sum is minimized. First, the currents (*I*) at short circuit, maximum power point and open circuit conditions are calculated using equation (3.3) and known voltages from the module datasheet. Newton-Raphson's method was used to solve equation (3.3) for electric current. Once the currents have been calculated, the mean square error in the current predictions is calculated from the current values reported in the datasheet. Second, the slope of the power-voltage (*P-V*) curve is calculated at maximum power point (*MPP*) using the predicted maximum power point current and voltage from the datasheet. Since, the slope should be zero for maximum power, any non-zero value was considered to be an error. Initial guess values were provided for the five parameters and the algorithm calculates the values of the parameters. The tolerance in the error was set to (10^{-3}).

Similar techniques have been used by others as well. Ikegami et al. [25] used a multi-variable optimization technique with experimentally determined I-V points to determine the model parameters. Zagrouba et al. [26] used a genetic algorithm with experimental data to determine the parameters. The proposed approach differs from approaches used by Ikegami et al. [25] and Zagrouba et al. [26] in two ways. First, the proposed method only uses manufacturer supplied data for three points (short circuit, open circuit and maximum power point) on the I-V curve. Second, the objective function used in the proposed method is different from Ikegami et al. [25] and Zagrouba et al. [26].

3.4 ELECTRICAL MODELS SELECTED FOR COMPARISON

Three electrical performance models were selected for comparison with the five parameter model using the developed parameters estimation methodology.

The selected models were:

1. Four parameter electric circuit model [18]
2. Sandia Labs model [2]
3. Villalva et al. electric circuit model [20]

It is important to note here that two of the models selected for comparison, four parameter electric circuit model and Villalva et al. electric circuit model, are variations of the five parameter model and differ from the proposed modeling methodology in either the assumptions involved or the parameter estimation process.

3.4.1 Four Parameter PV Model

Four parameter model is based on the assumption that the shunt resistance is high enough to be considered infinite and neglected. This results in only four unknown parameters and the simplified model is called the four parameter model [18]. The advantage of this model is that with the removal of the fifth parameter, R_{sh}, the nonlinearity in the system of equations used to determine the parameters reduces significantly and its solution is greatly simplified.

The I-V characteristics of the PV system in the four parameter model are described by equation (3.20).

$$I = I_L - I_0\left[\exp\left(\frac{q(V+IR_S)}{\gamma kT_C}\right)-1\right] \tag{3.20}$$

The parameters I_L, I_o and R_s are the same as in the five parameter model. The parameter γ is related to the parameter a in the 5 parameter model by the relation $a=\gamma kT_c/q$. Equations (3.21)-(3.26) were used to determine the parameters for the four parameter model [18]. Writing equation (3.20) for the short circuit, open circuit and maximum power conditions resulted in equations (3.21)-(3.23).

$$I_{L,ref} = I_{sc,ref} \tag{3.21}$$

$$I_{0,ref} = I_{sc,ref}\exp\left(\frac{-qV_{oc,ref}}{k\gamma T_{c,ref}}\right) \tag{3.22}$$

$$\gamma = A.NCS = \frac{q(V_{mp,ref} + I_{mp,ref}R_s - V_{oc,ref})}{kT_{c,ref}\ln(1-(I_{mp,ref}/I_{sc,ref}))} \tag{3.23}$$

To obtain the fourth equation, equation (3.22) was first written in the form of equation (3.24) and then the derivative with respect to temperature was taken resulting in equation (3.25).

$$V_{oc,ref} = \frac{kT_{c,ref}\gamma}{q}\ln\left(\frac{I_{sc,ref}}{I_{0,ref}}\right) \tag{3.24}$$

$$\mu_{voc} = \frac{\gamma k}{q}\left[\ln\left(\frac{I_{sc,ref}}{I_{0,ref}}\right) + \frac{T_{c,ref}\,\mu_{isc}}{I_{sc,ref}} - \left(3 + \frac{qE_g}{AkT_{c,ref}}\right)\right] \tag{3.25}$$

Here, E_g is the material band-gap energy, μ_{Voc} and μ_{Isc} are the temperature coefficients to V_{oc} and I_{sc} and $A=\gamma/NCS$ is the diode ideality factor.

Equation (3.25) was solved using a bisection method to determine R_s where the effect of R_s was introduced in the equation through equation (3.23) for γ. The minimum value of R_s for the bisection method was set to be 0 while its maximum value was determined by setting the ideality factor A equal to 1 in equation (3.26).

$$R_{s,\max} = \frac{1}{I_{mp,ref}}\left[\frac{kT_{c,ref}NCS}{q}\ln\left(1 - \frac{I_{mp,ref}}{I_{sc,ref}}\right) + V_{oc,ref} - V_{mp,ref}\right] \tag{3.26}$$

In the four parameter model, the parameters γ and R_s are assumed to be independent of operating conditions and are assumed constant while I_L and I_o are scaled to the operating conditions using equations (3.14) and (3.15) respectively.

3.4.2 Sandia Labs PV Model

The Sandia Labs PV Model was developed by King et al. [2] and uses empirical correlations and experimentally determined coefficients to predict the performance of the PV system. The accuracy of the model has been demonstrated for modules of all technologies as well as for concentrator modules and for large arrays of modules.

Electrical, thermal, solar spectral and optical effects for photovoltaic modules are all included in the model. The currents and voltages at five points on the I-V curve are calculated by the Sandia Labs model using equations (3.27)-(3.41).

$$I_{sc} = I_{sc0} \cdot f_1(AM_a)\left\{ \left(E_b f_2(AOI) + f_d E_{diff} \right) \Big/ E_0 \right\}\left\{1+\alpha_{isc}(T_c - T_0)\right\} \tag{3.27}$$

$$I_{mp} = I_{mp0}\left\{C_0 E_e + C_1 E_e^{\,2}\right\}\left\{1+\alpha_{imp}(T_c - T_0)\right\} \tag{3.28}$$

$$V_{oc} = V_{oc0} + N_s \delta(T_c)\ln(E_e) + \beta_{voc}(E_e)(T_c - T_0) \tag{3.29}$$

$$\begin{aligned} V_{mp} = {} & V_{mp0} + C_2 N_s \delta(T_c)\ln(E_e) + C_3 N_s\left\{\delta(T_c)\ln(E_e)\right\}^2 \\ & + \beta_{vmp}(E_e)(T_c - T_0) \end{aligned} \tag{3.30}$$

$$P_{mp} = I_{mp} V_{mp} \tag{3.31}$$

$$I_x = I_{x0}\left\{C_4 E_e + C_5 E_e^{\,2}\right\}\left\{1+\alpha_{isc}(T_c - T_0)\right\} \tag{3.32}$$

$$I_{xx} = I_{xx0}\left\{C_6 E_e + C_7 E_e^{\,2}\right\}\left\{1+\alpha_{imp}(T_c - T_0)\right\} \tag{3.33}$$

$$FF = P_{mp} \Big/ (I_{sc} V_{oc}) \tag{3.34}$$

$$E_e = I_{sc} \Big/ \left[I_{sc0}\left\{1+\alpha_{isc}(T_c - T_0)\right\} \right] \tag{3.35}$$

$$\delta(T_c) = nk(T_c + 273.15)/q \tag{3.36}$$

$$E_b = E_{dni}\cos(AOI) \tag{3.37}$$

$$f_1(AM_a) = a_0 + a_1(AM_a) + a_2(AM_a)^2 + a_3(AM_a)^3 + a_4(AM_a)^4 \tag{3.38}$$

$$\begin{aligned} f_2(AOI) = {} & b_0 + b_1(AOI) + b_2(AOI)^2 + b_3(AOI)^3 \\ & + b_4(AOI)^4 + b_5(AOI)^5 \end{aligned} \tag{3.39}$$

$$T_m = E.\left\{e^{a+b.WS}\right\} + T_{amb} \tag{3.40}$$

$$T_c = T_m + \frac{E}{E_0}\Delta T \tag{3.41}$$

3.4.3 Villalva et al. Electric Circuit Model

Villalva et al. [20] developed a model to predict the electrical performance of PV systems based on the equivalent electric circuit of Fig. 3.1. The difference in their model from other models based on the single-diode equivalent circuit is in the methodology for calculating the model parameters. In their methodology, during the parameter estimation process, one of the five parameters, a_{ref}, is explicitly specified. The remaining parameters are calculated using performance data of the PV module available in module datasheet.

An iterative scheme was used to calculate the model parameters at the reference condition. To ease the process of finding the parameters, the parameter a_{ref} was assumed at the beginning of the process and remained unchanged during the algorithm. The parameter I_o was found using equation (3.42). Next, in the iterative algorithm, the resistance R_s was set to an initial values of 0 and R_{sh} was set to an initial value of $R_{sh,min}$ given by equation (3.43).

$$I_{o,ref} = \frac{I_{sc,ref}}{\exp\left({V_{oc,ref}}/{a_{ref}})\right) - 1} \tag{3.42}$$

$$R_{sh,\min} = \frac{V_{mp,ref}}{I_{sc,ref} - I_{mp}} - \frac{V_{oc,ref} - V_{mp}}{I_{mp}} \tag{3.43}$$

The current I_L was calculated using equation (3.44) and the resistance R_{sh} was calculated using equation (3.45).

$$I_{L,ref} = \frac{R_{sh} + R_s}{R_{sh}} I_{sc,ref} \tag{3.44}$$

$$R_{sh,ref} = \frac{V_{mp,ref}(V_{mp,ref} + I_{mp,ref} R_{s,ref})}{\left\{ V_{mp,ref} I_{L,ref} - V_{mp,ref} I_{o,ref} \exp\left[\frac{(V_{mp,ref} + I_{mp,ref} R_{s,ref})}{a_{ref}} \right] + V_{mp,ref} I_{o,ref} - P_{\max,e} \right\}} \tag{3.45}$$

To calculate the maximum power, equation (3.3) was solved for current for the entire range of voltages from 0 to the open circuit voltage V_{oc} and the maximum power was found by multiplying the currents and voltages and searching for the maximum value. If the error of the predicted power from the experimental value were within the specified tolerance, the solution terminated otherwise the value for R_s was incremented and the process was repeated.

Once the parameters at the reference condition are known, they can be translated on to the operating condition using equations (3.13)-(3.17). Villalva et al. suggested that using equation (3.46) to translate I_o can improve the accuracy of the model.

$$I_o = \frac{I_{sc,ref} + \mu_{isc}(T_c - T_{ref})}{\exp\left({(V_{oc,ref} + \mu_{voc}(T_c - T_{ref}))} \big/ {a} \right) - 1} \tag{3.46}$$

3.5 COMPARISON OF ELECTRICAL MODELS

In order to validate the proposed parameter estimation methodology and to compare its accuracy with the accuracy of models available in literature, a total of six PV modules, three crystalline silicon modules and three thin film modules, were selected. The I-V curves available in the datasheets of the modules were digitized and five key I-V points were extracted from each curve. These points are short circuit (*SC*), open circuit (*OC*), maximum power point (*MPP*), point with voltage equal to half the voltage at maximum power point (*X*) and point with voltage equal to the average of maximum power point voltage and open circuit voltage (*XX*).

3.5.1 Selected PV modules

The PV modules selected for model validation are listed below. The manufacturer supplied electrical performance characteristics of the modules at STC are listed in Table 3.1. The I-V points for crystalline silicon and thin film modules which are extracted from the I-V curves on the module datasheets are listed in Table 3.2 and Table 3.3 respectively.

1. Astro Power AP110 (mc-Si)
2. Shell Solar S36 (pc-Si)
3. Kyocera KC-40T (pc-Si)
4. Shell Solar ST36 (CIS)
5. Solarex MST43LV (2-a-Si)
6. Unisolar PVL-124 (3-a-Si)

Table 3.1. Electrical characteristics of the selected modules at STC.

	AP-110	**S-36**	**KC-40T**	**ST-36**	**MST43-LV**	**PVL-124**
Short Circuit Current (I_{sc})	7.5	2.3	2.65	2.68	3.3	5.1
Open Circuit Voltage (V_{oc})	20.7	21.4	21.7	22.9	22.7	42
MPP Current (I_{mp})	6.6	2.182	2.48	2.28	2.6	4.13
MPP Voltage (V_{mp})	16.7	16.5	17.4	15.8	16.5	30
Number of Cells in series (*NCS*)	36	36	36	42	16	20
I_{sc} temperature coefficient (μ_{Isc})	0.0034	0.001	0.00106	0.00032	0.00066	0.001
V_{oc} temperature coefficient (μ_{Voc})	-0.08	-0.076	-0.0821	-0.1	-0.1	-0.0038

Table 3.2. Extracted I-V points for crystalline silicon modules.

	AP-110		**S36**		**KC-40T**	
Point	*V*	*I*	*V*	*I*	*V*	*I*
	1000 W/m^2 and 25°C		**1000 W/m^2 and 25°C**		**1000 W/m^2 and 25°C**	
SC	0.00	7.50	0.00	2.30	0.00	2.65
X	8.35	7.30	8.25	2.29	8.70	2.61
MPP	16.70	6.60	16.50	2.18	17.40	2.48
XX	18.70	4.60	18.95	1.53	19.55	1.82
OC	20.70	0.00	21.40	0.00	21.70	0.00
	1000 W/m^2 and 60°C		**1000 W/m^2 and 60°C**		**1000 W/m^2 and 50°C**	
SC	0.00	7.70	0.00	2.33	0.00	2.74
X	6.46	7.43	7.26	2.33	7.69	2.70
MPP	12.92	6.70	14.52	2.09	15.38	2.55
XX	15.13	3.88	16.64	1.44	17.49	1.78
OC	17.34	0.00	18.75	0.00	19.6	0.00
	800 W/m^2 and 45°C		**400 W/m^2 and 25°C**		**400 W/m^2 and 25°C**	
SC	0.00	6.00	0.00	0.92	0.00	1.22
X	7.33	5.88	8.25	0.89	8.32	1.21
MPP	14.65	4.98	16.54	0.84	16.64	1.15
XX	16.41	3.54	18.41	0.64	18.82	0.82
OC	18.18	0.00	20.27	0.00	20.99	0.00

Table 3.3. Extracted I-V points for thin film modules.

	PVL-124		**ST36**		**MST43LV**	
Point	*V*	*I*	*V*	*I*	*V*	*I*
	1000 W/m^2 and 25°C		**1000 W/m^2 and 25°C**		**1000 W/m^2 and 25°C**	
SC	0.00	5.10	0.00	2.68	0.00	3.30
X	15.00	4.98	7.90	2.65	8.25	3.10
MPP	30.00	4.13	15.80	2.28	16.50	2.60
XX	36.00	2.62	19.35	1.49	19.60	1.75
OC	42.00	0.00	22.90	0.00	22.70	0.00
	600 W/m^2 and 25°C		**400 W/m^2 and 25°C**		**250 W/m^2 and 25°C**	
SC	0.00	3.07	0.00	1.07	0.00	0.88
X	14.7	3.03	7.77	1.06	8.15	0.77
MPP	29.4	2.62	15.53	0.89	16.30	0.67
XX	35.24	1.71	18.25	0.61	18.46	0.52
OC	41.09	0.00	20.96	0.00	20.61	0.00
	200 W/m^2 and 25°C		**1000 W/m^2 and 60°C**			
SC	0.00	1.06	0.00	2.72		
X	14.74	1.04	6.36	2.68		
MPP	29.47	0.91	12.71	2.18		
XX	34.04	0.66	16.10	1.35		
OC	38.60	0.00	19.50	0.00		

3.5.2 Error Statistics

Two metrics were selected to compare the PV models. These were the root mean square error (*RMSE*) and the mean bias error (*MBE*) given by equations (3.47) and (3.48) respectively. In these equations, *y* is the modeled value, *x* is the measured value and *n* is the number of values.

$$RMSE = \frac{\frac{1}{n}\sqrt{\sum_{i=1}^{n}(y_i - x_i)^2}}{\frac{1}{n}\sum_{i=1}^{n}x_i} \tag{3.47}$$

$$MBE = \frac{\frac{1}{n}\sum_{i=1}^{n}(y_i - x_i)}{\frac{1}{n}\sum_{i=1}^{n}x_i} \tag{3.48}$$

The root mean square error is used to check the accuracy of the model in predicting actual measured values. The mean bias error, on the other hand, does not represent the accuracy of the model. Rather it is used to check whether the model over-predicts or under-predicts the performance.

3.5.3 Parameters Calculation for the Selected Modules

Before the electrical performance of the modules was simulated, the model parameters for the modules were determined. The procedures to determine the parameters for the five parameters model using the proposed methodology is described in section 3.3. The procedure to determine the parameters for the 4 Parameter model and Villalva et al. model are described in sections 3.4.1 and 3.4.3 respectively. The parameters determined using the proposed method for the five parameter model at STC are listed in Table 3.4, parameters for the four parameter model at STC are listed in Table 3.5 and the parameters for the Villalva et al. model are listed in Table 3.6. The parameters for the Sandia Labs PV Model are experimentally determined and were obtained from the parameters library in the System Advisor Model (*SAM*) software available from the National Renewable Energy Labs website and have been listed in Table 3.7.

Table 3.4. Parameters for the Five Parameter Model (Proposed) at STC.

Parameter	**AP-110**	**S-36**	**KC-40T**	**ST-36**	**MST-43LV**	**PVL-124**
$I_{L,ref}$	7.5084	2.3199	2.6540	2.7148	3.5075	5.3001
$I_{o,ref}$	3.4686e-6	9.8279e-7	1.3503e-8	9.2532e-7	2.33e-16	1.14e-23
a_{ref}	1.4249	1.4587	1.1366	1.5451	0.6141	0.7726
$R_{s,ref}$	0.0527	0.4235	0.4747	1.6187	1.6270	2.5023
$R_{sh,ref}$	46.8713	2002.273	2117.7476	124.7165	25.8786	63.7659

Table 3.5. Parameters for the Four Parameter Model at STC.

Parameter	**AP-110**	**S-36**	**KC-40T**	**ST-36**	**MST-43LV**	**PVL-124**
$I_{L,ref}$	7.5	2.3	2.65	2.68	3.3	5.1
$I_{o,ref}$	3.0176e-6	1.3873e-7	7.1599e-8	1.9691e-4	1.1114e-4	9.9250e-5
γ_{ref}	54.7192	50.1118	48.4726	93.6517	85.8243	150.72
$R_{s,ref}$	0.1545	0.4934	0.3548	1.1070	1.0697	1.35

Table 3.6. Parameters for Villalva et al. Model at STC.

Parameter	**AP-110**	**S-36**	**KC-40T**	**ST-36**	**MST-43LV**	**PVL-124**
$I_{L,ref}$	7.516	2.3015	2.6511	2.711	3.3714	5.1838
$I_{o,ref}$	2.50335e-7	4.289e-8	3.8505e-8	2.181e-7	2.0643e-18	2.5232
a_{ref}	1.2018	1.2018	1.2018	1.4021	0.5341	0.6677
$R_{s,ref}$	0.0707	0.5	0.3368	0.5	0.5	0.5
$R_{sh,ref}$	33.079	769.4	807.9666	43.1282	23.092	30.43

Table 3.7. Parameters for the Sandia Labs PV Model.

Parameter	**AP-110**	**S-36**	**KC-40T**	**ST-36**	**MST-43LV**	**PVL-124**
NCS	36	36	36	42	16	20
NP	1	1	1	1	4	1
I_{sc0}	7.5000	2.3000	2.6500	2.6800	3.5300	5.1000
V_{oc0}	20.7000	21.4000	21.7000	22.9000	22.2700	42.0000
I_{mp0}	6.6000	2.1800	2.4800	2.2800	2.5700	4.1300
V_{mp0}	16.7000	16.5000	17.4000	15.8000	16.6700	30.0000
α_{isc}	3.3000E-04	4.50E-04	4.00E-04	-1.3000E-05	6.600E-04	1.00E-03
α_{imp}	-4.2000E-04	-1.40E-04	-1.40E-04	-4.5000E-04	9.500E-04	1.00E-03
C_0	0.9970	0.9890	1.0060	0.9720	1.0227	1.0960
C_1	0.0030	0.0110	-0.0060	0.0280	-0.0227	-0.0960
β_{voc}	-8.4000E-02	-7.60E-02	-8.21E-02	-9.0600E-02	-1.050E-01	-1.60E-01
$m_{\beta voc}$	0.0000	0.0000	0.0000	0.0000	0.0000	0.0000
β_{vmp}	-8.4000E-02	-7.60E-02	-8.40E-02	-7.4400E-02	-8.700E-02	-9.30E-02
$m_{\beta vmp}$	0.0000	0.0000	0.0000	0.0000	0.0000	0.0000
n	1.4040	1.3700	1.3700	1.7520	3.5480	3.7700
C_2	-0.1775	-0.1170	-0.1170	0.5088	-0.2203	-1.1416
C_3	-11.0652	-11.0820	-11.0820	-2.9540	-4.0595	-2.8912
a_0	9.1800E-01	9.22E-01	9.22E-01	9.2100E-01	8.937E-01	1.05E+00
a_1	6.8713E-02	7.09E-02	7.09E-02	7.1815E-02	1.416E-01	8.21E-04

a_2	-1.0438E-02	-1.43E-02	-1.43E-02	-1.4619E-02	-5.539E-02	-2.59E-02
a_3	7.2504E-04	1.17E-03	1.17E-03	1.2500E-03	5.613E-03	3.17E-03
a_4	2.0182E-05	-3.37E-05	-3.37E-05	-3.7406E-05	-1.770E-04	-1.10E-04
b_0	1.0000E+00	1.00E+00	1.00E+00	1.0000E+00	1.000E+00	1.00E+00
b_1	-2.4380E-03	-2.47E-03	-2.44E-03	-2.4380E-03	-2.438E-03	-5.02E-03
b_2	3.1030E-04	3.15E-04	3.10E-04	3.1030E-04	3.103E-04	5.84E-04
b_3	-1.2460E-05	-1.26E-05	-1.25E-05	-1.2460E-05	-1.246E-05	-2.30E-05
b_4	2.1120E-07	2.14E-07	2.11E-07	2.1120E-07	2.112E-07	3.83E-07
b_5	-1.3590E-09	-1.37E-09	-1.36E-09	-1.3590E-09	-1.359E-09	-2.31E-09
ΔT	3.0000	3.0000	3.0000	3.0000	3.0000	1.0000
F_d	1.0000	1.0000	1.0000	1.0000	1.0000	1.0000
a	-3.5600	-3.5370	-3.5600	-3.4700	-3.4700	-2.8100
b	-0.0750	-0.0721	-0.0750	-0.0594	-0.0594	-0.0455
C_4	0.9840	0.9866	0.9866	0.9829	1.0124	1.0440
C_5	0.0160	0.0134	0.0134	0.0171	-0.0124	-0.0440
I_{x0}	7.3000	2.2600	2.6100	2.5900	3.2100	4.7200
I_{xx0}	4.6000	1.5300	1.7400	1.5800	1.7700	2.9000
C_6	1.1230	1.1183	1.1183	1.0450	1.1185	1.1300
C_7	-0.1230	-0.1183	-0.1183	-0.0450	-0.1185	-0.1300

3.5.4 Comparison of Electrical Models - Results

The electrical performance of the six selected PV modules as predicted by the five parameters model using the proposed parameter estimation methodology and the three selected models from literature was calculated at the absorbed radiation and cell temperature conditions listed in Table 3.2. From the results of these calculations, the root mean square error and mean bias error were calculated for the currents and voltages at the five key points and for maximum power. The model errors in currents and voltages at the five key points are shown in Fig. 3.2 and Fig. 3.3 respectively. Fig. 3.4 shows the error in the prediction of maximum power for each module. The results in these figures show that the five parameters model using the proposed parameter estimation methodology performs satisfactorily compared to the four parameter model and the Sandia Labs model with some instances in which it shows better accuracy than the two and some instances in which it shows larger errors than them. The five parameter model provided better results when the parameters estimated using the new methodology were used, especially for thin film module. For thin film modules, Villalva et al. model showed much larger errors although it differs from the proposed model in the methodology for estimating the model parameters. This signifies the importance of the parameter estimation process for accurate model prediction.

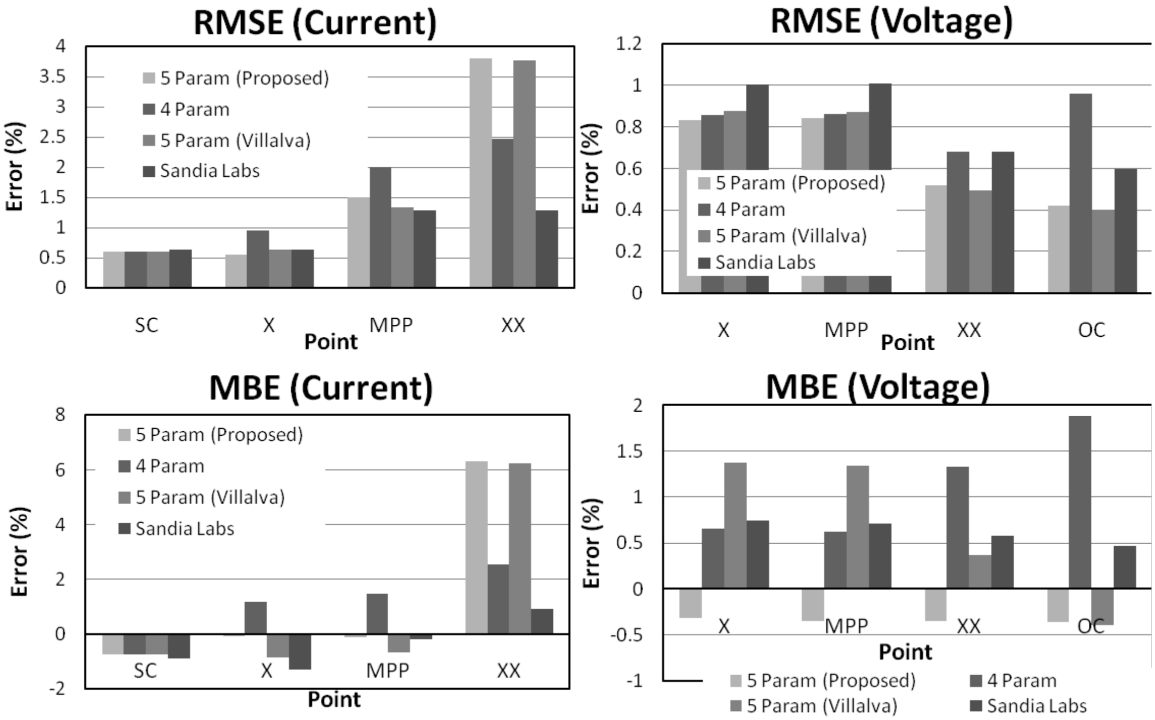

Fig. 3.2. Crystalline Silicon Modules Current and Voltage Errors.

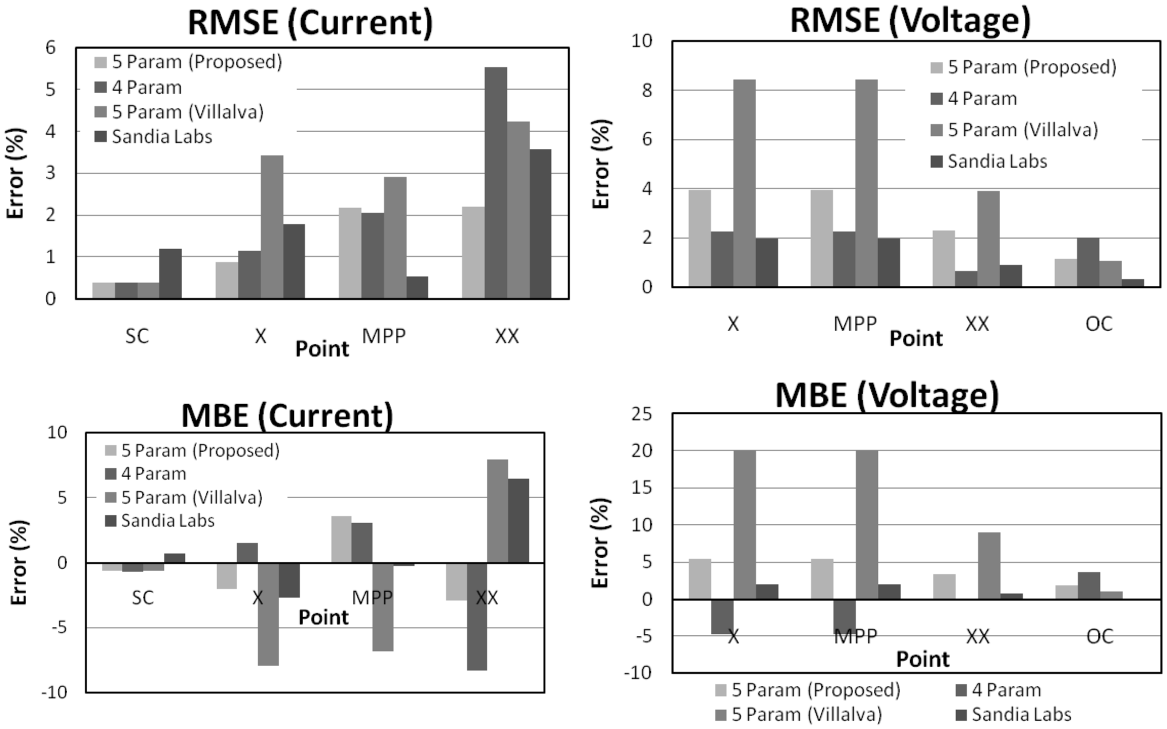

Fig. 3.3. Thin Film Modules Current and Voltage Errors.

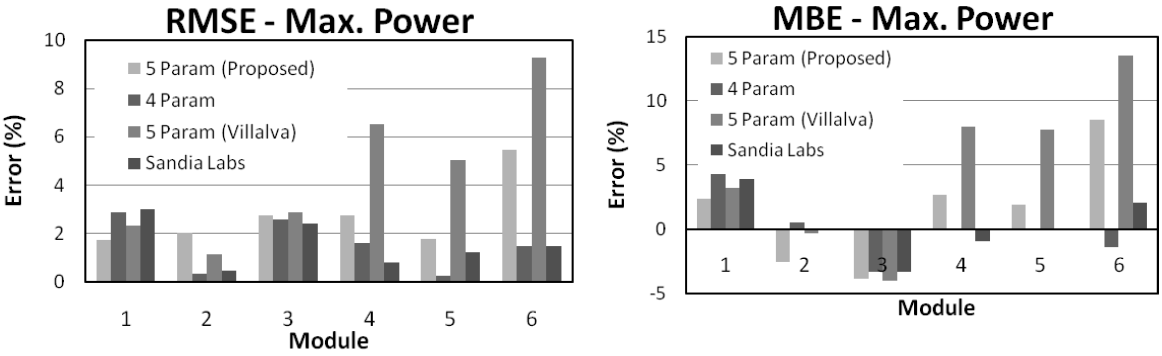

Fig. 3.4. Maximum Power prediction errors. (Module 1=AP-110, Module 2=S-36, Module 3=KC-40T, Module 4=MST-43LV, Module 5=ST-35, Module 6=PVL-124)

3.6 SENSITIVITY ANALYSIS OF 5 PARAMETER MODEL

To identify the relative importance of the five model parameters, a sensitivity analysis was carried out in which normalized sensitivity coefficients were calculated for each model parameter. This allows a one-to-one comparison between the model parameters. Masi et al. [65] explained the physical significance of the normalized sensitivity coefficients as the order of magnitude change in the analyzed function that will result from one order of magnitude change in the concerned parameter. Thus, normalized sensitivity coefficients are used to identify the model parameters to which the model is most sensitive. The normalized sensitivity coefficients (*NSCs*) are given by equation (3.49), where $\bar{Y}$ is nominal value of the function at nominal model parameters $\bar{X}_i$ and ΔY is the change in the function value to due to a change of ΔX_i in the model parameter X_i. For the five parameter model, the maximum power output of the PV panel is considered to be the function Y and X_i are the five model parameters (I_L, I_o, a, R_s and R_{sh}). Sensitivity analysis was carried out using the module data and parameters for the AP-110 PV module and the results of the analysis are shown in Table 3.8. In the table, the values $X+$ and $X-$ show 10% increase and decrease in the parameter X respectively while $Y+$ and $Y-$ show the corresponding values of the function Y. It is clear from the table that the electrical power prediction using the model is clearly more sensitive to two model parameters, I_L and a. In order to check whether the normalized sensitivity coefficients vary with irradiance and cell temperature, the analysis was repeated by changing the absorbed radiation and the cell temperature. The results are shown in Fig. 3.5 which shows that within the ranges of absorbed radiation and cell temperatures considered, the relative importance of the five parameters does not change.

$$NSC_i = \frac{\Delta Y}{\bar{Y}} \frac{\overline{X}_i}{\Delta X_i} \tag{3.49}$$

Table 3.8. Normalized Sensitivity Analysis results for the Five Parameter Model.

Parameter	**X**	**X+**	**X-**	**Y+**	**Y-**	**ΔX_i**	**ΔY_i**	**NSC*i***
I_L	7.508	8.259	6.758	122.500	98.020	1.502	24.480	1.223
I_o	3.47E-6	3.82E-6	3.12E-6	109.4	111.1	6.94E-7	1.7	5.90E-3
a	1.425	1.567	1.282	120.80	99.480	0.285	21.320	0.927
R_s	0.053	0.058	0.047	109.90	110.500	0.011	0.600	7.34E-4
R_{sh}	46.871	51.558	42.184	110.80	109.500	9.374	1.300	3.45E-3

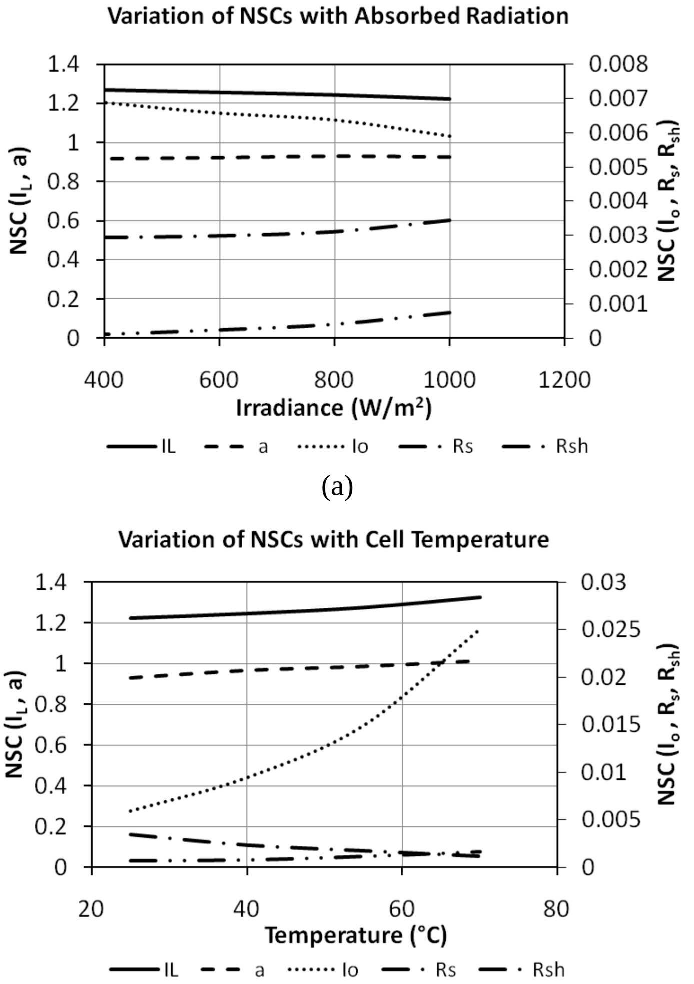

(a)

(b)

Fig. 3.5. Variation of Normalized Sensitivity Coefficients with (a) Absorbed Radiation and (b) PV Cell Temperature.

3.7 PROPOSED SEVEN PARAMETER ELECTRICAL MODEL

Boyd [12] attempted to improve the five parameter model by introducing two new parameters m and δ to the translation equations for I_o and R_s. The improvements did not provide satisfactory results with errors remaining the same or sometimes even increasing when the new parameters were introduced, especially in the maximum power prediction. These observations agree with the results of the sensitivity analysis carried out here which show that the maximum power prediction is not very sensitive to I_o and R_s. In the present work, modifications to the model based on the results of the sensitivity analysis were attempted to improve the model accuracy. Using an approach similar to Boyd [12], modifications were made in the translation equations of parameters I_L and a to which the model prediction is most sensitive to. In total, five possible improvements to the translation equations were attempted.

Table 3.9 shows the five modifications to the translation equations of I_L and a considered here.

Table 3.9. Modifications to translation equations for I_L and *a*.

Model	**Translation Equation for I_L**	**Translation Equation for *a***
7 Parameters (I_L and a)	$I_L = \left({}^{S}\!/\!{}_{S_{ref}} \right)^m \left(I_{L,ref} + \mu_{Isc}(T_c - T_{ref}) \right)$	$a = a_{ref} \left({}^{T_c}\!/\!{}_{T_{ref}} \right)^n$
6 Parameters (m)	$I_L = \left({}^{S}\!/\!{}_{S_{ref}} \right)^m \left(I_{L,ref} + \mu_{Isc}(T_c - T_{ref}) \right)$	$a = a_{ref} \left({}^{T_c}\!/\!{}_{T_{ref}} \right)$
6 Parameters (n)	$I_L = \left({}^{S}\!/\!{}_{S_{ref}} \right) \left(I_{L,ref} + \mu_{Isc}(T_c - T_{ref}) \right)$	$a = a_{ref} \left({}^{T_c}\!/\!{}_{T_{ref}} \right)^n$
7 Parameters (a)	$I_L = \left({}^{S}\!/\!{}_{S_{ref}} \right) \left(I_{L,ref} + \mu_{Isc}(T_c - T_{ref}) \right)$	$a = a_{ref} \left({}^{S}\!/\!{}_{S_{ref}} \right)^m \left({}^{T_c}\!/\!{}_{T_{ref}} \right)^n$
7 Parameters (I_L)	$I_L = \left({}^{S}\!/\!{}_{S_{ref}} \right)^m \left(I_{L,ref} + \left(\mu_{Isc} \right)^n (T_c - T_{ref}) \right)$	$a = a_{ref} \left({}^{T_c}\!/\!{}_{T_{ref}} \right)$

In all the modifications considered, the new parameters (m and n) were estimated using a secondary optimization routine that used the sum of the root mean square errors in maximum power prediction at a low irradiance condition and at a high temperature as the objective function to be minimized. The objective function for the secondary optimization is given by equation (3.50).

$$error = \sqrt{\left(P_m - P_e\right)^2}\Big|_{Low\,Irradiance} + \sqrt{\left(P_m - P_e\right)^2}\Big|_{High\,Temeprature} \qquad (3.50)$$

where P is the electrical power output of the PV panel. Subscripts m and e stand for modeled and experimental values respectively. The new information about the PV module required for the estimation process includes the maximum power of the PV module at a low irradiance value and the temperature coefficients of either I_{mp} and V_{mp} or P_{mp}. The additional information for the six modules considered here is given in Table 3.10. It is important to note that values of the original five parameters remain unchanged when the new parameters are introduced. The effect of the five modifications on the maximum power prediction accuracy of the six modules considered here is shown in Table 3.11.

Table 3.10. Module information required for parameters *m* and *n*.

Module	**Low Irradiance Data**			**Temperature Coefficient of I_{MP} (A/°C)**	**Temperature Coefficient of V_{MP} (A/°C)**
	Input Condition	I_{MP}(A)	V_{MP}(V)		
AP-110	800 W/m^2, 45°C	4.975	14.653	-0.00042	-0.084
S-36	400 W/m^2, 25°C	0.835	16.54	-0.00014	-0.076
KC-40T	400 W/m^2, 25°C	1.15	16.64	-0.00014	-0.084
MST-43LV	250 W/m^2, 25°C	0.67	16.30	0.00095	-0.087
ST-36	400 W/m^2, 25°C	0.894	15.53	-0.00045	-0.074
PVL-124	200 W/m^2, 25°C	0.909	29.472	0.001	-0.093

Table 3.11. Effect of the translation equations modification on maximum power prediction accuracy (RMSE).

Model	**Module 1**	**Module 2**	**Module 3**	**Module 4**	**Module 5**	**Module 6**
Original	1.755	2.054	2.746	2.751	1.760	5.456
7 Parameters (I_L and a)	1.426	0.378	1.284	0.003	0.942	3.037
6 Parameters (m)	0.889	2.041	1.654	0.051	0.247	2.983
6 Parameters (n)	2.315	0.466	2.542	2.751	3.160	5.486
7 Parameters (a)	1.419	0.407	1.287	0.048	3.150	2.396
7 Parameters (I_L)	1.425	0.404	1.285	0.051	2.583	2.988

Only the *seven parameter model (I_L and a)*, henceforth referred to as only the seven parameter model, provided consistent and significant improvement for all PV modules. Therefore, the best modifications to the translation equations of I_L and a are given by equations (3.51) and (3.52). The values of the two new parameters (m and n) required in the new seven parameters model for the PV modules considered in the present study are listed in Table 3.12.

$$I_L = \left(G / G_{ref} \right)^m \left(I_{L,ref} + \mu_{Isc} (T_c - T_{ref}) \right) \tag{3.51}$$

$$a = a_{ref} \left(T_c / T_{ref} \right)^n \tag{3.52}$$

Table 3.12. Parameters m and n for the selected PV modules.

Module	**m**	**n**
AP-110	1.0959	1.1368
S-36	0.9865	1.4144
KC-40T	0.8706	1.1157
MST-43LV	1.0736	-0.0887
ST-36	1.0959	1.1368
PVL-124	1.1137	-0.0010

3.7.1 Comparison of Proposed Seven Parameters Model with Other Models

A comparison of the maximum power prediction accuracy between the five parameter model using the parameters estimated using the new proposed methodology and the seven parameter model was carried out and is shown in Fig. 3.6. The introduction of the two new parameters in the model resulted in marked improvement in the maximum power prediction accuracy of all the considered modules. A comparison of the new seven parameter model with the three models from literature considered here is shown in Figs. 3.7 to 3.9. Figs. 3.6 to 3.9 show that the introduction of the new parameters results in much more accurate results than the five parameter model.

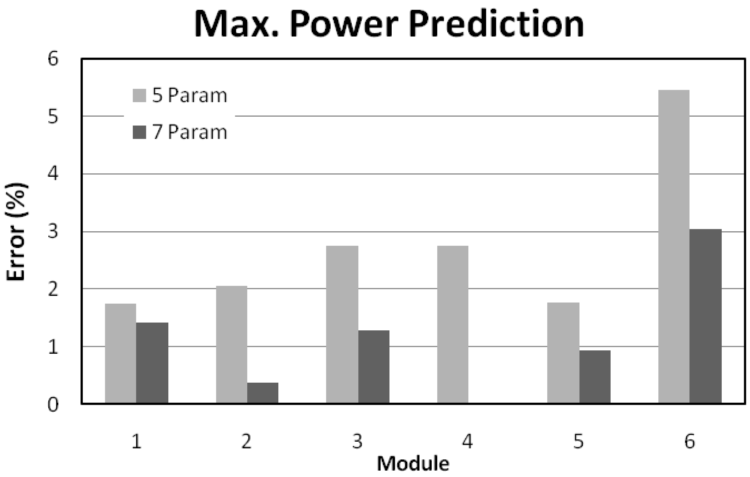

Fig. 3.6. Comparison of Maximum Power prediction accuracy (RMSE) of five parameter model and seven parameter model. (Module 1=AP-110, Module 2=S-36, Module 3=KC-40T, Module 4=MST-43LV, Module 5=ST-35, Module 6=PVL-124)

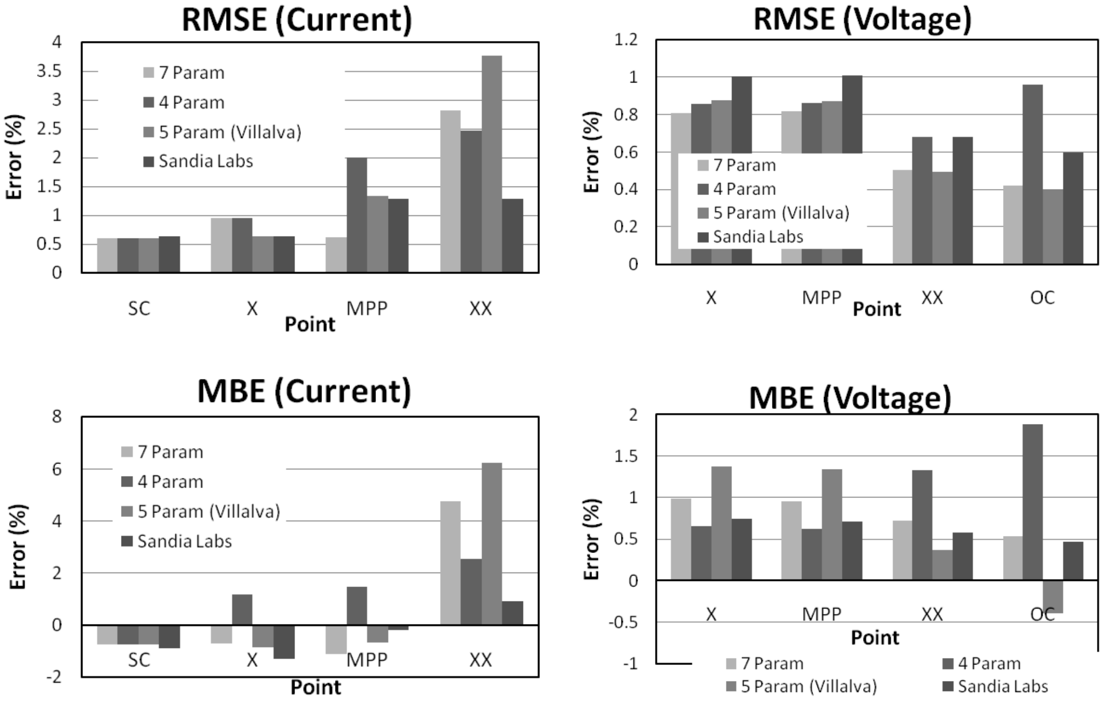

Fig. 3.7. Comparison of accuracy of seven parameter model for crystalline silicon technology.

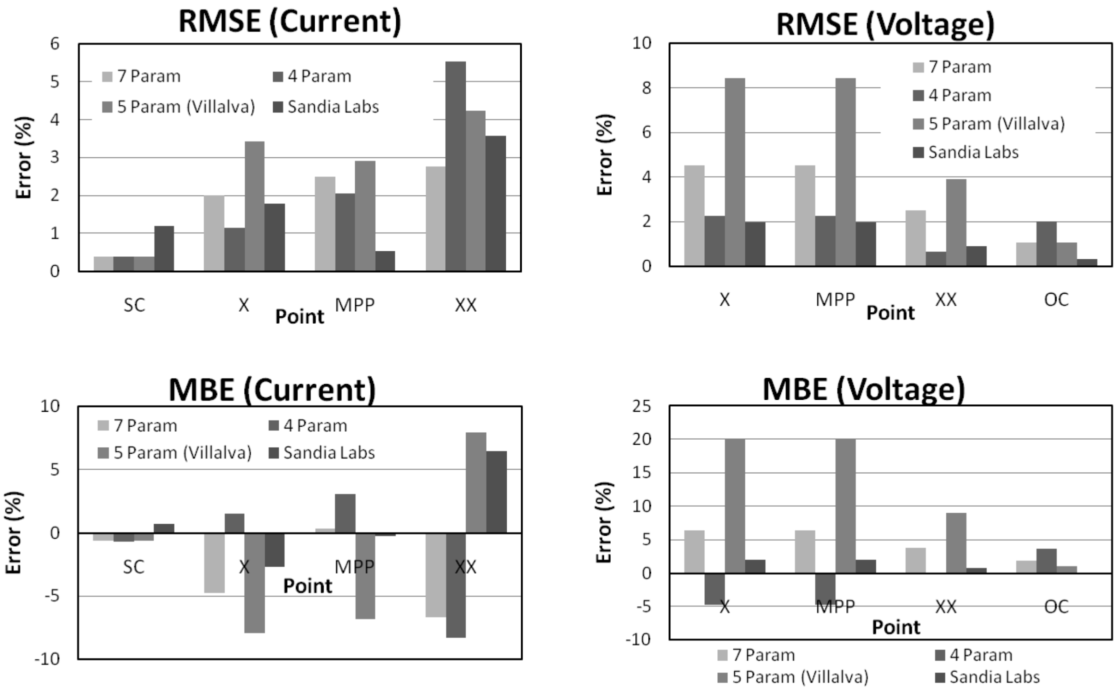

Fig. 3.8. Comparison of accuracy of seven parameter model for thin film technology.

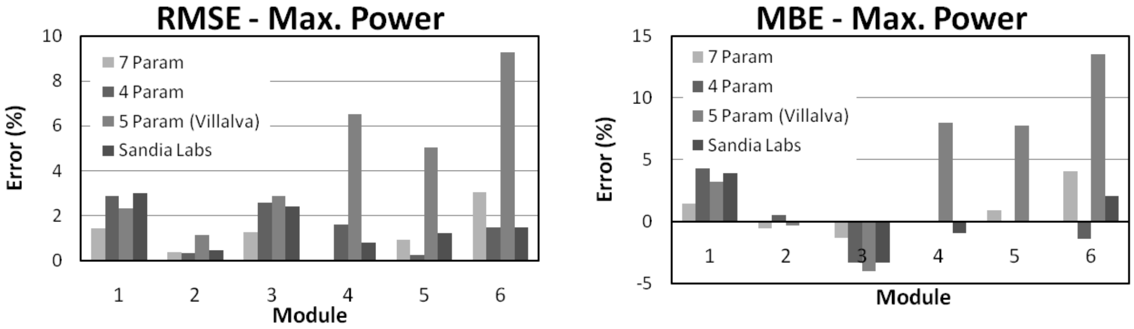

Fig. 3.9. Comparison of Maximum Power prediction accuracy for seven parameter model. (Module 1=AP-110, Module 2=S-36, Module 3=KC-40T, Module 4=MST-43LV, Module 5=ST-35, Module 6=PVL-124)

In order to confirm the accuracy of the seven parameter model, the model was used to predict the maximum power of two new PV modules. These included Sanyo's propriety HIT technology module, HIT-195, which combines mono-crystalline silicon and amorphous silicon in a layered arrangement and Suntech's STP090T amorphous silicon module. The RMSE in the maximum power prediction for HIT-195 and STP090T modules using the seven Parameter model was found to be 0.91% and 2.32% respectively.

3.8 CONCLUSIONS

In this chapter, a novel methodology for estimating the model parameters for the five parameters PV model and a new seven parameter PV model based on the results of a sensitivity analysis have been presented. The following conclusions were drawn from the conducted studies.

- Comparison of the five parameter model using the new parameters estimation methodology with other electrical models showed that the new methodology provided comparable results to other models and better results than the five parameter model using the parameters estimated by the methodology of Villalva et al. [20] for crystalline silicon as well as thin film PV cell types.
- The results of the sensitivity analysis showed that the five parameter model is several orders of magnitude more sensitive to the parameters I_L and a than the remaining three parameters.

- The proposed seven parameter model showed improvement in the prediction accuracy for all modules considered in the study. In the future, there is a need to test the proposed seven parameter model with experimental data to further validate its accuracy.

CHAPTER 4

RADIATION AND OPTICAL MODELING

4.1 INTRODUCTION

Radiation and optical models are used to calculate radiation absorbed in PV modules from solar irradiance data measured on the horizontal plane. This absorbed radiation is then used in the electrical model to calculate the electrical output of the system and in the thermal model to calculate the temperature distribution in the PV panel.

In the present work, no new radiation model was developed. Instead, four of the most commonly used radiation models were implemented. In this chapter, the details of these four radiation & optical models used to calculate solar irradiance absorbed in PV modules is presented. A results of a study conducted to select the model with the least error have also been presented in the chapter.

4.2 RADIATION & OPTICAL MODELING

The Radiation & Optical models implemented in the present work are a combination of two separate models, a radiation model to calculate plane of array (*POA*) irradiance from measured horizontal solar irradiance and an optical model to calculate the amount of the *POA* irradiance that gets absorbed in the PV module.

4.2.1 Optical Model

The optical model used to calculate the transmitivity-absorptivity product ($\tau\alpha$) is given by Eq. (4.1) where θ and θ_r are the incidence and refraction angles, K is the extinction coefficient and L is the thickness of the glass cover [14]. The ($\tau\alpha$) product is then used to calculate the incidence angle modifiers ($K_{\tau\alpha}$) using Eq. (4.2). It is important to note that separate incidence angle modifiers are needed for beam, diffuse and ground reflected components of the incident solar radiation.

$$\tau\alpha(\theta) = e^{-(KL/\cos\theta_r)}\left[1-\frac{1}{2}\left(\frac{\sin^2(\theta_r-\theta)}{\sin^2(\theta_r+\theta)}+\frac{\tan^2(\theta_r-\theta)}{\tan^2(\theta_r+\theta)}\right)\right] \tag{4.1}$$

$$K_{\tau\alpha}(\theta) = \frac{\tau\alpha(\theta)}{\tau\alpha(0)} \tag{4.2}$$

4.2.2 Radiation Models

Four radiation models were implemented in the present work. These models differ from each other in the complexity of their treatment of the diffuse component of the solar radiation. The simplest one of the four is the Isotropic Sky Model. The Isotropic sky radiation model was presented by Liu and Jordan [8,66] and assumes that the diffuse radiation is isotropic over the entire sky dome. The model includes separate treatment for the beam, isotropic diffuse and ground reflected components of incoming solar radiation.

The model is given by Eq. (4.3). In this and all of the other three models, the optical model is integrated in the form of $K_{\tau\alpha}$ modifiers being included in the model equations.

$$\begin{aligned}\frac{S}{S_{ref}} &= M\frac{G_b}{G_{ref}}R_{beam}K_{\tau\alpha,b} + M\frac{G_d}{G_{ref}}K_{\tau\alpha,d}\frac{1+\cos\beta}{2} \\ &+M\frac{G}{G_{ref}}\rho K_{\tau\alpha,g}\frac{1-\cos\beta}{2}\end{aligned} \tag{4.3}$$

where subscripts *b*, *d* and *g* refer to the beam, diffuse and ground reflected radiation components, β is the slope of the PV panel and ρ is the ground reflectance.

Hay & Davies model [13,66] is an improvement to the isotropic sky model because it considers an additional component of the diffuse radiation i.e. the circumsolar diffuse radiation. In this model, it is assumed that all of the circumsolar radiation comes from the same direction as the beam radiation. The model is represented by Eq. (4.4). The factor A_i is called the Anisotropy index and is given by Eq. (4.5).

$$\begin{aligned}\frac{S}{S_{ref}} &= M\frac{G_b + A_i G_d}{G_{ref}}R_{beam}K_{\tau\alpha,b} + M\frac{(1-A_i)G_d}{G_{ref}}K_{\tau\alpha,d}\frac{1+\cos\beta}{2} \\ &+M\frac{G}{G_{ref}}\rho K_{\tau\alpha,g}\frac{1-\cos\beta}{2}\end{aligned} \tag{4.4}$$

$$A_i = \frac{G_b}{G_o} \tag{4.5}$$

The Hay & Davies model was improved by Reindl et al. [10,66] to include the final component of diffuse radiation i.e. the horizon brightening diffuse radiation which led to the development of the Hay-Davies-Reindl-Klutcher (*HDKR*) model. The horizon brightening component was assumed to be coming from the same direction as the isotropic diffuse radiation in the *HDKR* model. The model is given by Eq. (4.6)

$$
\begin{aligned}
\frac{S}{S_{ref}} &= M\,\frac{G_b + A_i G_d}{G_{ref}} R_{beam} K_{\tau\alpha,b} \\
&+ M\,\frac{(1-A_i)G_d}{G_{ref}} K_{\tau\alpha,d}\left(\frac{1+\cos\beta}{2}\right)\left(1+f\sin^3\left(\frac{\beta}{2}\right)\right) \\
&+ M\,\frac{G}{G_{ref}} \rho K_{\tau\alpha,g}\left(\frac{1-\cos\beta}{2}\right)
\end{aligned}
\tag{4.6}
$$

where the factor *f* is given by Eq. (4.7).

$$
f = \sqrt{\frac{G_b}{G}} \tag{4.7}
$$

The final radiation model implement in the present work was developed by Perez et al. [11] who presented an empirical model to calculate the incident radiation on sloped surfaces which included all diffuse radiation components. In this study, their model for incident radiation was modified to calculate the absorbed solar radiation in the PV cells in a manner similar to the previous three models. The model for calculating absorbed solar radiation using the Perez model is given by Eq. (4.8).

$$
\begin{aligned}
\frac{S}{S_{ref}} &= M\,\frac{G_b R_{beam} + F_1 G_d \, {}^{a}\!/_{b}}{G_{ref}} K_{\tau\alpha,b} \\
&+ M\left\{\frac{(1-F_1)G_d}{G_{ref}}\,\frac{1+\cos\beta}{2} + \frac{G_d F_2 \sin\beta}{G_{ref}}\right\} K_{\tau\alpha,d} \\
&+ M\,\frac{G}{G_{ref}} \rho K_{\tau\alpha,g}\,\frac{1-\cos\beta}{2}
\end{aligned}
\tag{4.8}
$$

To calculate F_1 and F_2, Eqs. (4.9)-(4.12) are used where f_{11}, f_{12}, f_{13}, f_{21}, f_{22} *and* f_{23} are empirical constants determined by Perez et al. [7].

$$\begin{aligned} a &= \max(0, \cos\theta) \\ b &= \max(\cos 85, \cos\theta_z) \end{aligned} \tag{4.9}$$

$$\varepsilon = \frac{\dfrac{I_d + I_{b,n}}{I_d} + 5.535(10^{-6})\theta_z^{\,3}}{1 + 5.535(10^{-6})\theta_z^{\,3}} \tag{4.10}$$

$$\Delta = AM\,\frac{I_d}{I_{on}} \tag{4.11}$$

$$\begin{aligned} F_1 &= \max\left[0, \left(f_{11} + f_{12}\Delta + \frac{\pi\theta_z}{180} f_{13}\right)\right] \\ F_2 &= \left(f_{21} + f_{22}\Delta + \frac{\pi\theta_z}{180} f_{23}\right) \end{aligned} \tag{4.12}$$

4.3 COMPARATIVE STUDY OF RADIATION & OPTICAL MODELS

In the present study, a PV site located at the Florida State University campus in Tallahassee, Florida in the United States was selected. The electrical performance data for the site as well as measured meteorological data and module temperatures was obtained for the site for the complete year 2005 at 15 minutes intervals [67]. The site had two PV arrays installed each with a rated power output of 2970 Watts. The PV modules used in the arrays were Schott Solar SAPC 165 multi-crystalline modules arranged in two parallel strings of 9 modules each. The system was installed facing south at a slope of 30° which is approximately equal to the latitude of the site.

To perform the comparative analysis, one day was selected from each month and its performance was modeled at 15 minutes intervals. The selected day for each month was the mean day of the month [66]. The four parameter electrical model was used along with each of the four radiation & optical models to predict the electrical performance of the PV array for the selected twelve days. The effect of the selected radiation model on the prediction accuracy was analyzed using two statistical error techniques i.e. root mean square error and mean bias error given by Eq. (4.13) and Eq. (4.14) respectively.

$$RMSE = \frac{\frac{1}{n}\sqrt{\sum_{i=1}^{n}(y_i - x_i)^2}}{\frac{1}{n}\sum_{i=1}^{n}x_i} \tag{4.13}$$

$$MBE = \frac{\frac{1}{n}\sum_{i=1}^{n}(y_i - x_i)}{\frac{1}{n}\sum_{i=1}^{n}x_i} \tag{4.14}$$

The reference parameters (at standard test conditions (*STC*) of 1000 W/m^2 incident radiation and 25°C cell temperature) for a single SAPC-165 module were calculated and are given in Table 4.1.

Table 4.1: STC Reference Parameters for SAPC-165 PV Module

Parameter	**Value**
I_L	5.46 [A]
I_o	$2.45 \mathrm{x} 10^{-6}$ [A]
γ	115.9
R_s	0.49 [Ω]

4.3.1 Results and Discussion

In this section, first the results of three of the twelve days used in the analysis are presented. These three days represent the three types of cloud conditions namely clear, partially cloudy and overcast. Fig. 4.1 shows the *POA* irradiance and ambient temperature for the three days.

One way to analyze the prediction performance of any model is to plot modeled value against experimental value. Such a plot highlights the over- or under-prediction trends and the visualization of the accuracy of results. Fig. 4.2 shows the plots of modeled vs. experimentally determined power for isotropic, Hay & Davies, HDKR and Perez models for January 17. The plots show that the model that is most conservative is the Isotropic sky model while the Perez model has the highest over-prediction. Fig. 4.3 shows the modeled vs. experimentally determined power plot for March 16. March 16 was a very overcast day and Fig. 4.3 shows that all models heavily under predict the power output. The modeled vs. experimental power plots for May 15 are shown in Fig. 4.4. For May 15, which was a cloudy day, there is a sign of under-prediction from the isotropic model and the Hay & Davies model but the HDKR model and the Perez model show reasonably good results.

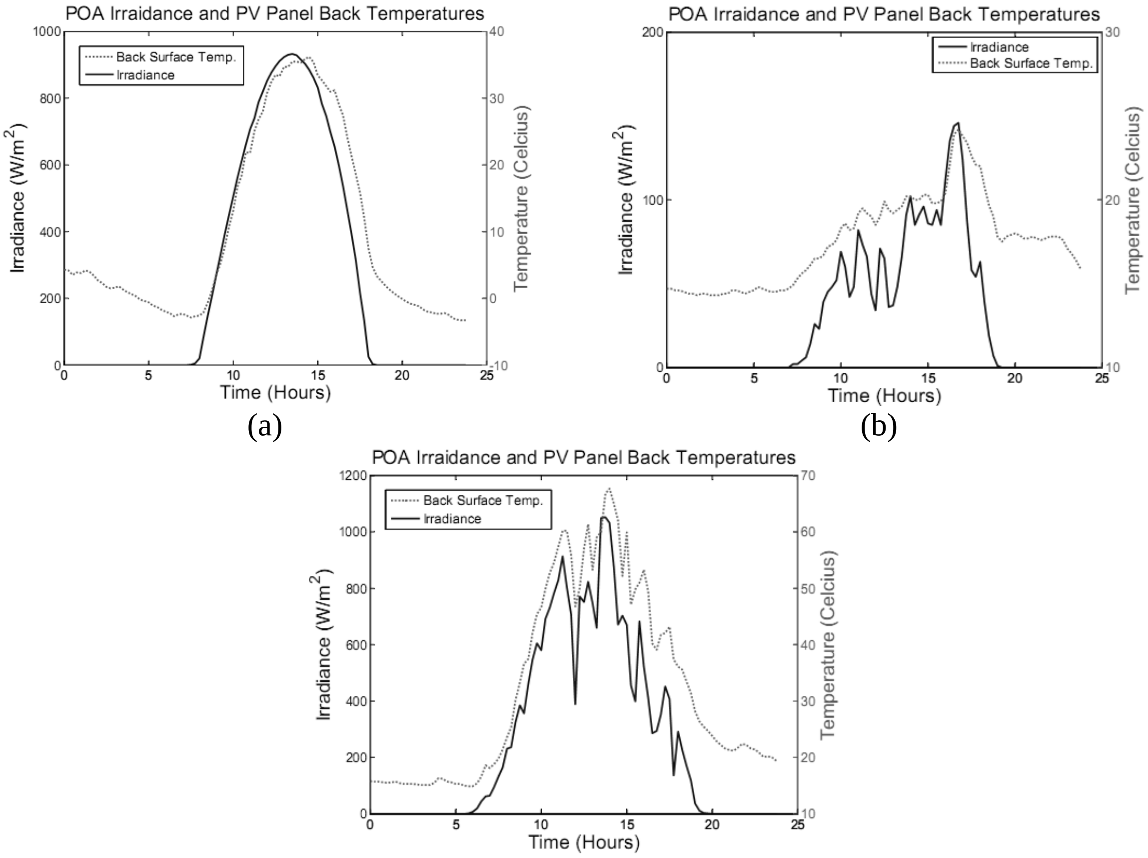

(a) (b)

(c)

Fig. 4.1. POA Irradiance and ambient temperature for (a) January 17 - Clear day, (b) March 16 - Overcast day and (c) May 15 - Cloudy day.

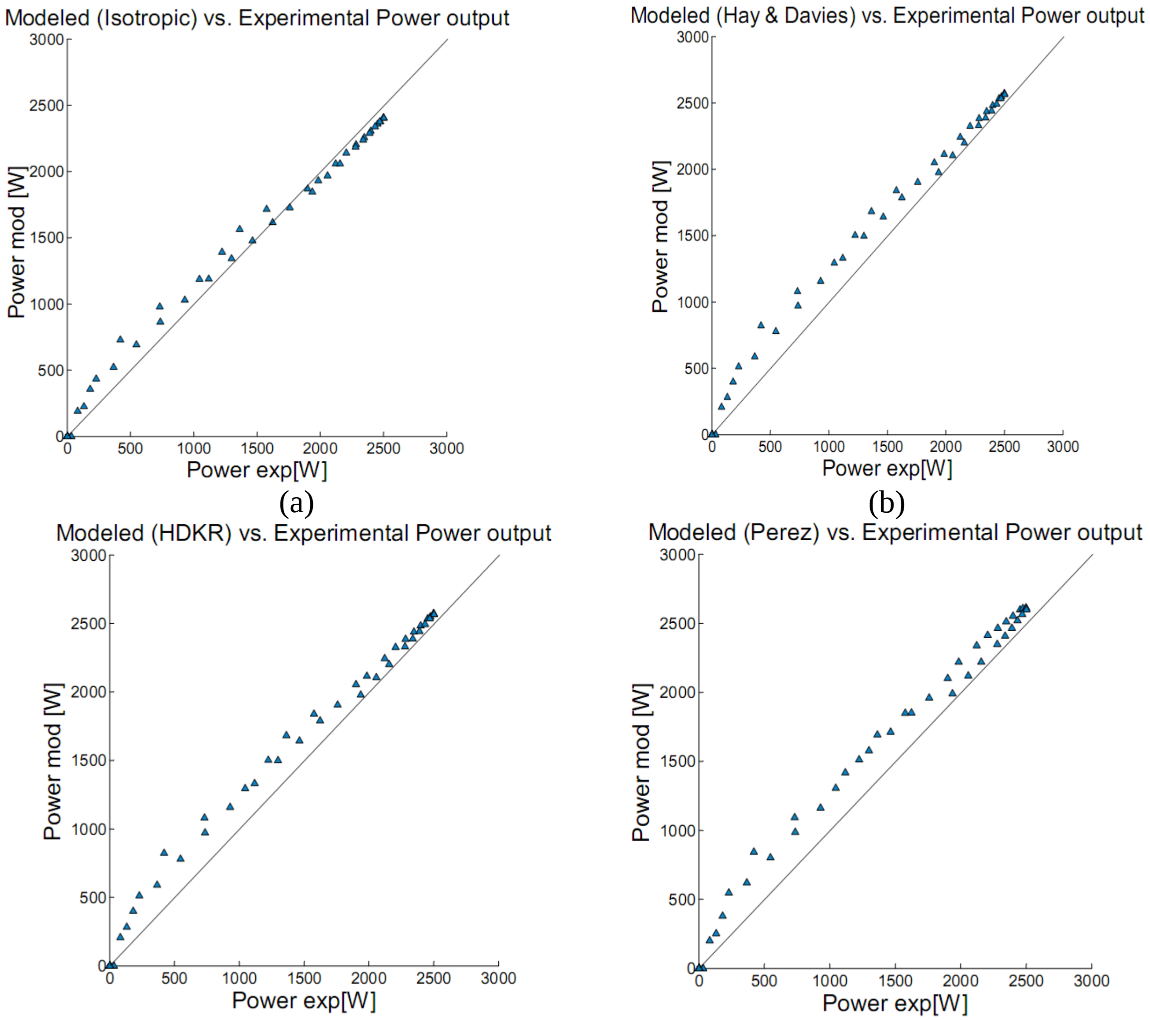

(a) (b) (c) (d)

Fig. 4.2. Modeled vs. Experimental Power - January 17 for (a) Isotropic model, (b) Hay & Davies model, (c) HDKR model and (d) Perez model.

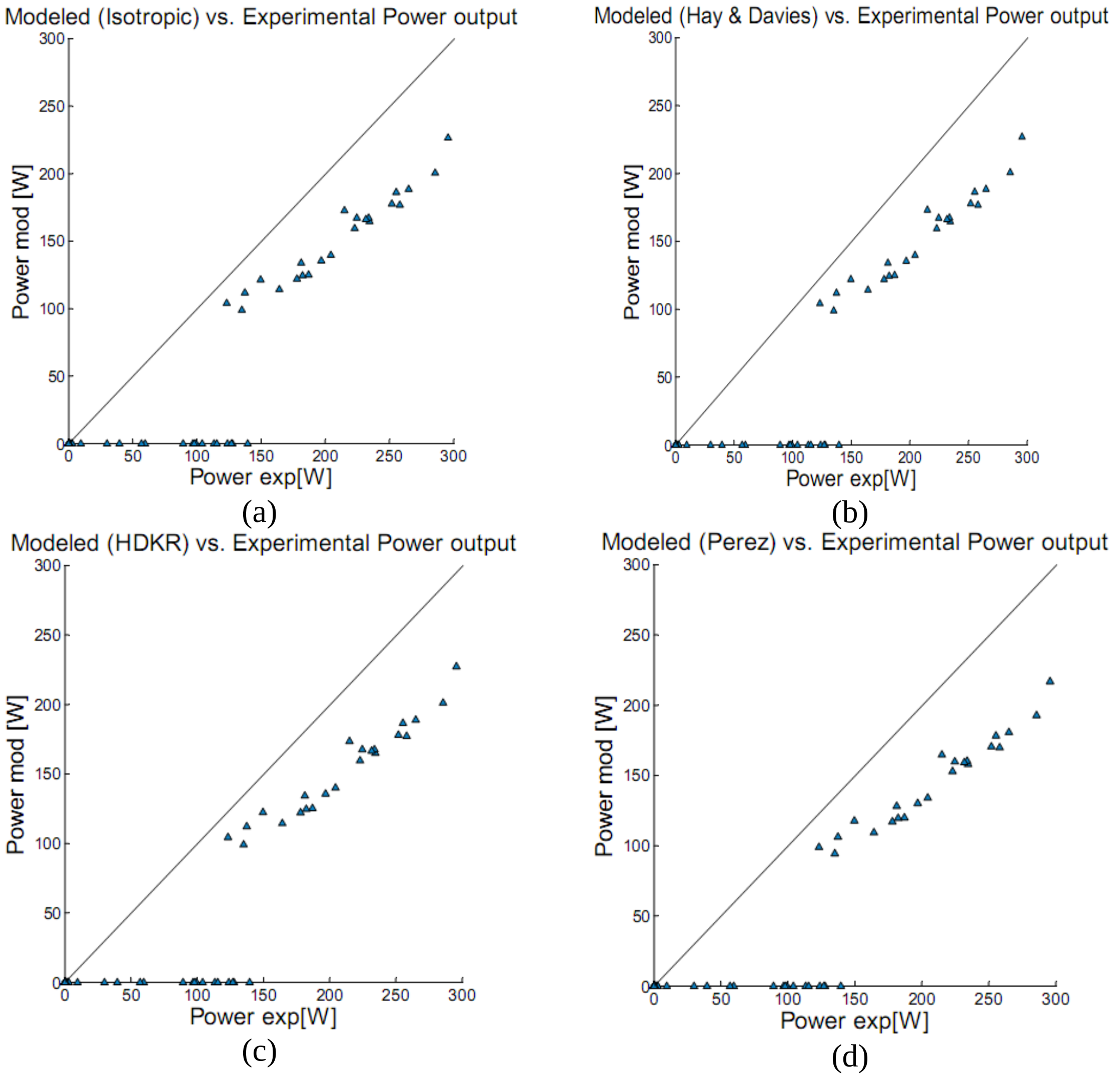

(a) (b)

(c) (d)

Fig. 4.3. Modeled vs. Experimental Power – March 16 for (a) Isotropic model, (b) Hay & Davies model, (c) HDKR model and (d) Perez model.

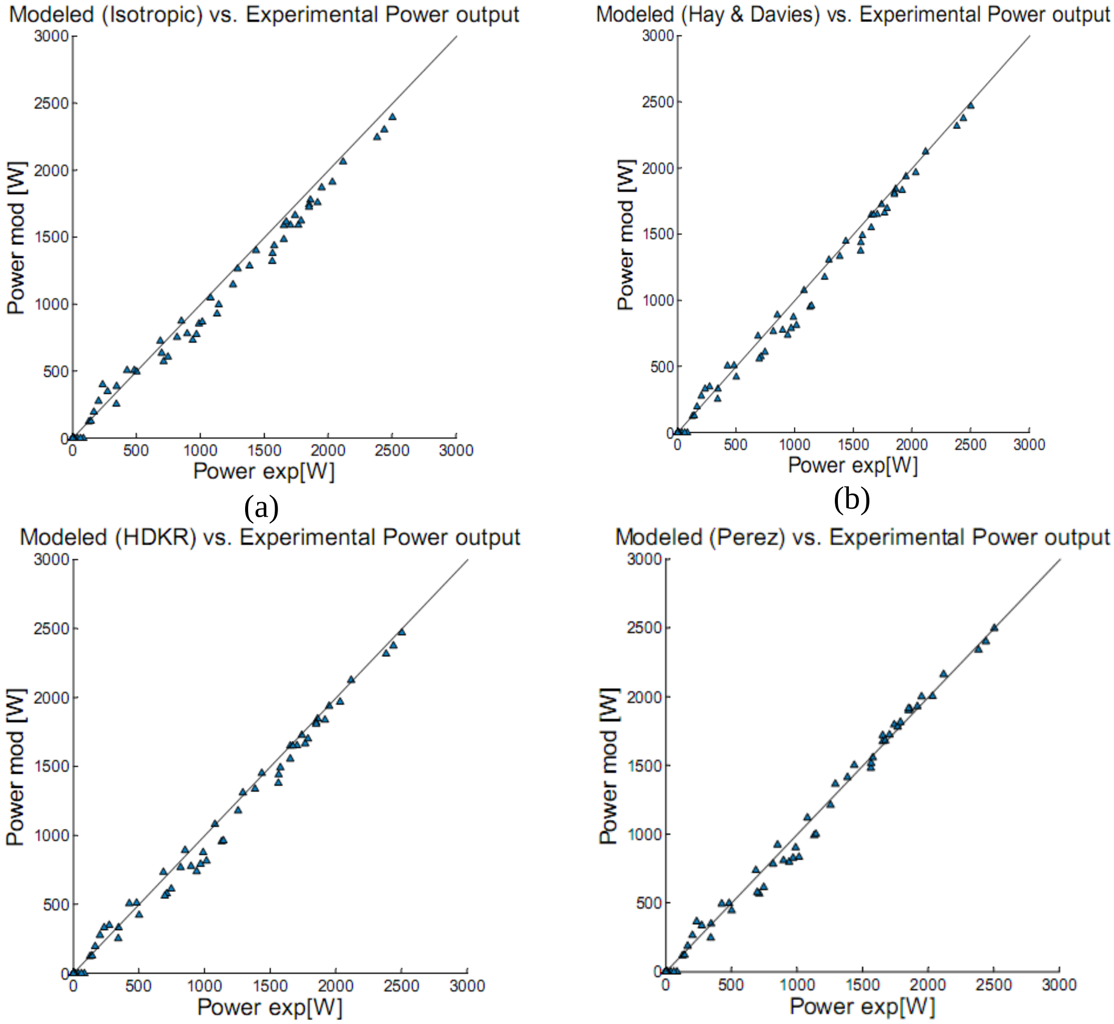

(a) (b)

(c) (d)

Fig. 4.4. Modeled vs. Experimental Power – May 15 for (a) Isotropic model, (b) Hay & Davies model, (c) HDKR model and (d) Perez model.

The overall modeling errors (*RMSE*) for all days are shown in Fig. 4.5. Fig. 4.5 shows that there is no clear difference in the prediction accuracy of the radiation models as each one of the four models show the least *RMSE* error for some days. Fig. 4.6 shows the mean bias errors (*MBE*) for all the modeled days. *MBEs* in Fig. 4.6 show that the most conservative of the models is the Isotropic model with an overall *MBE* equal to -6.5%. The *HDKR* model is the least biased with an overall *MBE* error of -1.46% while the overall *MBE* for Hay & Davies model is -1.65%. The Perez model, with an overall *MBE* equal to 1.9%, is the most over-predicting.

Since for most times the incident radiation on the PV panels is much below 1000 W/m^2, the electrical model was modified to include an additional set of reference parameters calculated at an absorbed solar radiation of 600 W/m^2 using the data available in IV curves in the module datasheet. These parameters are shown in Table 4.2 and were used whenever the absorbed radiation was below 600 W/m^2. This causes the overall MBEs of Isotropic sky model, Hay & Davies model, HDKR model and Perez model change to -7%, -2.57%, -2.39% and 0.5% respectively which shows a tendency to lower the prediction.

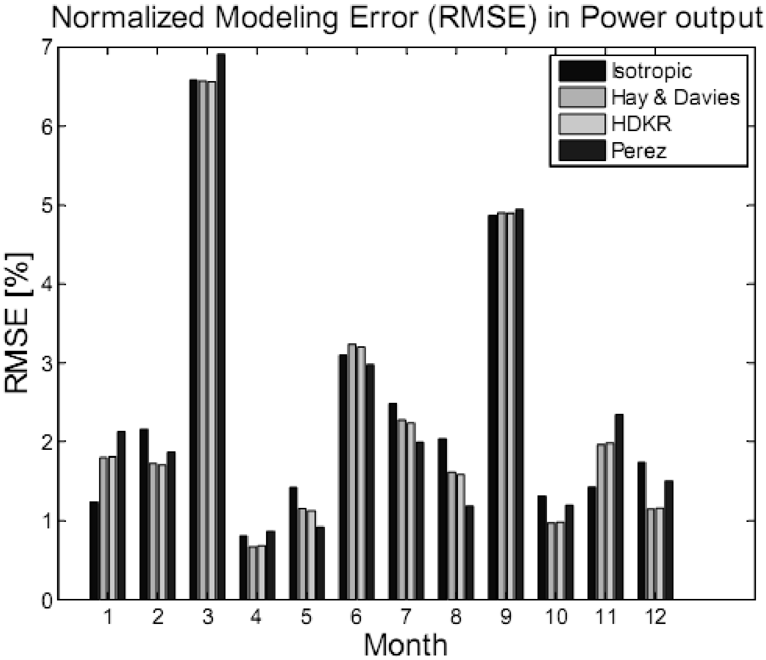

Fig. 4.5. Daily Modeling error (RMSE) in power prediction for all days.

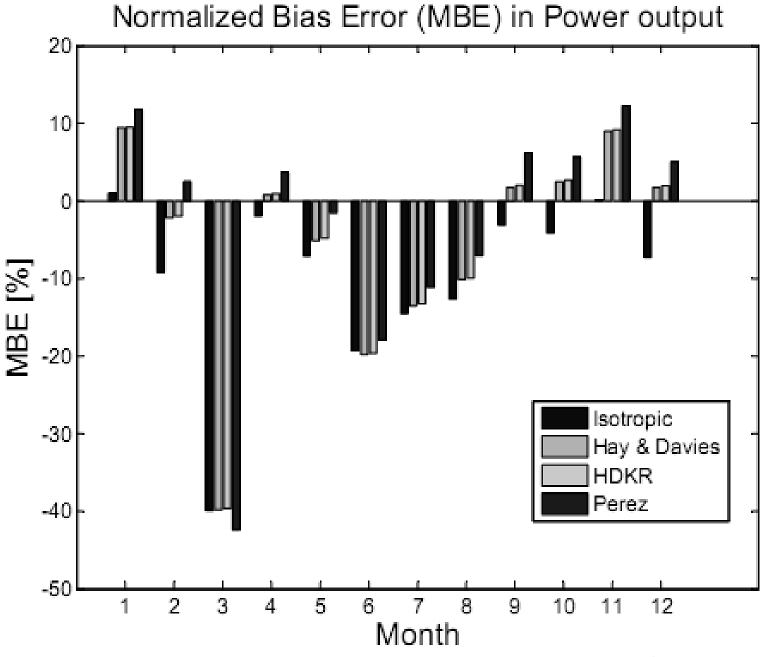

Fig. 4.6. Daily bias error (MBE) in power prediction for all days.

Table 4.2. Reference Parameters for SAPC-165 PV Module for 600 W/m^2 absorbed radiation

Parameter	**Value**
I_L	3.3375 [A]
I_o	3.167x10^{-6} [A]
γ	113.4
R_s	0.71 [Ω]

4.3.2 Conclusions

The following is a list of conclusions drawn from the study conducted.

- Isotropic radiation model is the most conservative while the Perez model has the highest over-prediction.
- The minimum bias is shown by the HDKR model and the maximum bias is shown by the Isotropic model.
- For system designing purposes, Isotropic model is the most suitable choice because of its conservative nature. For system studies, HDKR model is the most suitable choice because its prediction is the closest to actual value.
- The inclusion of an additional set of reference parameters in the electrical model tends to decrease the predicted values and hence results in more conservative predictions.

CHAPTER 5

THERMAL MODEL

Thermal models of PV modules are used to calculate the temperature field in the PV module at given environmental and operating conditions. A substantial body of research work on the development of thermal models either with cooling [38,44,47,48,50] or without cooling [2,4,5,34] has appeared in the literature. Most of the reported research effort deals with one-dimensional analytical thermal model for PV panels with temperature variation along the thickness only. Although simple 1D models are sufficiently accurate for long term performance predictions, more complex 2D and 3D models are needed to capture temperature gradient effect in PV/T collectors. Only such a model can handle complex heat exchanger flow patterns and design optimization tasks [50]. In the present work, three dimensional numerical models were developed to predict the thermal behavior of PV panels with and without cooling.

5.1 THERMAL MODELING OF PV MODULES

The temperature distribution in PV panels depends on the PV module materials, PV cell type, the panel configuration, the electrical load attached to the PV system, the prevailing environmental conditions and in case of cooling, the characteristics of the heat exchanger.

For a PV panel, the various modes of energy transfer in the PV panel are shown in Fig. 5.1. The panel gains energy by absorbing incoming solar radiation while energy is lost from it by convection and radiation to the environment, by energy transfer to the working fluid in the heat exchanger and in the form of electrical energy delivered to the electrical load. In case of PV panel without cooling, the energy transfer to the heat exchanger through the PV panel back surface is replaced by convection and radiation losses to the environment.

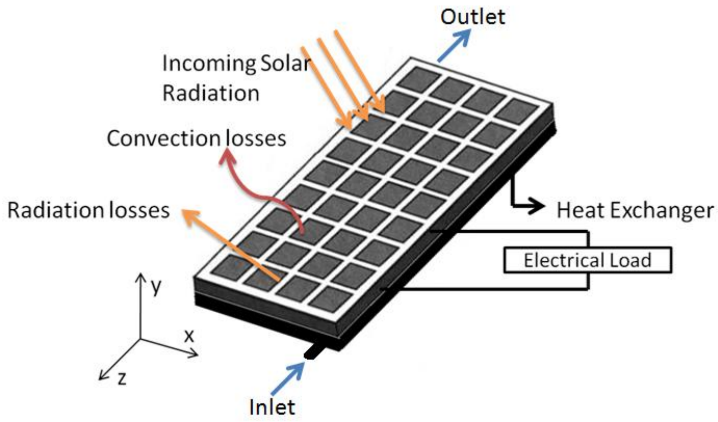

Fig. 5.1. Modes of energy transfer in a PV panel.

5.1.1 Governing Equations

The heat transfer in cooled PV panels involves a fluid and multiple solid domains. The fluid domain covers the working fluid inside the heat exchanger. There is a separate solid domain for each material layer (front cover, encapsulent, PV cells and back sheet) in the PV panel and for the heat exchanger body. For any solid domain, the energy equation can be derived from the 1st law of thermodynamics. For solids, heat flow is by conduction only. Therefore, for a one-dimensional element of length *Δx,* the energy equation is,

$$\rho C_p A\Delta x \frac{\Delta T}{\Delta t} = -kA\frac{\Delta T}{\Delta x}\bigg|_x - \left(-kA\frac{\Delta T}{\Delta x}\bigg|_{x+\Delta x}\right) + \dot{Q}_{gen}A\Delta x$$

By dividing by *A* and *Δx* and taking limits $\Delta x \to 0$ and $\Delta t \to 0$, we get,

$$\rho C_p \frac{\partial T}{\partial t} = \frac{\partial}{\partial x}\left(k\frac{\partial T}{\partial x}\right) + \dot{Q}_{gen}$$

For the three-dimensional case considered, equation (5.1) is the energy equation for the solid domains and equation (5.2) is the energy equation for the fluid domain [68] where ρ is the density, C_p is the specific heat capacity, $T(x,y,z)$ is the temperature, t is the time, k is the thermal conductivity, $\boldsymbol{q}$ is the heat transferred by conduction, Q is the internal heat generation, $\boldsymbol{u}$ is the fluid velocity and Q_{vh} is the viscous dissipation.

$$\rho_i C_{pi} \frac{\partial T_i(x,y,z)}{\partial t} = \nabla.(\mathbf{q}_i) + Q_i \ , \ i=1,2,\ldots,n \tag{5.1}$$

$$\rho C_p \frac{\partial T(x,y,z)}{\partial t} + \rho C_p \mathbf{u}.\nabla T(x,y,z) = \nabla.(\mathbf{q}) + Q_{vh} \tag{5.2}$$

where,

$$\mathbf{q} = k\nabla T \tag{5.3}$$

The momentum and continuity equations governing the fluid flow inside the heat exchanger are given by equations (5.4) and (5.5) where p is the pressure, μ is the viscosity, μ_T is the turbulent viscosity and k is the turbulent kinetic energy. The turbulence model used is the k-ε model given by equations (5.6)-(5.9) [69].

$$\rho\frac{\partial\mathbf{u}}{\partial t}+\rho(\mathbf{u}.\nabla)\mathbf{u}=\nabla.\left[-p\mathbf{I}+(\mu+\mu_T)\left(\nabla\mathbf{u}+\nabla\mathbf{u}^T\right)-\frac{2}{3}\rho k\mathbf{I}\right] \tag{5.4}$$

$$\frac{d\rho}{dt}+\nabla.\rho\mathbf{u}=0 \tag{5.5}$$

$$\rho\frac{\partial k}{\partial t}+\rho(\mathbf{u}.\nabla)k=\nabla.\left[\left(\mu+\frac{\mu_T}{\sigma_k}\right)\nabla k\right]+P_k-\rho\varepsilon \tag{5.6}$$

$$\rho\frac{\partial\varepsilon}{\partial t}+\rho(\mathbf{u}.\nabla)\varepsilon=\nabla.\left[\left(\mu+\frac{\mu_T}{\sigma_e}\right)\nabla\varepsilon\right]+C_{e1}\frac{\varepsilon}{k}P_k-C_{e2}\rho\frac{\varepsilon^2}{k} \tag{5.7}$$

$$\mu_T=\rho C_\mu\frac{k^2}{\varepsilon} \tag{5.8}$$

$$P_k=\mu_T\left[\nabla\mathbf{u}:\left(\nabla\mathbf{u}+(\nabla\mathbf{u})^T\right)\right] \tag{5.9}$$

where P_k is production term and ε is the turbulent dissipation rate. The values of the model constants are C_μ=0.09, $C_{\varepsilon 1}$=1.44, $C_{\varepsilon 2}$=1.92, σ_k=1.0 and σ_ε=1.3 [69].

5.1.2 Thermal Load and Boundary Conditions

The incoming solar radiation is used to calculate the absorbed solar radiation using the HDKR radiation and optical model [10,66] defined by Eq. (4.6). A portion of the absorbed solar radiation is converted to electrical energy while the remaining energy raises the temperature of the PV panel. The absorbed solar radiation is applied to the heat transfer equation of the PV cell layer as an internal heat generation, Q, which is calculated using equation (5.10) where η_{pv} is the electrical efficiency of the PV panel, A_{panel} is the front area of the PV panel and the $V_{pv\,cell}$ is the volume of the PV cells in the panel.

$$Q = \frac{(1-\eta_{pv})\ \mathrm{x}\ S\ \mathrm{x}\ A_{panel}}{V_{pv\,cell}} \tag{5.10}$$

Convection boundary conditions were applied to the PV panel top and bottom surfaces for the model without cooling and to the top surface only for the model with cooling. After a study of several correlations for calculating the heat transfer coefficient for PV panels, Notton et al. (2005) suggested using equation (5.11) for calculating the heat loss coefficient where h is the heat loss coefficient and WS is the wind speed.

$$h = 11.4 + 5.7(WS) \tag{5.11}$$

The corresponding boundary conditions applied to the heat transfer equations of top and bottom layers of the PV panel is given by equation (5.12) where **n** is the surface normal and T_{amb} and T_s are the ambient and surface temperatures.

$$-\mathbf{n}.\mathbf{q} = h\left(T_{amb} - T_s\right) \tag{5.12}$$

For the fluid domain, the inlet boundary conditions were defined by the inlet water temperature, $T_{f,in}$ and a uniform velocity, $V_{f,in}$ as expressed by equations (5.13) and (5.14).

$$T = T_{f,in} \tag{5.13}$$

$$\mathbf{u} = -\mathbf{n}V_{f,in} \tag{5.14}$$

The outlet condition is set to zero gauge pressure and no slip condition is applied to all internal surfaces of the heat exchanger. A perfect contact is assumed between all the layers in the PV panel.

5.1.3 Implementation of the Thermal Model for PV Panel without Cooling

The implementation of the thermal model without cooling was done in ANSYS Mechanical finite element code using a four-node thermal shell element, SHELL131, which is a 3-D layered shell element having in-plane and through-thickness thermal conduction capability. The use of layered elements allows all the material layers in a PV panel to be included in the model without increasing computational costs. The geometry of the model is shown in Fig. 5.2. Though, the geometry of the PV module is 2-dimensional, the temperature variation through thickness is also considered in the model.

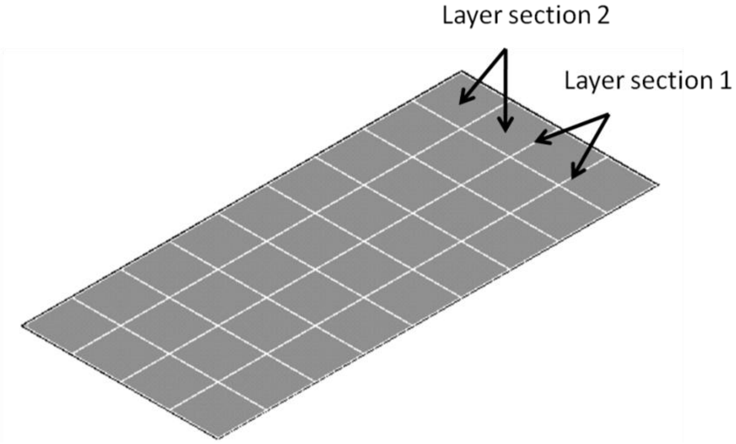

Fig. 5.2. Geometry of the model for PV panel without cooling

The various material layers in a standard PV module and the two layer sections are shown in Fig. 5.3. The material properties used in the model are given in Table 5.1.

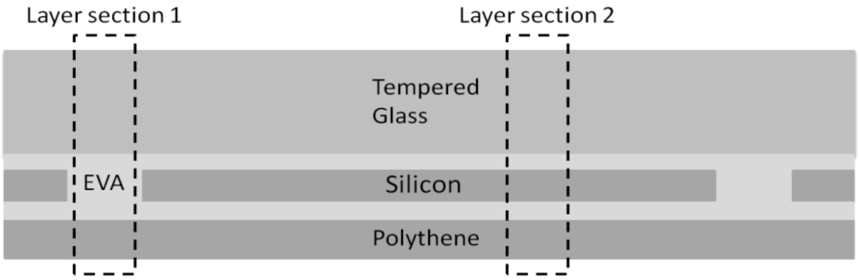

Fig. 5.3. Layers in PV module.

Table 5.1. Material properties for PV Panel materials.

Material	Layer	Thermal Conductivity (W/m.K)	Specific Heat Capacity (J/kg.K)	Density (kg/m^3)
Silicon	Solar cell	130	677	2330
Tempered Glass	Top cover	2	500	2450
Polyester	Bottom cover	0.15	1250	1200
Ethyl Vinyl Acetate	Encapsulant	0.311	2090	950

5.1.4 Implementation of the Thermal Model for PV Panel with Cooling

The thermal model with cooling was implemented in ANSYS CFX environment as a computation fluid dynamics (CFD) model of the PV panel with a heat exchanger attached to its back. The working fluid in the heat exchanger was assumed to be water. The geometric model is 3-dimensional and was prepared and meshed in ANSYS Mechanical. The geometry of the model and the flow channels for water in the heat exchanger are shown in Fig. 5.4. The heat exchanger design selected for this study was the parallel channel type heat exchanger. The model consists of four solid domains for the PV panel: front cover, back sheet, encapsulent and the PV cells and two domains for the heat exchanger: a solid domain for the heat exchanger body and a fluid domain for the water inside the heat exchanger.

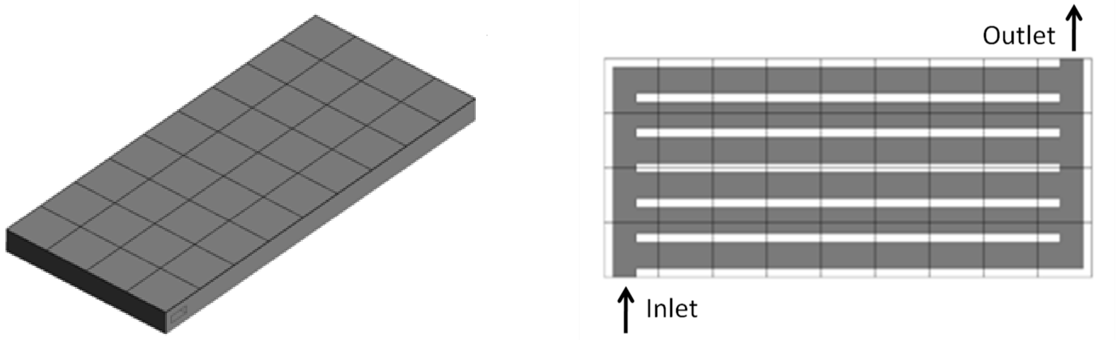

Fig. 5.4. Geometry of model with cooling.

The material for heat exchanger is assumed to be Aluminum and its material properties are given in Table 5.2.

Table 5.2. Material properties for heat exchanger body

Material	Thermal Conductivity (W/m.K)	Specific Heat Capacity (J/kg.K)	Density (kg/m^3)
Aluminum	237	903	2702

5.2 MODEL VALIDATION

To validate the developed thermal model, three types of validations were carried out. For the thermal model without cooling, two validations were done, one against experimentally measured data and second against the normal operating conditions temperature (*NOCT*) reported in the module datasheet. The model for PV panel with cooling was validated against a simplified one dimensional model. The details of the validations are presented in the following sections.

5.2.1 Validation of Thermal Model without Cooling using Experimental Data

The thermal model for PV panel without cooling was validated using experimentally measured data for a 5940 Watts PV site using Schott Solar SAPC-165 multi-crystalline silicon PV panel. The site is located in Tallahassee, Florida, USA. The data recorded at the site included plane-of-array incident solar radiation, ambient temperature, PV panel back-surface temperature and electrical current, voltage and power. The meteorological data for the PV site for one day (May 15, 2005) was taken from the PV performance database maintained by *Florida Solar Energy Center* and is shown in Fig. 5.5 [67]. The wind speed data which was not measured at the site was taken from the measurements made at Tallahassee regional airport [70]. The wind speed data is shown in Fig. 5.6. The developed model was used to calculate the transient thermal response of the PV panel for the environmental conditions for the selected day and the module back surface temperature predicted by the current model was compared to the experimentally measured values. The comparison is shown in Fig. 5.7. The root mean square error in the model prediction of panel back surface temperature was 3.19°C while the maximum error was -7.64°C.

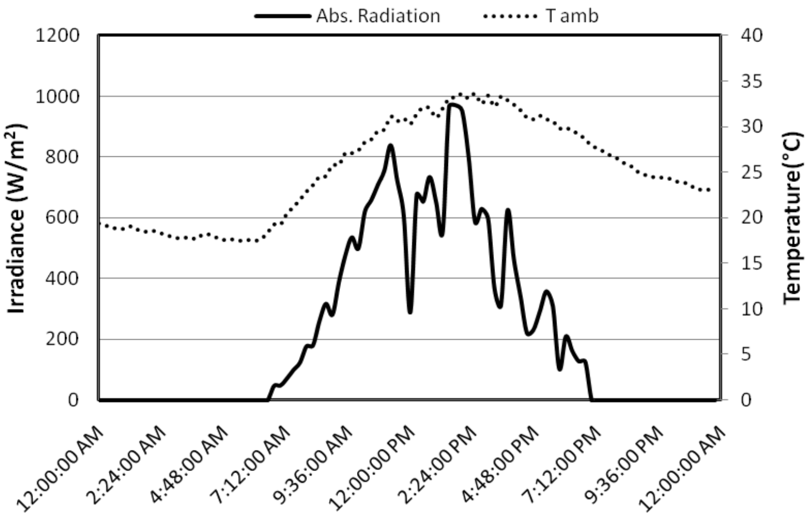

Fig. 5.5. Meteorological and environmental data for the PV Site (Florida Solar Energy Center PV performance database)

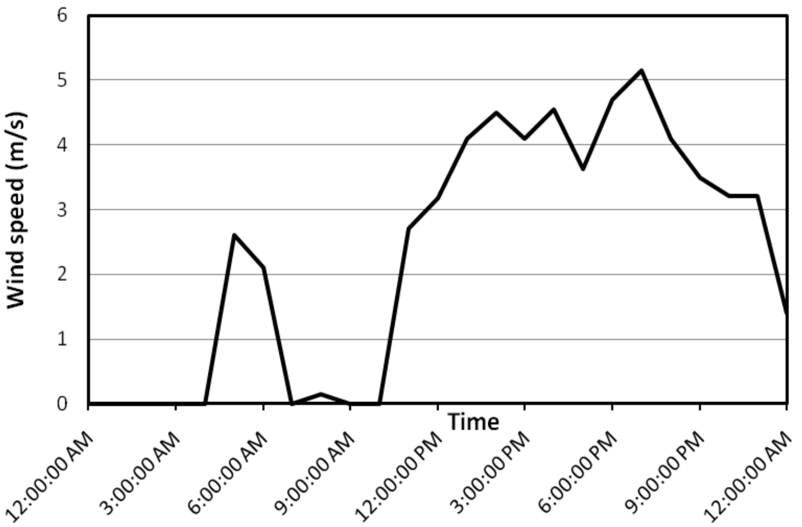

Fig. 5.6. Wind speed data for Tallahassee, Florida on May 15, 2005 (Wolfram Mathematica Weather Data)

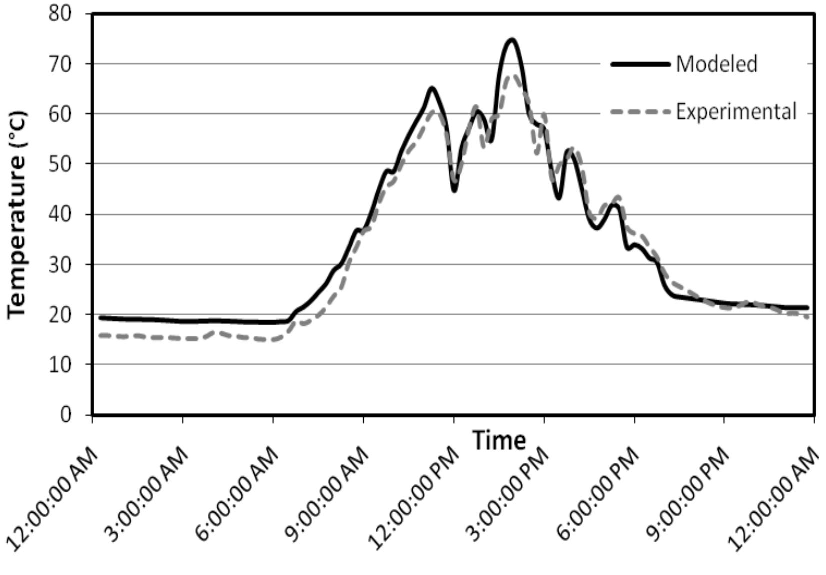

Fig. 5.7. Model validation for thermal model without cooling using experimental data

5.2.2 Validation of Thermal Model without Cooling using Manufacturer Data

Using the thermal model for PV panels without cooling, the normal operating conditions temperature (*NOCT*) of AstroPower AP-110 mono crystalline silicon PV module was predicted and compared to the value provided in the module datasheet. The inputs to the model were an incident solar radiation of 800 W/m2, an ambient temperature of 20°C, and a wind speed of 1m/s on the front surface. The NOCT reported in the datasheet of the module is 45°C. The predicted value from the model, shown in Fig. 5.8, is 44.2°C (317.2 K). This represents a 1.78% error in PV cell temperature prediction.

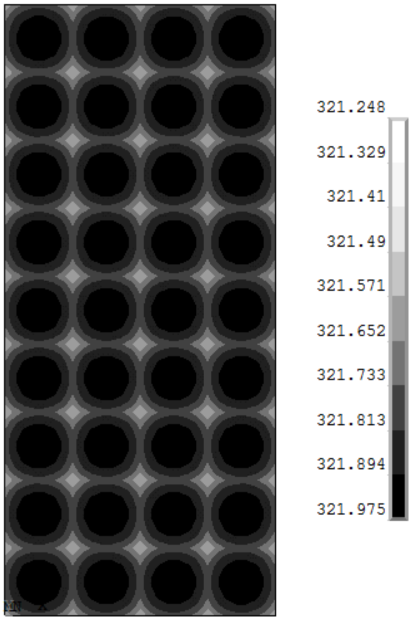

Fig. 5.8. Model validation for thermal model without cooling using manufacturer data

5.2.3 Validation of Thermal Model with Cooling using Analytical Model

To validate the thermal model with cooling, the results of the model for the simple case of parallel channel heat exchanger attached to an AstroPower AP-110 module were compared with the analytical model for the parallel channel heat exchanger PV/T collector presented by Sarhaddi et al. [45]. Temperatures of the fluid outlet and PV cells were compared at various inlet velocities. The results of the comparison are shown in Table 5.3. The root mean square errors in the prediction of PV cells and outlet fluid temperatures were 1.61°C and 1.94°C respectively.

Table 5.3. Model validation for thermal model with cooling

Inlet Velocity (m/s)	Cell Temperature (°C)		Outlet Fluid Temperature(°C)	
	Current Model	using Sarhaddi et al. (2010)	Current Model	using Sarhaddi et al. (2010)
0.1	29.3	29.1	25.02	25.6
0.05	31.05	31.5	26.44	26.1
0.01	37.05	39.8	29.6	26.3

5.3 PARAMETRIC STUDY - PV PERFORMANCE UNDER VARYING ATMOSPHERIC AND OPERATING CONDITIONS

Using the developed and validated models, studies were conducted with an objective to study the effect and usefulness of cooling on the performance of the PV panel under different atmospheric and operating conditions. The effect of atmospheric factors such as ambient temperature and solar irradiance on the performance (T_{cell}, $T_{water,out}$, η_{pv}, *Electric*

Power) of PV panels with and without cooling were studied. Additionally, the effect of heat exchanger inlet conditions and thermal contact resistance between the PV panel and heat exchanger on the performance of cooled PV panels was also analyzed. In all of the studies conducted, a standard case was studied by varying only a single parameter. The PV module selected for the study was AstroPower AP-110 module. The electrical model used in the study was the Four Parameters model. The electrical model reference parameters for the selected module are given in Table 5.4.

Table 5.4. Electrical model reference parameters for the selected PV module.

Parameter	**Value**
$I_{L,ref}$	7.5 [A]
$I_{o,ref}$	3.0176e-6 [A]
γ_{ref}	54.7192
$R_{s,ref}$	0.1545 [Ω]

The operating and environmental conditions considered for the standard case were 800 W/m^2 absorbed radiation, 25°C ambient temperature and for cooling, inlet water velocity and temperature equal to 0.05 m/s and 25°C. A perfect contact was assumed between the PV panel and the heat exchanger.

Fig. 5.9 and Fig. 5.10 show the temperature distribution in PV cells for the panels without cooling and with cooling respectively for the standard case. Fig. 5.11 shows the temperature distribution in water in the heat exchanger and Fig. 5.12 shows the flow pattern of water inside the heat exchanger. It can be seen that in the panel without cooling, no appreciable temperature gradient exists while in the panel with cooling, there is almost a 4°C temperature difference in PV cells across the panel. This difference is due to the non-uniform water flow in the heat exchanger as is shown in Fig. 5.12. Such temperature profiles cannot be determined by simple 1-D models such as the one presented by Sarhaddi et al. (2010).

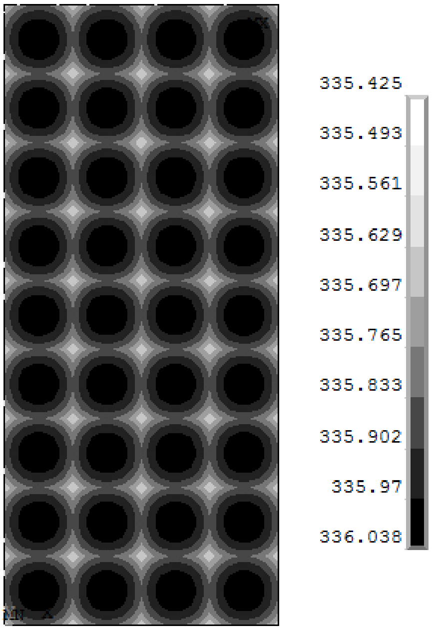

Fig. 5.9. Temperature distribution in PV cells for panel without cooling.

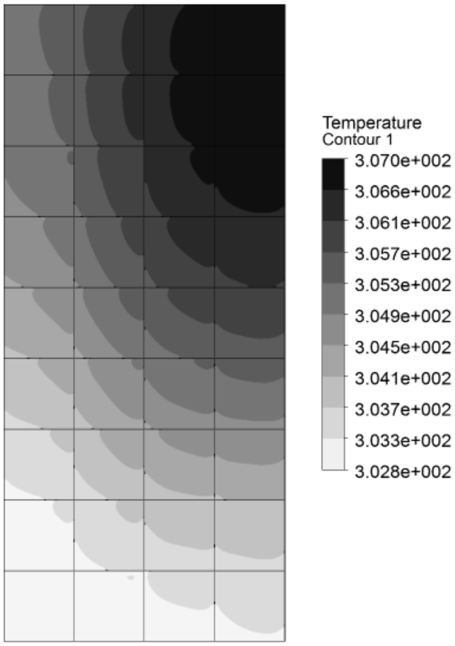

Fig. 5.10. Temperature distribution in PV cells for panel with cooling.

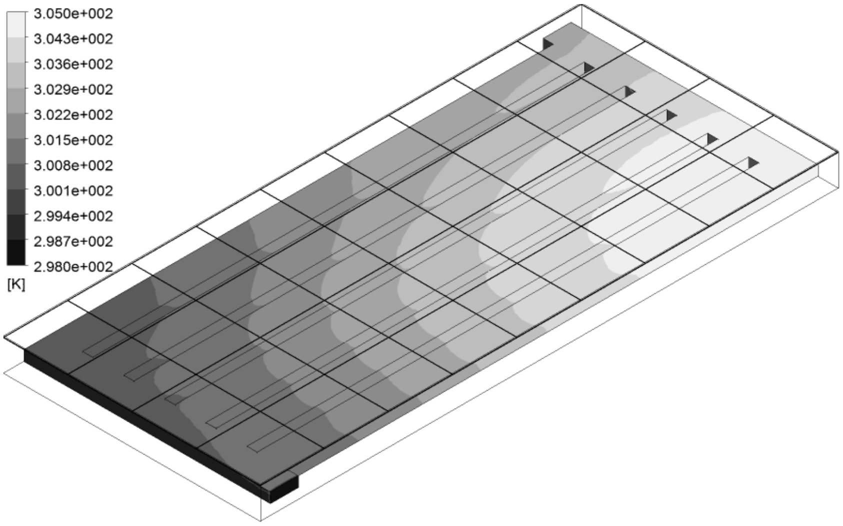

Fig. 5.11. Temperature distribution in water inside the heat exchanger.

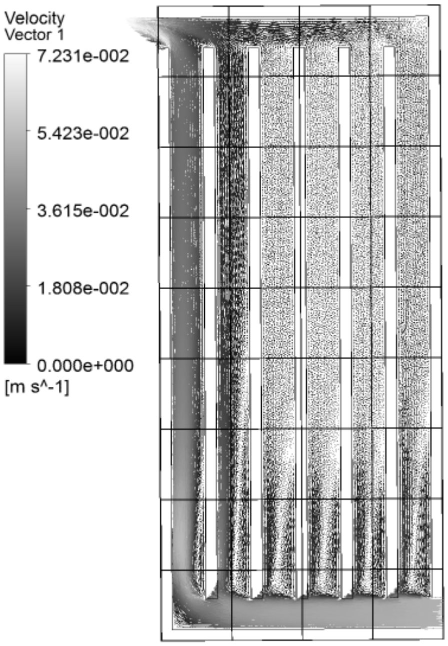

Fig. 5.12. Flow Pattern of water inside the heat exchanger.

5.3.1 Effect of Absorbed Solar Radiation on Panel Performance

Incident solar radiation is one of the most important environmental parameters that determine the performance of PV panels. In order to study the effect of cooling on the performance of PV panels under different amounts of solar radiation, the developed models for PV panels with cooling and without cooling were used to calculate the PV cells and water outlet temperatures, electrical efficiency and electrical power output of the panel for different amounts of absorbed radiation. The selected range of radiation was taken from 400 W/m^2 to 3000 W/m^2 to include radiation levels for PV panels with and without concentration. The results are shown in Fig. 5.13. The average PV cell temperature for the PV panel without cooling ranges from 44 to 168°C whereas for the panel with cooling, the range is from 28°C to 50°C. It is important to note here that in real-life situations, an upper limit of 168°C is unrealistic as such high temperature can damage the PV panel. The outlet water temperature ranges from 26°C to 31°C which is not very high. Due to the very high cell temperatures at high solar irradiances, the electrical efficiency of the PV panel without cooling drops from 10% at 400 W/m^2 to 4% at 3000 W/m^2. Due to this efficiency drop, the electrical power output of the panel shows very little increase with increase in absorbed radiation. In fact, the electrical output drops from 128W to 124W when the absorbed radiation increases from 2000W/m^2 to 3000W/m^2 due to a significant drop in efficiency. On the other hand, the cooled PV panel shows only about 1% drop in efficiency from 10.5% to 9.5% for the selected absorbed solar radiation range. The results presented in Fig. 5.13 show the importance of cooling when concentration is being used on PV panels. The fact that the panel without cooling reaches very high temperatures explains why some form of additional heat dissipation mechanism (cooling, fins, etc) is usually added to panels under solar concentration.

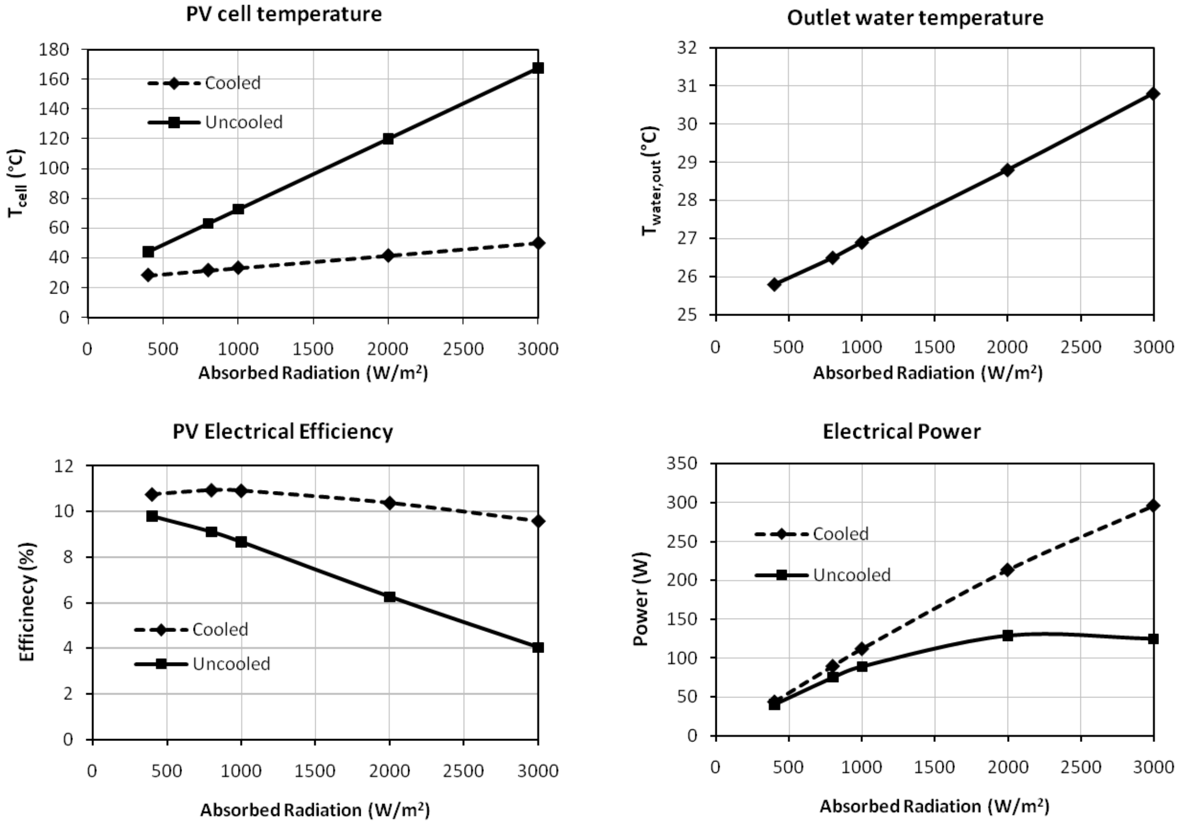

Fig. 5.13. PV panel performance variation with absorbed radiation. (T_{amb}=25°C, $V_{f,in}$=0.05 m/s, $T_{f,in}$=25°C)

5.3.2 Effect of Ambient Temperature on Panel Performance

Ambient temperature is another very important environmental factor. In order to study the effect of cooling on PV panel's performance working in different ambient temperatures, the developed models were used to calculate the PV cells and water outlet temperatures, electrical efficiency and electrical power output of the PV panel with and without cooling for ambient temperatures ranging from 0°C to 50°C. This range of ambient temperatures covers PV panels working in cold winter conditions to very hot summer conditions. The results are shown in Fig. 5.14. The cooled PV panel shows no significant performance variation for the entire ambient temperature range. On the other hand, for the PV panel without cooling, the average PV cell temperature increases from 38°C to 88°C as ambient temperature increases from 0°C to 50°C, the electrical efficiency drops from 11% to 8%, the electrical power output decreases from 86W to 63W. This represents a 27% decrease in electrical power output for the PV panel without cooling from the coldest to the hottest environment considered.

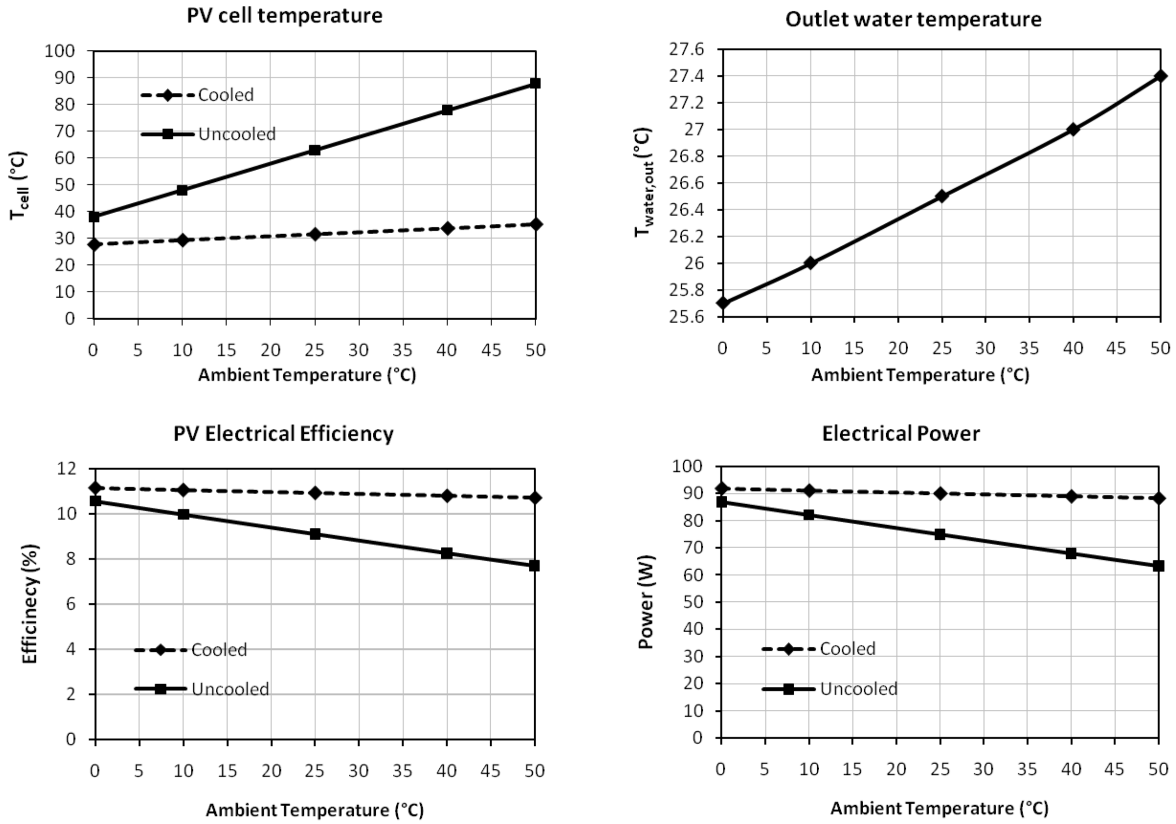

Fig. 5.14. PV panel performance variation with ambient temperature. (S=800 W/m^2, $V_{f,in}$=0.5 m/s, $T_{f,in}$=25°C)

5.3.3 Effect of Heat Exchanger Inlet Conditions

The operating parameters of the heat exchanger also affect the performance of the PV panel. In this study, the effect on performance of heat exchanger parameters, inlet velocity and inlet temperature, were studied. Fig. 5.15 shows the results for inlet velocity variation. The range of inlet velocities was taken from 0.01m/s to 0.1m/s. For this range, the average PV cell temperature decreases from 38°C to 30°C and the outlet water temperature drops from 30°C to 26°C. The absolute increase in electrical efficiency is only 0.4% which for the selected PV panel means 4W more electrical power.

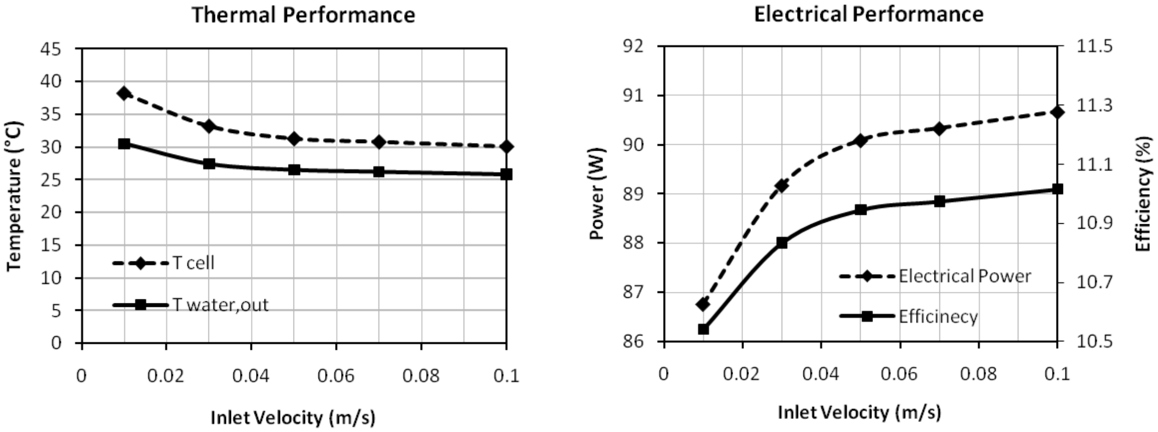

Fig. 5.15. PV panel performance variation with heat exchanger inlet velocity. (S=800 W/m^2, T_{amb}=25°C, $T_{f,in}$=25°C)

Fig. 5.16 shows the variation in the PV panel performance with inlet temperature variation. The range selected for inlet water temperature variation was 5-45°C. Such high inlet temperatures can also result when the heat exchangers of multiple PV panels are connected in series. For the selected range of inlet temperatures, the average PV cell temperatures increase from 14°C to 49°C, the efficiency drops from 12% to 10% and this causes the electrical power output of the PV panel to drop by almost 20W.

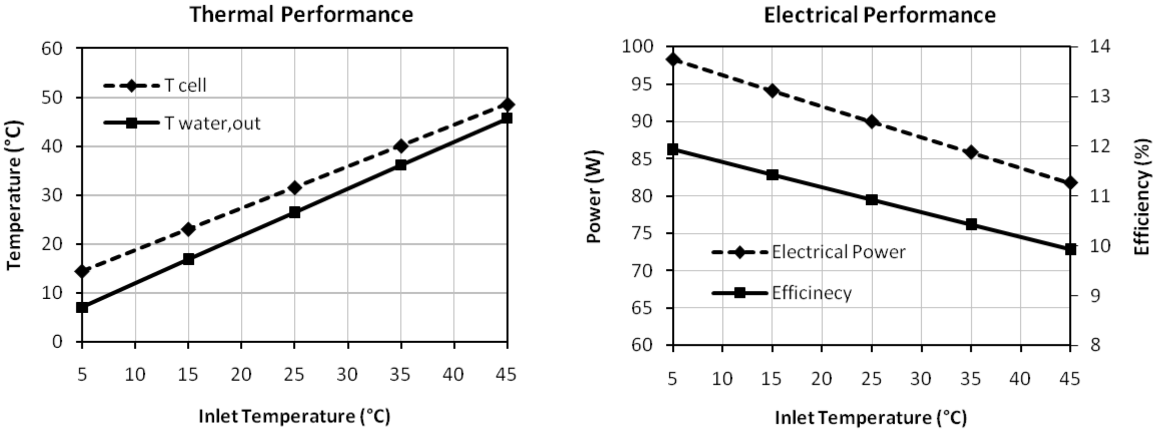

Fig. 5.16. PV panel performance variation with heat exchanger inlet temperature. (S=800 W/m^2, T_{amb}=25°C, $V_{f,in}$=0.5 m/s)

5.3.4 Effect of Thermal Contact Resistance

Inefficient thermal contact resistance between the PV panel and the heat exchanger can also lead to degradation of PV panel performance. The range of thermal contact resistance used in this study is 0.005-0.05 °C.m^2/W and was taken from the work of Bahrami et al. [71]. Fig. 5.17 shows the results of the study. The difference between the case of ideal contact and the case of maximum contact resistance considered, the increase in PV cell temperature is 15°C but the absolute drop in efficiency is around 1%. This means that about 9% of electrical power is lost due to the contact resistance.

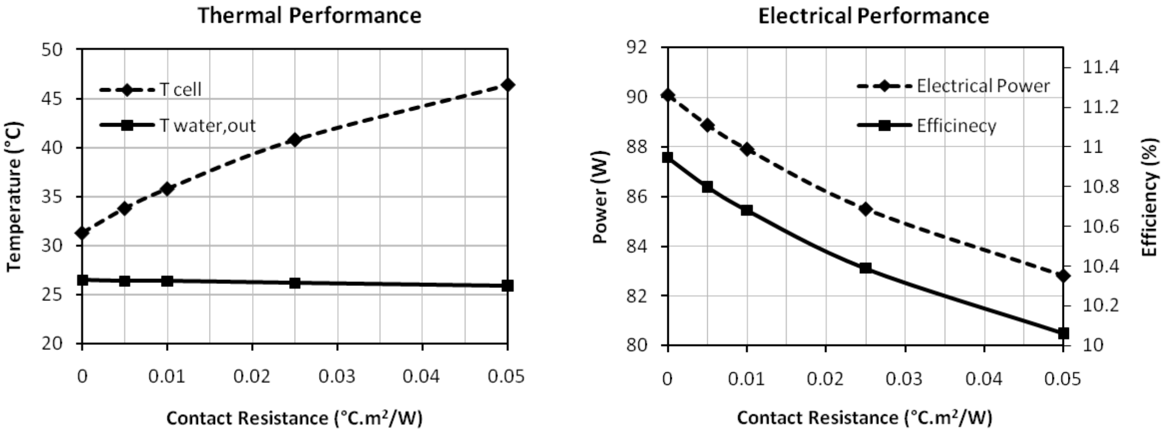

Fig. 5.17. PV panel performance variation with change in thermal contact resistance.

(S=800 W/m^2, T_{amb}=25°C, $V_{f,in}$=0.5 m/s, $T_{f,in}$=25°C)

5.3.5 Conclusion

A three dimensional numerical model to predict thermal and electrical performance of the PV panel for given environmental and operating conditions is presented and validated in this paper. From the various studies conducted using this model, the following conclusions are drawn:

- Within the absorbed radiation range of 400-3000 W/m^2 at an ambient temperature of 25°C, PV panel with cooling maintains its efficiency (9.5-10.5%) with almost linearly increasing electrical power from 50W to 300W. Whereas, for the same range, efficiency reduces from 10% to 4% for panel without any cooling.
- For an absorbed radiation of 800W/m^2, the efficiency and electrical power of PV panel with cooling almost remains constant at 11% and 90W, respectively, for the ambient temperature variation from 0°C to 50°C. For PV panel without cooling, the electrical power output decreases from 86W to 63W under the same temperature range.
- Thermal contact resistance between PV panel and heat exchanger can result in significant power loss due to higher PV cell temperatures. The decrease in electrical power output of the panel with contact resistance equal of 0.05°C.m^2/W is around 9% with respect to panel having no thermal resistance.
- The effect of cooling will be more pronounced in hot environments like Saudi Arabia having high solar irradiance and ambient temperature.

CHAPTER 6

STRUCTURAL MODEL

In the present work, a three dimensional structural model was developed as an extension of the thermal model shown in chapter 5. The developed structural model can be used to calculate the thermal stresses developing in the PV module as well the stress cycling it undergoes during day-to-day operation. The following sections discussion the mathematical background and the implementation of structural models with and without cooling. This is followed by a study to see the effect of varying atmospheric and operating conditions on the thermal stresses developing in the module.

6.1 STRUCTURAL MODEL

Finite element method was used to calculate the thermal stresses developing in the PV panel. For structural response, the principle of virtual work can be used to develop the finite element formulation. For a body constrained to move during a temperature change, the finite element formulation using principle of virtual work was given by Yilbas et al.[72]. Applying principle of virtual work to bodies under only temperature body load gives,

$$\left\{\delta u\right\}^T \int_{vol}[B]^T[D][B]dv\left\{u\right\} = \left\{\delta u\right\}^T \int_{vol}[B^T][D]\left\{\varepsilon^{th}\right\}dv \qquad (6.1)$$

Since $\left\{\delta u\right\}^T$ is an arbitrary displacement vector, the above equation reduces to,

$$[K]\left\{u\right\} = \left\{F^{th}\right\} \qquad (6.2)$$

where,

$[K] = \int_{vol}[B]^T[D][B]dv$ = element stiffness matrix

$\left\{F^{th}\right\} = \int_{vol}[B]^T[D]\left\{\varepsilon^{th}\right\}dv$ = element thermal load vector

$\left\{\varepsilon^{th}\right\} = \left\{\alpha\right\}\Delta T$ = thermal strain vector

$\left\{\alpha\right\} =$ vector of coefficient of thermal expansion

and $[B]$ is the displacement gradient matrix, $[D]$ is the material properties matrix and ΔT is the temperature difference from the reference condition. To calculate the thermal stresses developing in the body, the Hooke's law, given by equation (6.3), is used.

$$\left\{\sigma\right\} = \left[D\right]\left\{\varepsilon\right\} \qquad (6.3)$$

where $\{\sigma\}$ is the stress vector and $\{\varepsilon\}$ is the elastic strain vector equal to the difference of the total strain $\{\varepsilon_T\}$and thermal strains $\{\varepsilon^{th}\}$.

$$\left\{\varepsilon\right\} = \left\{\varepsilon_T\right\} - \left\{\varepsilon^{th}\right\} \qquad (6.4)$$

For a body under only temperature body load, the total strain is zero which leads to equation (6.5) for calculating the thermal stresses.

$$\{\sigma\} = [D]\{\varepsilon_{th}\} \tag{6.5}$$

In the present work, two structural models were implemented, one for PV panel without cooling and one for PV panels with cooling. The structural models are sequentially coupled with the thermal models. The details of both the models are presented below.

6.1.1 Implementation of Structural Model for PV Panel without Cooling

The structural model for PV panel without cooling was developed in *ANSYS Mechanical* code using SHELL181 layered structural elements. SHELL181 is a 4-node shell element with six degrees of freedom at each node and is suitable for analyzing thin to moderately thick shell structures. The geometric model as well as layer section definitions remained the same as the thermal model for panel without cooling. The structural properties for the PV panel materials are shown in Table 6.1. Temperature distribution calculated in the thermal analysis was applied to the model as body load. To restrain the model structurally, the four corners of the model are fixed in all degrees of freedom.

Table 6.1. Required material properties for structural model.

Material	**Layer**	**Modulus of Elasticity (GPa)**	**Poisson's Ratio**	**Coefficient of Thermal expansion (°C^{-1})**
Silicon	Solar cell	150	0.17	2.616e-6
Tempered Glass	Top cover	70	0.22	9e-6
Polyester	Bottom cover	4	0.37	60e-6
EVA	Encapsulant	7.8	0.3	90e-6
Aluminum		72	0.32	22e-6

6.1.2 Implementation of structural model for cooled PV panel

The structural model for cooled PV panel was implemented in ANSYS Mechanical environment. Only the PV panel was modeled for structural analysis using the same geometry and mesh as the thermal model. The finite element used was SOLID185 which is defined by eight nodes having three degrees of freedom at each node. The material properties are same as in the model without cooling, given in Table 6.1. The results of the thermal model of cooled PV panel were imported into the ANSYS Mechanical structural model and applied as body load. The boundary conditions applied were the same as in the structural model for PV panels without cooling and the four corners of the panel were constrained.

6.2 PARAMTERIC STUDY – STRUCTURAL PERFORMANCE UNDER VARYING ATMOSPHERIC AND OPERATING CONDITIONS

Using the developed structural models, the parametric study carried out in section 5.3 was extended to study the effect of environmental factors such as ambient temperature and solar irradiance and operating conditions such as heat exchanger inlet fluid velocity and inlet fluid temperature on the structural performance of PV panels. The same standard conditions of 800 W/m^2 absorbed radiation, 25°C ambient temperature and for cooling, inlet water velocity and temperature equal to 0.05 m/s and 25°C respectively with a perfect contact between the PV panel and the heat exchanger were used in the conducted study.

Fig. 6.1, Fig. 6.2 and Fig. 6.3 respectively show a comparison of the two in-plane stress components, x-component along the width and z-component along the length of the panel, and the von Mises stress for the panels with and without cooling. The very high magnitudes of stresses at and near the four corners were due the applied boundary conditions. The maximum stresses in x-direction in the panel without and with cooling away from the boundary were 58.2MPa and 6.01MPa. In the z-direction, the stress magnitudes away from the boundary effects were 32.5MPa and 6.15MPa for the panels without and with cooling respectively. The maximum von Mises stress in the panel without cooling was 65.5MPa while in the cooled panel the maximum von Mises stress was 6.68MPa.

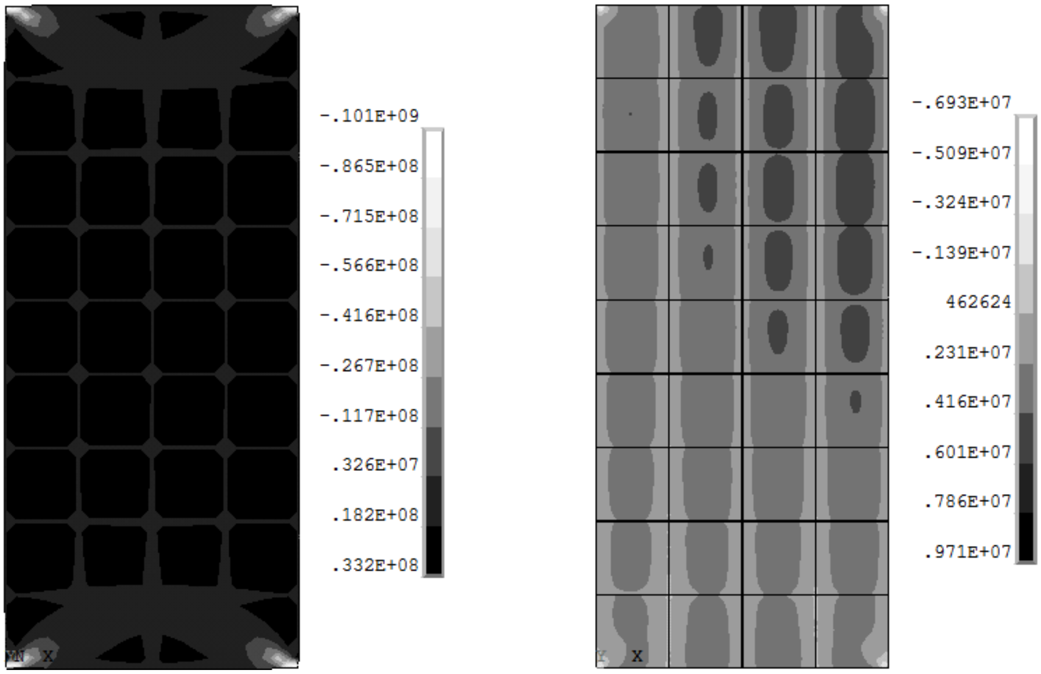

(a) (b)

Fig. 6.1. X-Component of Stress in PV Cells.

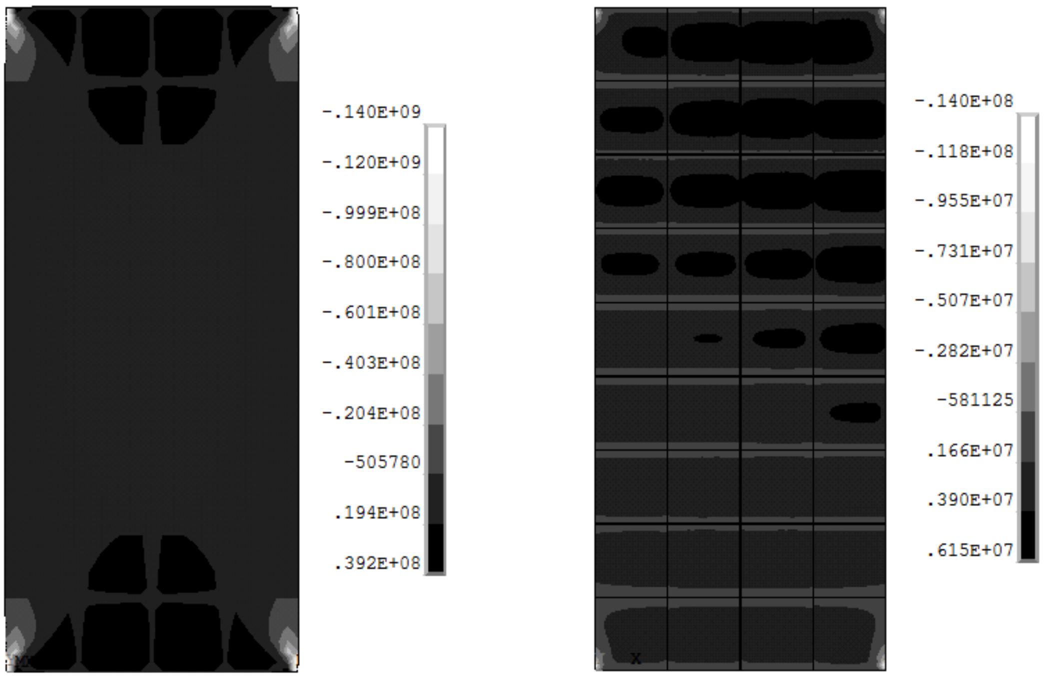

(a) (b)

Fig. 6.2. Z-Component of Stress in PV Cells.

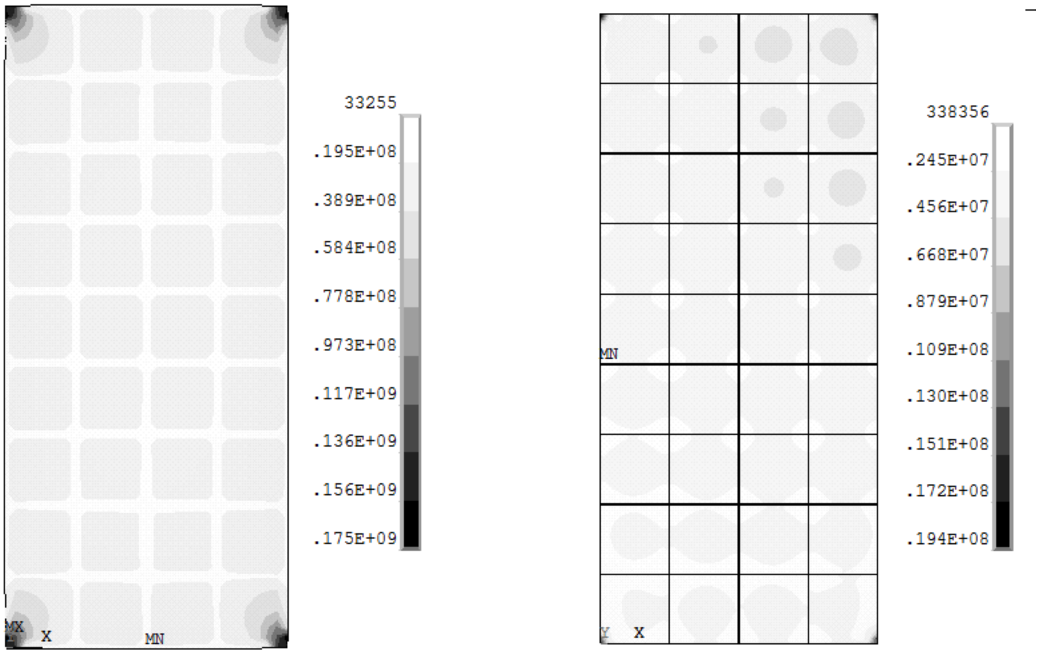

(a) (b)

Fig. 6.3. von Mises Stress in PV Cells.

To compare the spatial variation of stresses in the panel, the von Mises stress was plotted along four different paths in the plane of the panel and one path along its thickness. The five paths are shown in Fig. 6.4.

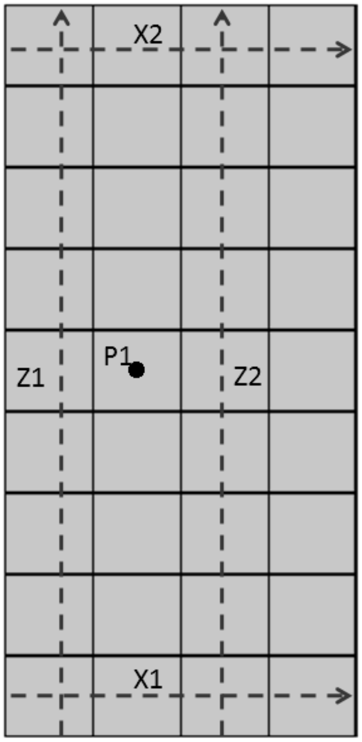

Fig. 6.4. Location of paths for studying spatial stress variation

Fig. 6.5(a) and Fig. 6.5(c) show the temperature variation along paths X1 and X2 respectively. Both these figures show that the variation in temperature for the panel without cooling was periodic around 62.9°C while the temperature for the cooled panel increased along path X1 from 29.5°C to 30.1°C and 31.4°C to33.4°C for path X2. Fig. 6.5(b) and Fig. 6.5(d) show the von Mises stress variation along the paths. The high stresses at the beginning and the end of the paths for the panel without cooling were due to the effect of the boundary condition. The stresses in the panel with cooling (4MPa for path X1 and 3MPa for X2) were one order of magnitude lower than those in the panel without cooling (29MPa).

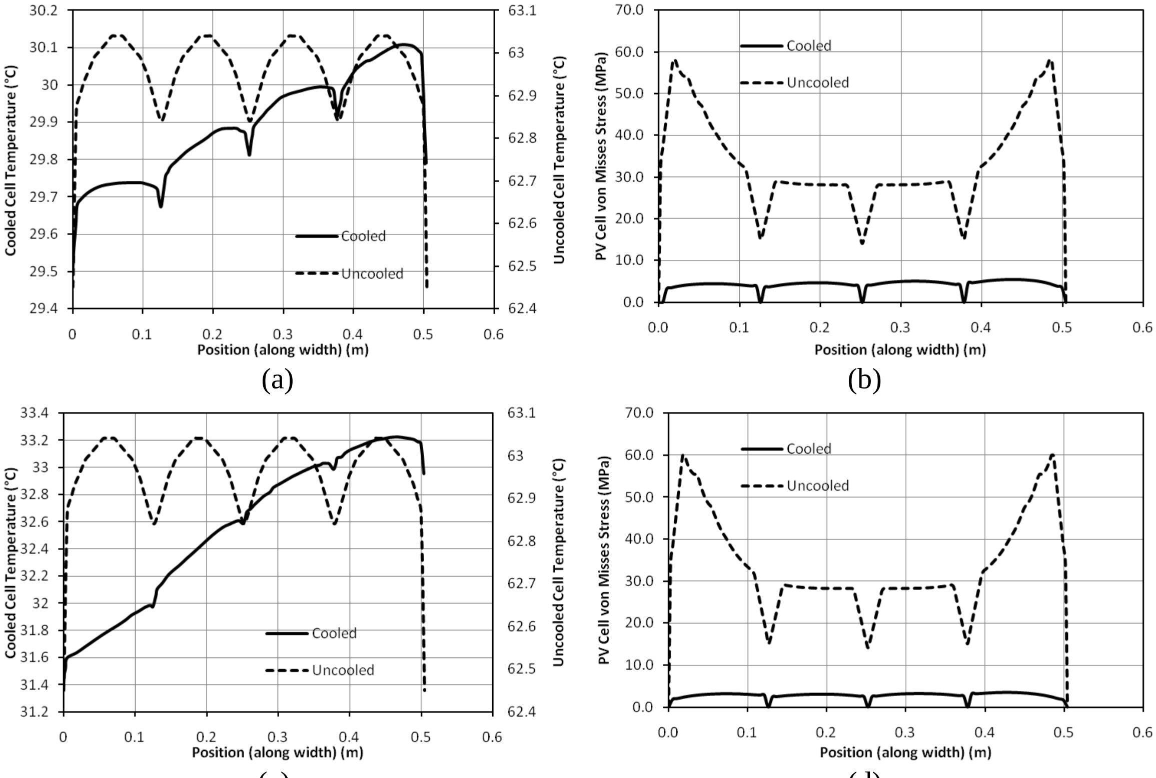

(a) (b)

(c) (d)

Fig. 6.5. Variation of PV cell temperature and von Mises stress along paths X1 and X2.

For the paths Z1 and Z2, similar trends were observed. The temperature variation along the paths, shown in Fig. 6.6(a) and Fig. 6.5(c) was periodic centered at about 62.9°C for the panel without cooling while for the panel with cooling it showed an increase of about 2.5°C for path Z1 and 3.5°C for path Z2 in the direction of the paths. The difference between the temperature of the cooled and uncooled panels was around 30°C. The variations in von Mises stress along the paths are shown in Fig. 6.5(b) and Fig. 6.5(d). The effect of boundary conditions is seen again in the figures but the effects are much lower in path Z2 which is not directly adjacent to the boundary. Away from the boundaries, the maximum stresses were around 28MPa for both paths Z1 and Z2. For the cooled panel, an increase of around 1MPa was observed in the direction of the path.

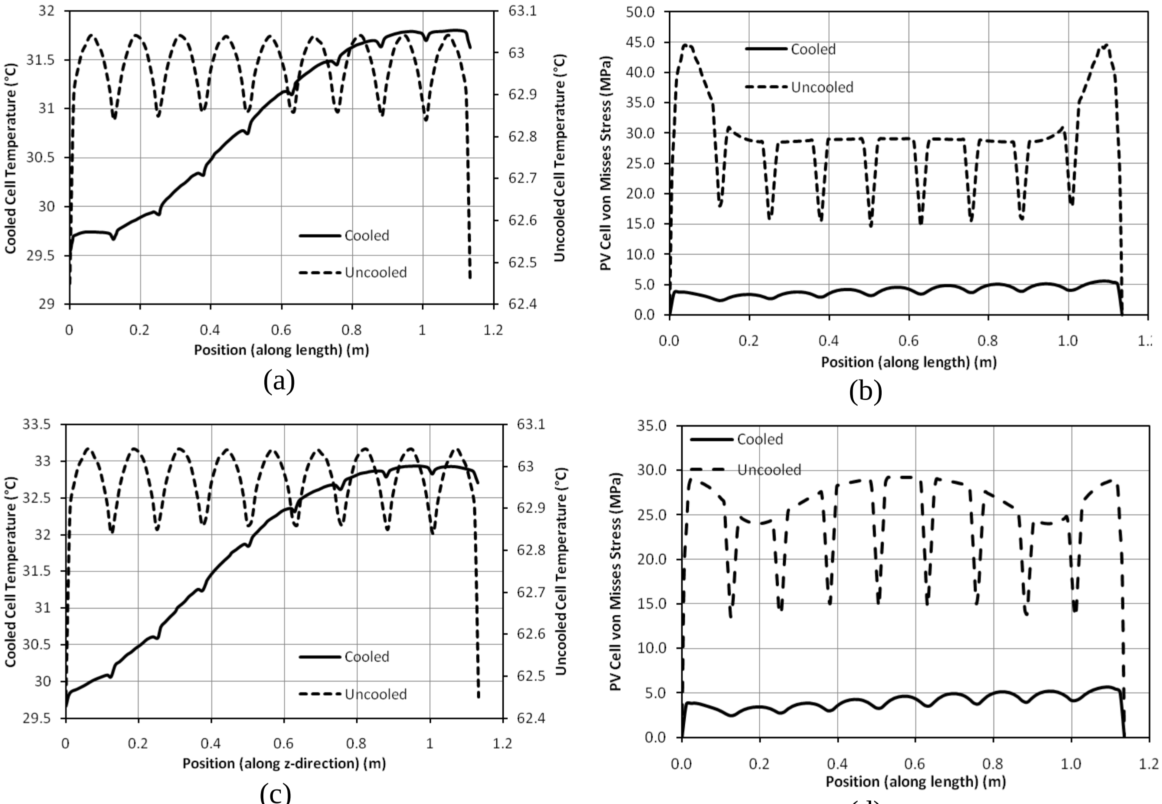

(a)

(b)

(c)

(d)

Fig. 6.6. Variation of PV cell temperature and von Mises stress along paths Z1 and Z2.

The variation of temperature and von Mises stress along the path P1 which runs along the thickness is shown in Fig. 6.7. The temperature variation for the panel without cooling covered a range of about 1.4°C while the range was about 2.2°C for the cooled panel. The minimum temperature for the cooled panel was at the top surface which is farthest from the PV cell and had higher convection heat loss coefficient than the bottom surface. The minimum temperature for the cooled panel was at the lower surface which is expected since that is the surface in contact with the heat exchanger. The von Mises stress variation, shown in Fig. 6.7(b), shows that the maximum stresses were in the PV cell layer. The sudden variation in stress between the layers was due to the variation of material properties.

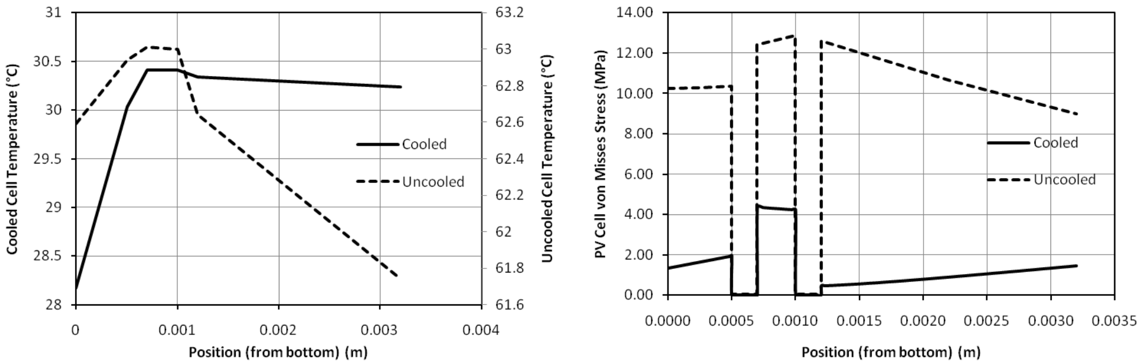

(a) (b)

Fig. 6.7. Variation of PV cell temperature and von Mises stress along path P1.

To study the variation of stresses with environmental and operating conditions, von Mises stresses in the PV cells at a point away from the boundaries were plotted by varying one parameter at a time. In Fig. 6.8(a), the stress variation when the absorbed solar radiation was varied from 400 W/m^2 to 3000 W/m^2 is shown. The figure shows that the variation of stresses in cooled panel is much lower than the panel without cooling. A similar phenomenon was observed in Fig. 6.8(b) in which the ambient temperature is varied from 0°C to 50°C. This range, therefore, covers ambient temperatures for cold to very hot environments. For the panel without cooling, the stresses increased from 10 MPa to about 50 MPa whereas the increase in stresses for the cooled panel was only around 8 MPa. Fig. 6.8(c) and Fig. 6.8(d) show the variation in von Mises stresses with the operating conditions of heat exchanger i.e. inlet water temperature and velocity respectively and therefore, only the variation of stresses in the cooled PV panel were plotted in these figures. In Fig. 6.8(c), the inlet water temperature was varied from 5°C to 45°C. The figure shows that at 15°C inlet temperature, the von Mises stress in the PV panel was minimum. This is because at this temperature, the PV cell temperature is closest to the reference temperature chosen for calculating the thermal strain (equal to 25°C). Fig. 6.8(d) showed that the stresses in the PV cells reduced as the water inlet velocity was increased because of lower PV cell temperatures.

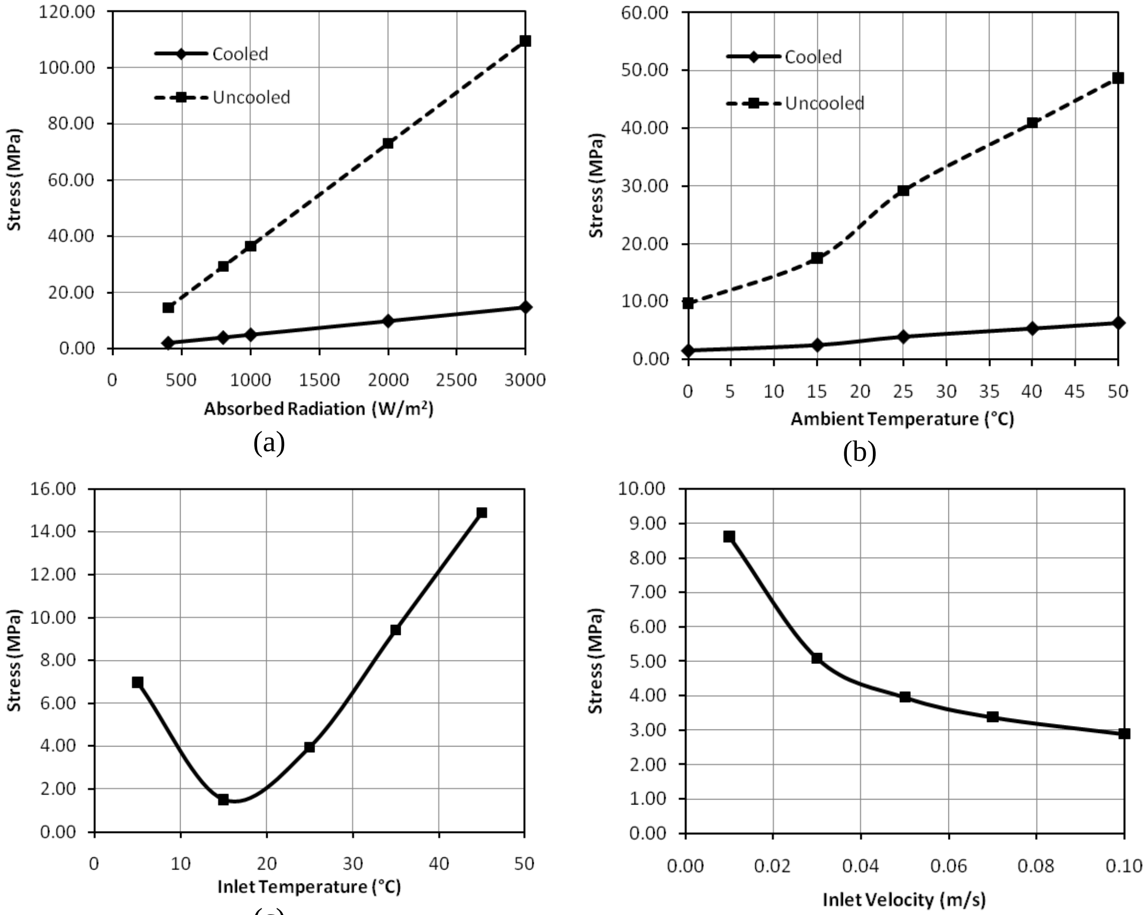

(a) (b) (c) (d)

Fig. 6.8. Variation of von Mises stress in PV cells with operating and environmental conditions.

6.2.1 Conclusion

A model to predict the thermal and structural performance of the PV system for given environmental and operating conditions has been presented in this paper and validated. From the conducted study, the following conclusions are drawn.

- The effectiveness of cooling in reducing the thermal stress in the module increases as the solar radiation or the ambient temperature increases. This implies that cooling is more effective in areas like the Middle East which have high solar resource and hot environments.
- As can be seen from Fig. 6.8(a), the von Mises stress when the absorbed radiation was 3000 W/m^2 was 110 MPa. Stress cycling at such high stress magnitudes can lead to failures in the cell. This suggests that from a structural point of view, cooling becomes increasingly important as concentration is increased.
- From Fig. 6.8(c), the influence of the selected strain-free temperature can be seen. In the future, there is a need to standardize the reference temperature for thermo-structural analyses.

CHAPTER 7

MULTIPHYSICS MODEL AND TRANSIENT ANALYSIS

In the previous chapters, development of various sub-models required for PV performance prediction has been presented. When the thermal, structural and electrical performance of the PV panels needs to be simulated, all of these models need to be coupled together to form a multi-physics model. This chapter first discusses the overall multi-physics model followed by a transient analysis of the thermal, structural and electrical performance of a PV module under real-life meteorological conditions measured at Jeddah, Saudi Arabia.

7.1 OVERAL MULTI-PHYSICS MODEL

The overall multi-physics model comprises four different physical models: radiation & optical, electrical, thermal and structural. The external inputs required are the meteorological data and the PV site information. Fig. 7.1 shows the flow chart of the multi-physics performance prediction model for photovoltaic panels developed in this work.

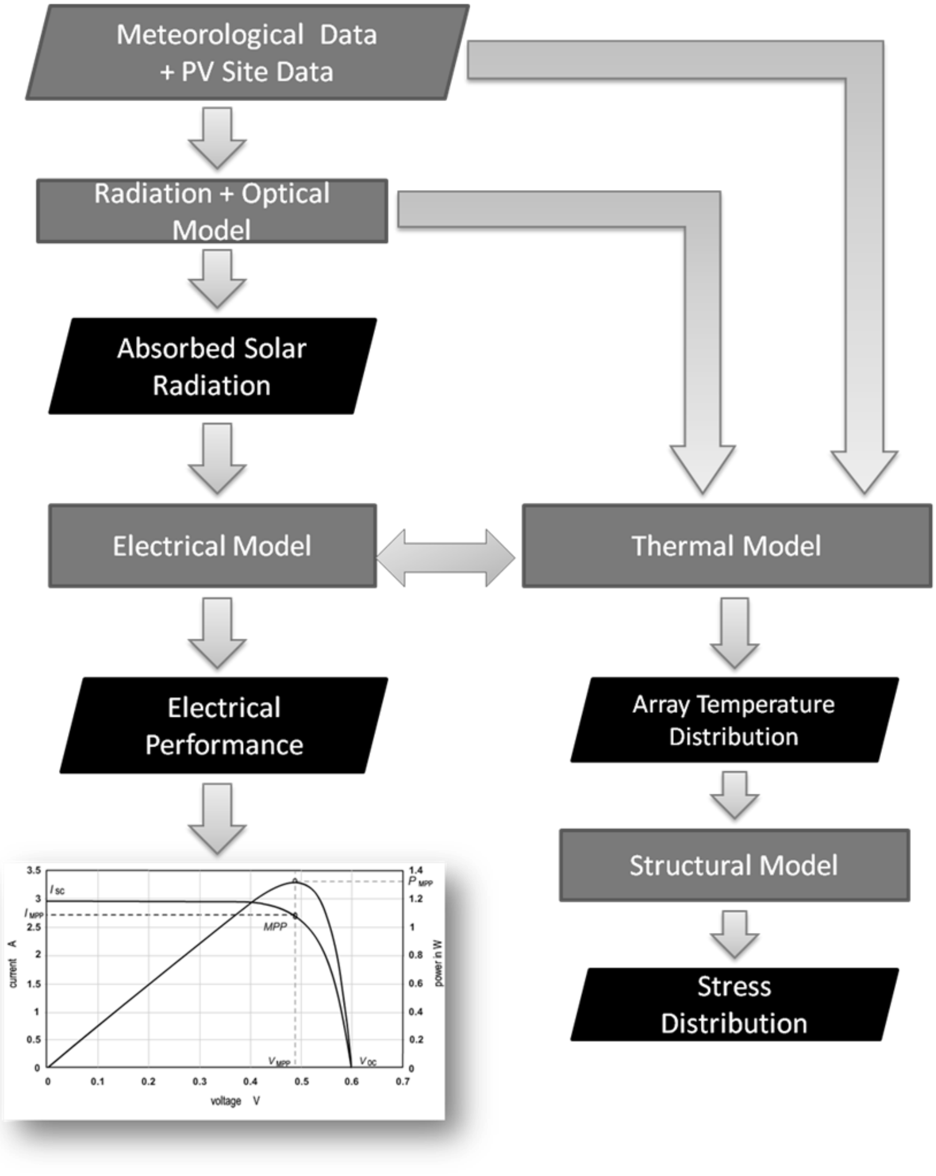

Fig. 7.1. Overall multi-physics model of PV modules.

The radiation & optical model is sequentially coupled with the thermal model and the electrical providing them with the solar energy absorbed in the panel. The electrical and thermal models, on the other hand, affect each other both ways. This is because the electrical conversion efficiency of PV panels is a function of PV cell temperature while the heat generation in the thermal model that controls the temperature distribution in the PV panel is dependent on electrical efficiency. To handle this complexity, an analytical expression for PV cell temperature as a function of average PV cell temperature was incorporated in the two thermal models. This analytical expression was formed by first differentiating the electrical efficiency with respect to PV cell temperature which gives Eq. (7.1). It was then used to calculate the electrical efficiency at each iteration using equation (7.2).

$$\frac{\partial \eta_{pv}}{\partial T_{cell}} = \frac{1}{GA_{panel}} \left(I_{mp} \frac{\partial V_{mp}}{\partial T_{cell}} + V_{mp} \frac{\partial I_{mp}}{\partial T_{cell}} \right) \tag{7.1}$$

$$\eta_{pv} = \eta_{pv,ref} \left(1 - \frac{\partial \eta_{pv}}{\partial T_{cell}} \left(T_{cell,avg} - T_{cell,ref} \right) \right) \tag{7.2}$$

where T_{cell} is PV cell temperature, $T_{cell,avg}$ is the average cell temperature in the PV panel, G is the incident solar radiation, A_{panel} is the front surface area of the PV panel and I_{mp} and V_{mp} are the maximum power point current and voltage . For the model of panel without cooling, the above methodology cannot be employed. This is because ANSYS Mechanical in which the model without cooling has been implemented, does not use iterative solver. Therefore, instead of using the PV cell temperature from the same time step in equation (7.2), the cell temperature from the previous time step was used.

7.2 TRANSIENT ANALYSIS

Using the developed multi-physics model, the thermal, structural and electrical performance of a crystalline silicon PV module (AstroPower AP-110) was simulated for four days with different meteorological conditions in Jeddah, Saudi Arabia. The time step selected for the transient analysis was set to 15 minutes. The input conditions used in the models were converted to 15 minute data and then used in the model. The simulations were started at 12:15 am and continued till 11:45 pm.

The ambient temperature and total irradiance on a horizontal plane for the four selected days is presented in Fig. 7.2. The total horizontal irradiance was used to calculate absorbed solar radiation in the PV cells using HDKR model [10] described in section 4.2.2. The absorbed radiation and the ambient temperature were used in the thermal model to calculate the temperature distribution in the PV panel which was then used to calculate the stress distribution inside the panel. The electrical model used the absorbed radiation and average PV cell temperature to calculate the electrical power output and the electrical efficiency throughout the day.

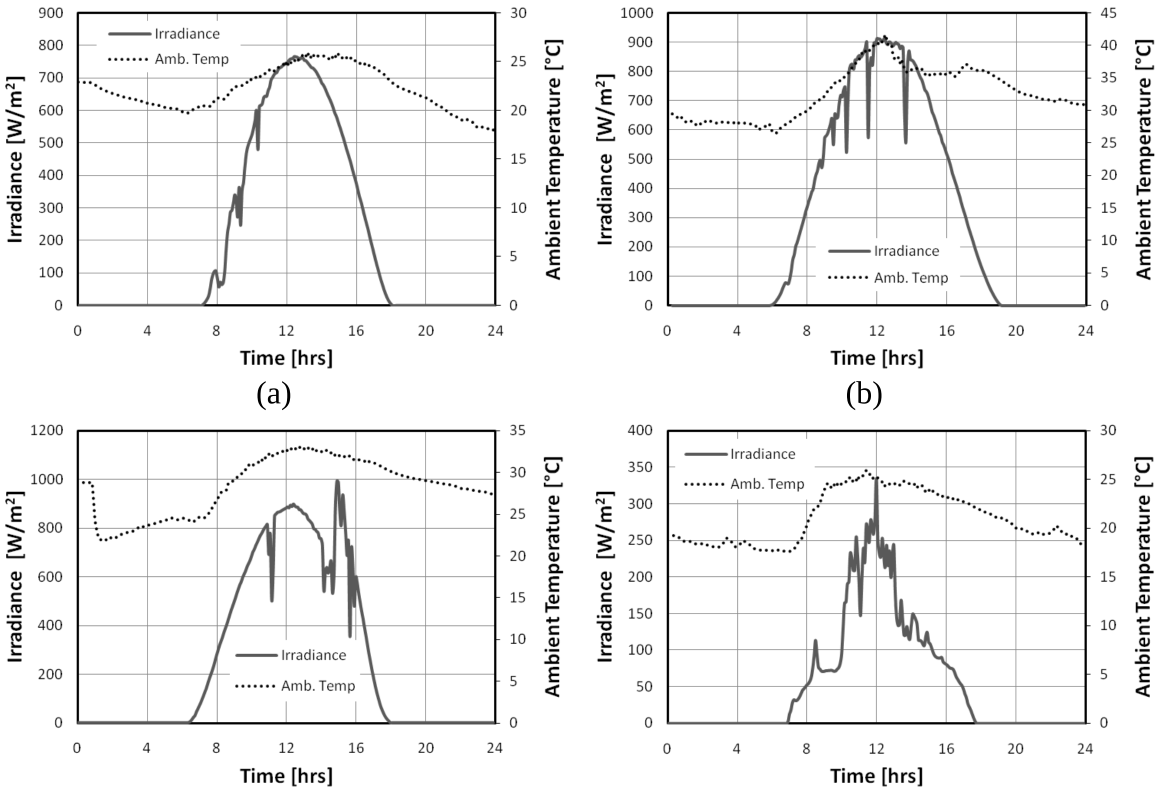

(a) (b)

(c) (d)

Fig. 7.2. Input meteorological conditions for (a) January 17, 2000 (b) July 17, 2000 (c) October 15, 2000 and (d) December 10, 2000

7.2.1 Results and Discussion

For studying the spatial and temporal variation of temperatures and stresses, initially one day was studied in detail. This was followed by a comparison of the temperatures and stresses developing in the panel for all four simulated days. To study the spatial distribution of temperature and stress, five paths were defined along the PV panel. Paths P1 and P2 were used to examine the variation of stresses and temperatures along the length of the panel while paths P3 and P4 were used to study the variations along the panel's width. The fifth path was along the thickness of the panel starting from the bottom at location T1. All paths are shown in Fig. 7.3.

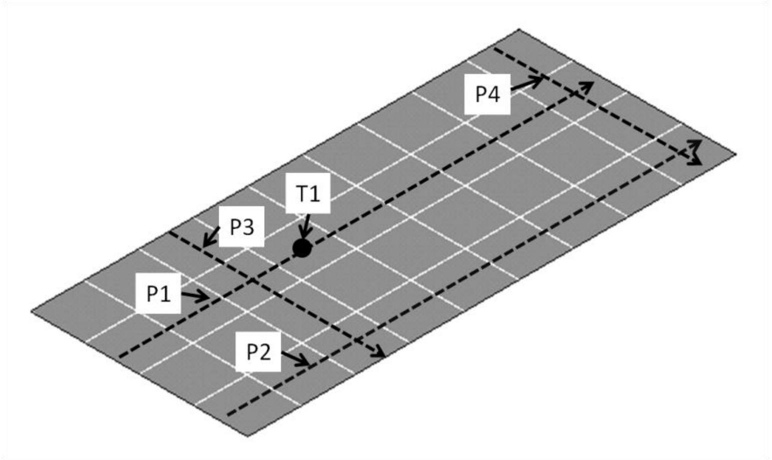

Fig. 7.3. Paths for studying spatial distribution of temperature and stresses

The day selected for the detailed study was July 17, 2000 because of its high and uniformly distributed solar irradiance and high ambient temperatures. For July 17, the time variation of temperature and von Mises stress in the PV cell at point T1 for PV panel with and without cooling is shown in Fig. 7.4. The maximum cell temperature occurred at

12:30 and was 74.7°C for panel without cooling and 33.1°C for panel with cooling. The corresponding maximum von Mises stress values for the panel without cooling and with cooling were 38MPa and 4.6MPa respectively. Fig. 7.4(b) shows that the PV cells underwent one major stress cycle and several minor stress cycles in one day. The major stress cycle was due to the daily solar irradiance variation from sunrise to sunset while the minor stress cycles were due to other environmental variations such as ambient temperature and cloud conditions. It is also important to note that the stress cycling for the PV panel without cooling was much more severe (2MPa-38MPa) than the panel without cooling (0.3MPa-4.6MPa).

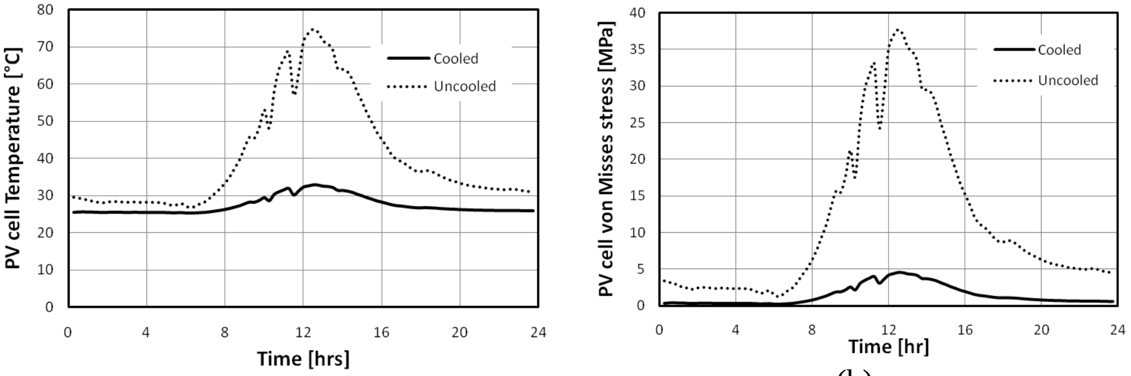

(a) (b)

Fig. 7.4. Time variation of (a) PV cell temperature (b) von Mises stress

For the time 12:30pm when the PV cell temperature and stresses were maximum, the spatial distribution of temperature and stresses were plotted and are shown in Fig. 7.5 to Fig. 7.9 which show the variation of PV cell temperature and von Mises stress, 1st principal stress and 2nd principal stress in the PV cells along paths P1, P2, P3 and P4 and across the thickness at location T1. The 3rd principal stress for the PV cell layer was found to be several orders of magnitude lower than the 1st and 2nd principal stresses and thus not shown in figures Fig. 7.5 to Fig. 7.8.

Fig. 7.5(a) shows the PV cell temperature variation along path P1 in the panels with and without cooling. It is clear from the figure that for the panel without cooling, the cell temperature remained almost constant along the entire path at around 74.5°C while there was a 4.5°C rise in temperature for the cooled panel along the same path. Fig. 7.5(b) shows the variation of von Mises stress along path P1. In the figure, stress values for the first and the last cells include the effect of the applied boundary condition and therefore should be neglected. This effect is clear from the stress variation curve for the PV panel without cooling. Along, the path, the panel without cooling showed symmetric variation in stress with the middle cell showing the maximum von Mises stress (37MPa). The cooled panel showed one order of magnitude lower stress values (around 1MPa) with a gradual increase in the stress along the path due to the increase in the cell temperature. In the panel without cooling there was also a strong stress gradient between the cells. The stress gradient dropped significantly for the cooled panel. Fig. 7.5(c) which shows the variation of 1st principal stress along the path shows a similar behavior to von Mises stress. The maximum stress 1st principal stress for the panel without cooling was around

44MPa while the cooled panel showed a gradual increase in 1st principal stress values from 4MPa to 6MPa. Finally, Fig. 7.5(d) shows the variation of 2nd principal stress along the path. The 2nd principal stress showed a behavior opposite to the von Mises and 1st principal stresses with the minimum stress (21MPa) occurring in the middle cell. The behavior of the cooled panel was similar behavior to the von Mises and 1st stress with a gradual increase in stresses from around 3.8MPa to 5.8MPa.

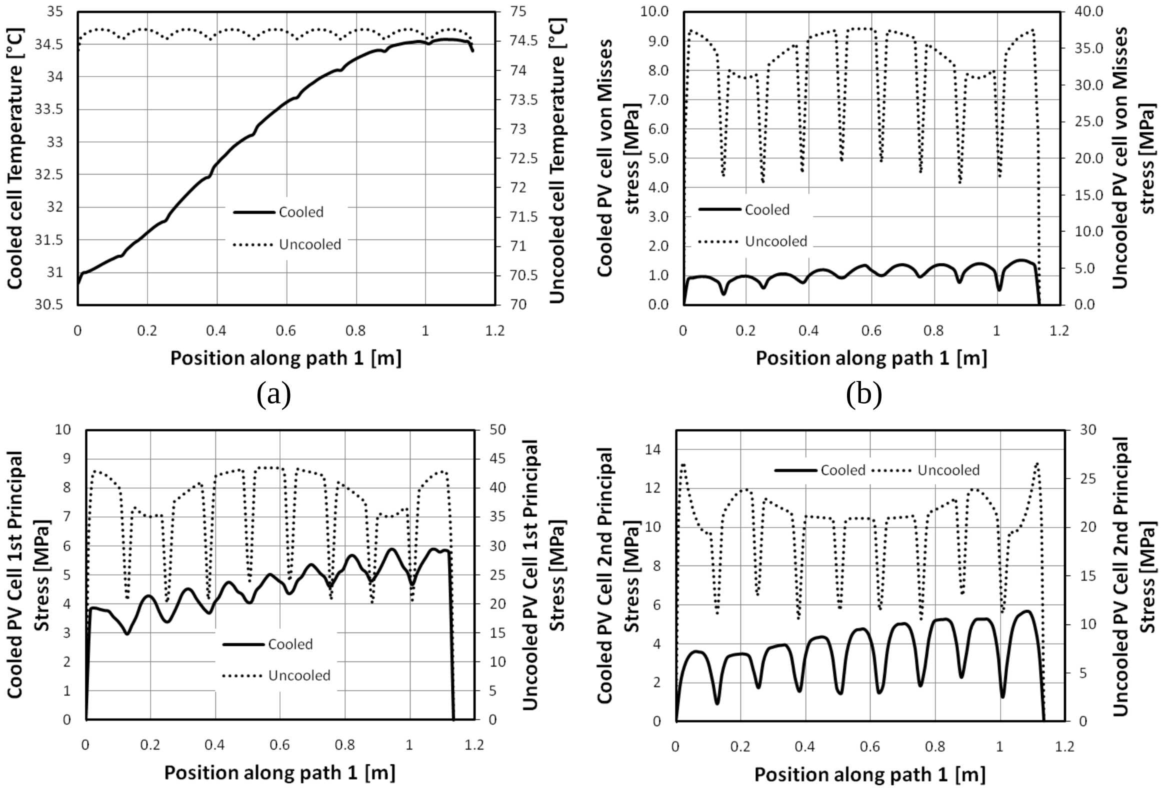

(a) (b)

(c) (d)

Fig. 7.5. Along path 1: (a) temperature (b) von Mises stress (c) 1st Principal Stress (d) 2nd Principal stress

Fig. 7.6 shows the variation of PV cell temperature and stresses along path P2. The cell temperature for the panel without cooling was 74.5°C, same as path P1. The cooled panel showed a 5.5°C rise in temperature which was 1°C higher than path P1. This indicates a lower fluid flow in the heat exchanger along path P2 resulting in higher temperatures. The von Mises stress and 1st principal stress for P2 show similar behavior to path P1. The stress values for the panel without cooling were also equal to those for path P1 away from the edges which show a higher effect of boundary conditions because path P2 is closer to the edge than P1. The stress values for the cooled panel were slightly higher than path P1 towards the end due to slightly higher temperatures. The variation for the 2nd principal stress for the panel without cooling along P2 was different from P1 with the maximum stress (23MPa) occurring in the middle cell. For the cooled panel, there was a gradual increase in stress, similar to P1, with slightly higher magnitudes than those along P1.

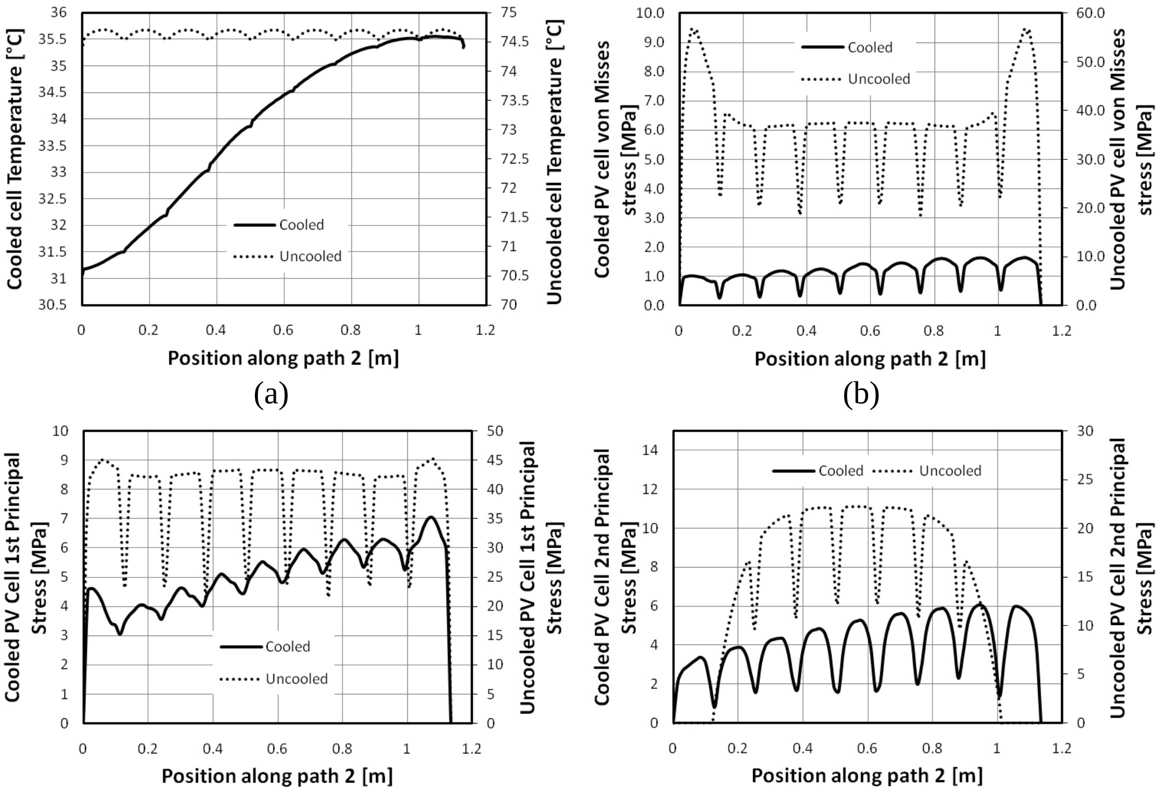

(a) (b)

(c) (d)

Fig. 7.6. Along path 2: (a) temperature (b) von Mises stress (c) 1st Principal Stress (d) 2nd Principal stress

Fig. 7.7 shows the variation of cell temperature and stresses along path P3 which is perpendicular to P1 and P2 and away from the applied boundary conditions. The cell temperature along the path, shown in Fig. 7.7(a), was constant at 74.5°C for the panel without cooling similar to paths P1 and P2 while there was a 1.5°C rise in cell temperature along the path for the cooled panel. In Fig. 7.7(b), Fig. 7.7(c) and Fig. 7.7(d) which show the stress variation along path P3, a pattern similar to the stress variation for the first two and last two cells along path P1 is seen. The stresses for the cooled panel showed a slight increase along the path.

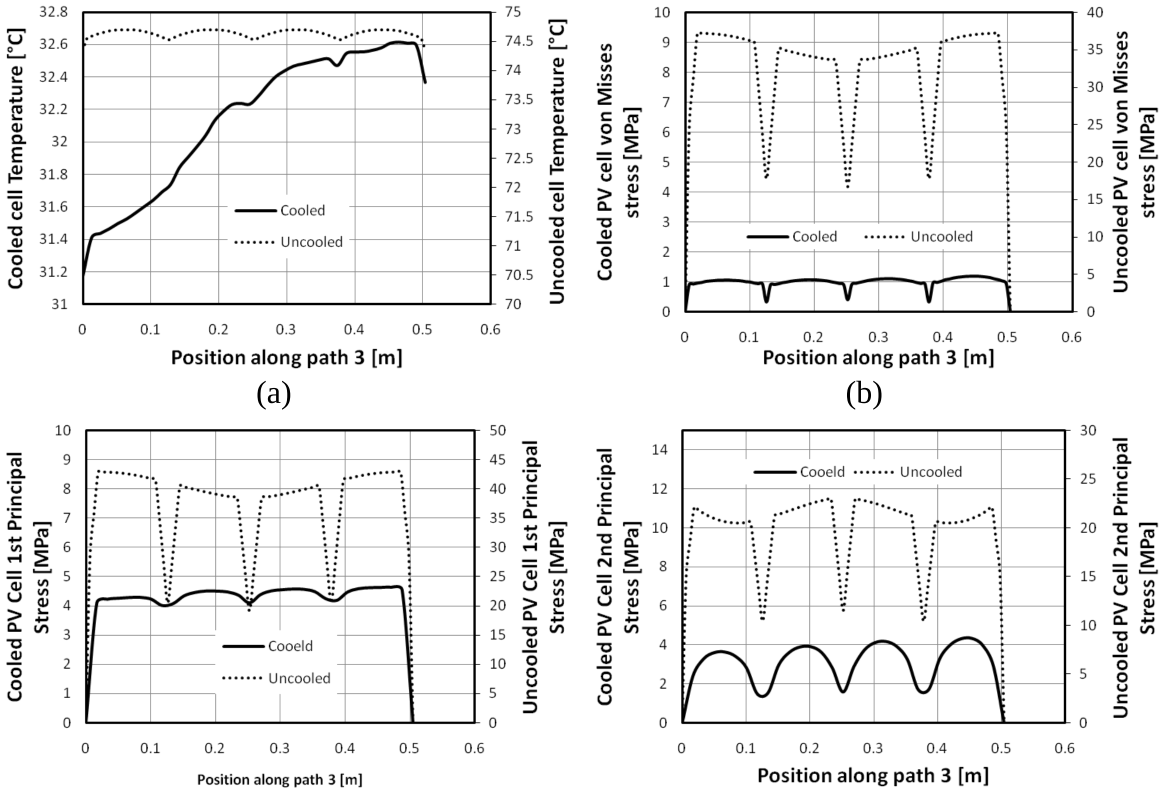

(c) (d)

Fig. 7.7. Along path 3: (a) temperature (b) von Mises stress (c) 1st Principal Stress (d) 2nd Principal stress

Fig. 7.8 shows the variation of cell temperature and stresses along path P4 which is perpendicular to P1 and P2, parallel to P3 and adjacent to the applied boundary conditions. The cell temperature along the path, shown in Fig. 7.8(a), was constant at 74.5°C for the panel without cooling. There was a 2°C rise in cell temperature along the path for the cooled panel. Fig. 7.8(b), Fig. 7.8(c) and Fig. 7.8(d) showed the stress variation along path P4. In these figures, a pattern similar to the stress variation for the first two and last two cells along path P2 is seen while there is a slight increase in stresses for the cooled panel.

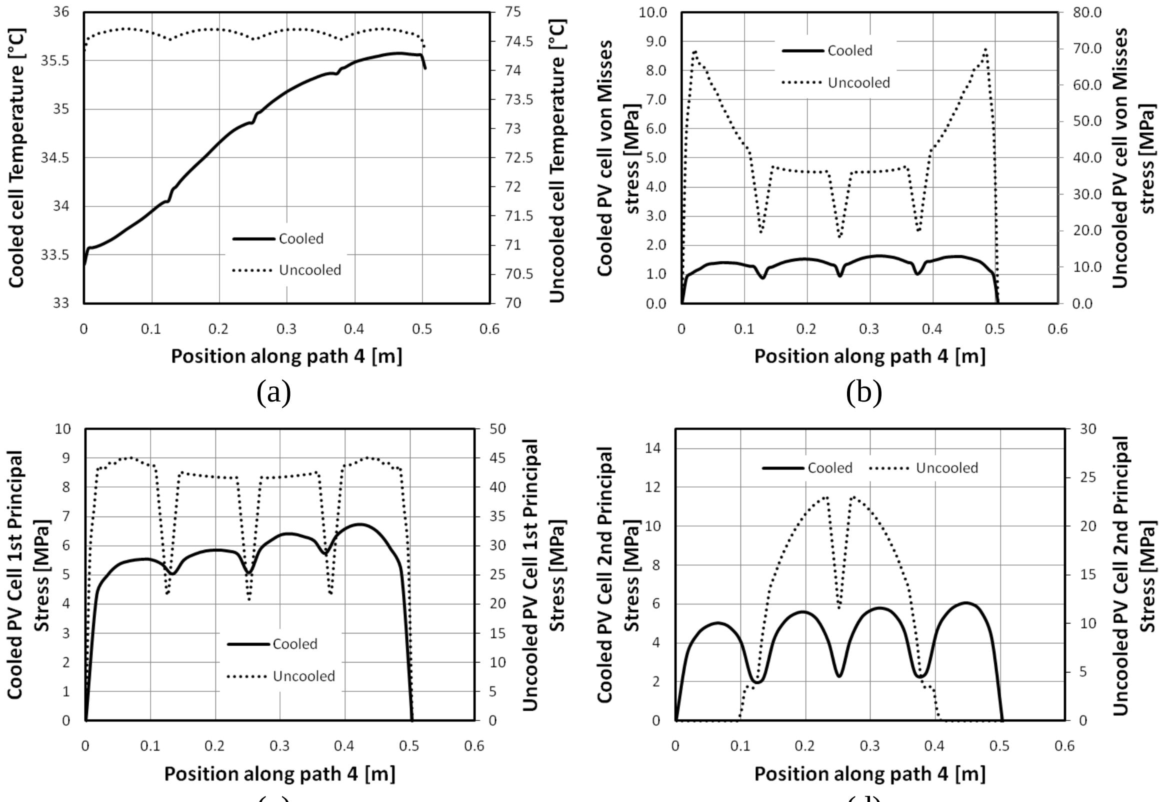

(a) (b)

(c) (d)

Fig. 7.8. Along path 4: (a) temperature (b) von Mises stress (c) 1st Principal Stress (d) 2nd Principal stress

In all four figures, Fig. 7.5-Fig. 7.8, the PV cell temperature for PV panel without cooling showed almost constant values along the paths with cyclic variation within 0.2°C. On the other hand, the cell temperature for cooled PV panel showed almost 5°C rise along paths P1 and P2 and 2.5°C rise along paths P3 and P4. Also, the temperatures along P2 were higher than those along P1. Similarly, the temperatures along P4 were higher than the temperatures along P3. The non-uniformity of cell temperatures in parallel paths in the cooled panel was due to non-uniform flow in the heat exchanger. In the stress curves for the four paths, the first and the last cell show the effect of the boundary condition and therefore their stress values should be neglected. A comparison of the stress values of PV panels with and without cooling shows that stresses for the panel without cooling were one order of magnitude higher than those for the cooled panel.

Fig. 7.9 shows the temperature and stress variation across the thickness of the PV panel at location T1. The temperature variation is shown in Fig. 7.9(a). It shows that PV panels with and without cooling have different types of variation along the thickness of the panel. For the panel without cooling, the temperature varied between 73.6°C and 74.7°C with the minimum temperature being at the top where the convection losses were maximum. For the panel with cooling, the temperature varied between 30°C and 33.1°C with the minimum temperature being at the bottom where the heat exchanger is attached. Fig. 7.9(b) shows the von Mises stress variation across the thickness. The figure shows no significant stresses developing in the encapsulent layer due to the very low elastic modulus of the encapsulent material. For panels with as well as without cooling, the maximum stresses occurred in the PV cell layer (37.5MPa for the panel without cooling and 4.6MPa for the cooled panel). The variation of the 1st principal stress across the thickness, shown in Fig. Fig. 7.9(c), showed that the 1st principal stress values for all the layers were negligibly small except for the PV cells layer where the 1st principal stress was 44MPa for the panel without cooling and 5MPa for the cooled panel. The variation of 2nd principal stress across the thickness is shown in Fig. 7.9(d). The figure shows tensile stress for the PV cells layer and compressive stress for the back sheet and the front cover glass. Finally, Fig. 7.9(e) shows the variation of 3rd principal stress across the thickness. The figure shows that the value of 3rd principal stress for the PV cell layer was zero while that for the front cover and the back sheet, the 3rd principal stress was compressive in nature.

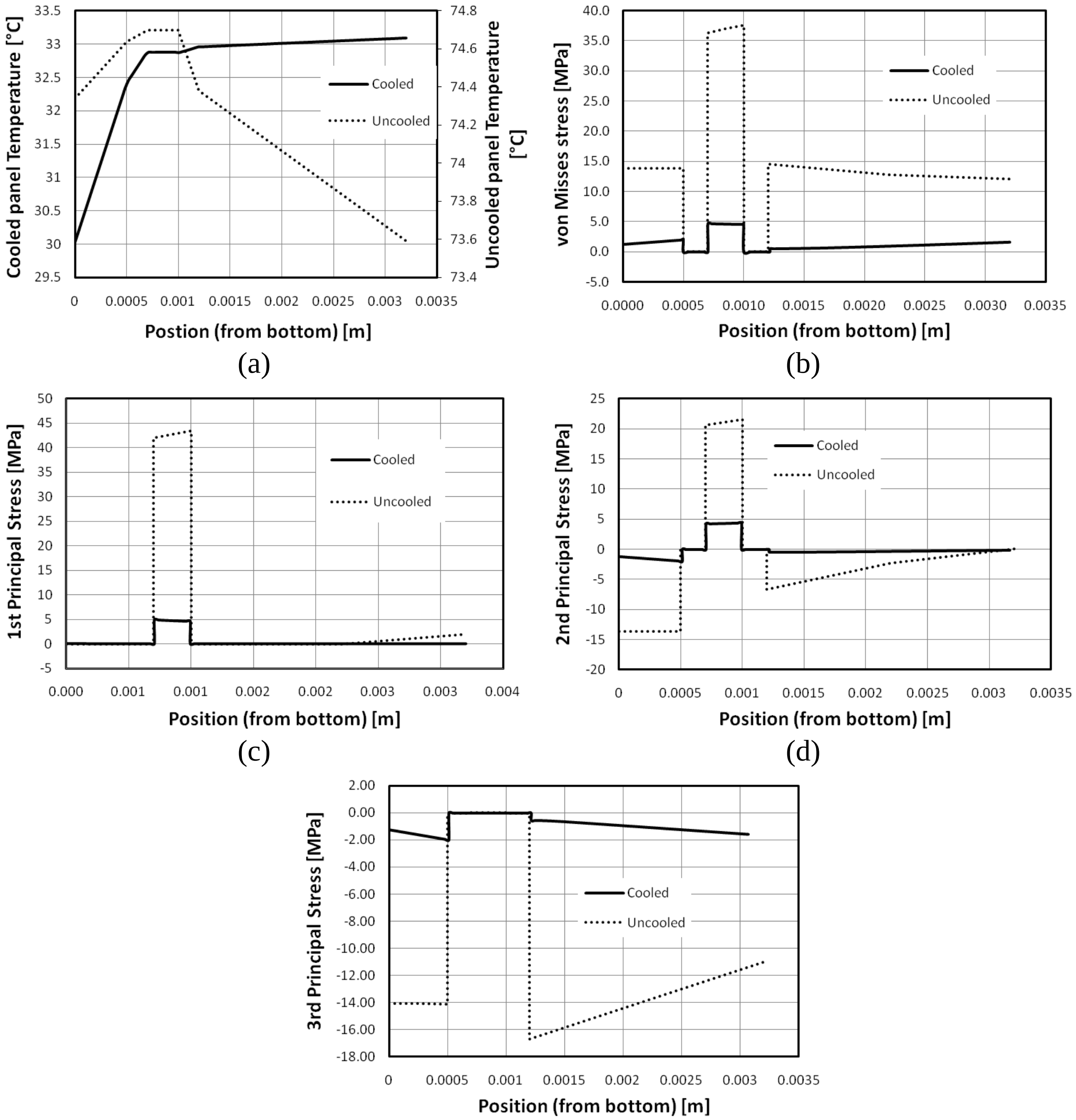

(a) (b) (c) (d) (e)

Fig. 7.9. Across thickness: (a) temperature (b) von Mises stress (c) 1st Principal Stress (d) 2nd Principal stress (e) 3rd Principal stress

For the remaining three days i.e January 17, 2000, October 15, 2000 and December 10, 2000, the temporal and spatial variations of temperature and stresses are shown in Fig. 7.10, Fig. 7.11 and Fig. 7.12. For studying the spatial variation along the length, path p2 was selected. Results across thickness at point T1 were also plotted.

In Fig. 7.10(a) and Fig. 7.10(b), the temporal variation of PV cell temperature and stress at point T1 is shown for January 17, 2000. The maximum temperature for the day occurred at 12:30 pm and was 61°C for the panel without cooling and 31°C for the cooled panel. Because the strain-free temperature was assumed to be 25°C, the von Mises stress showed zero magnitude when the PV cell temperature equaled 25°C. The maximum von Mises stress for the panel without cooling was 27MPa and for the cooled panel was 3.5MPa. Fig. 7.10(c), Fig. 7.10(d), Fig. 7.10(e) and Fig. 7.10(f) show the variations of temperatures and stresses along path P2 and across thickness at point T1 at time 12:30 pm. The figures show variation patterns similar to those seen for July 17, 2000.

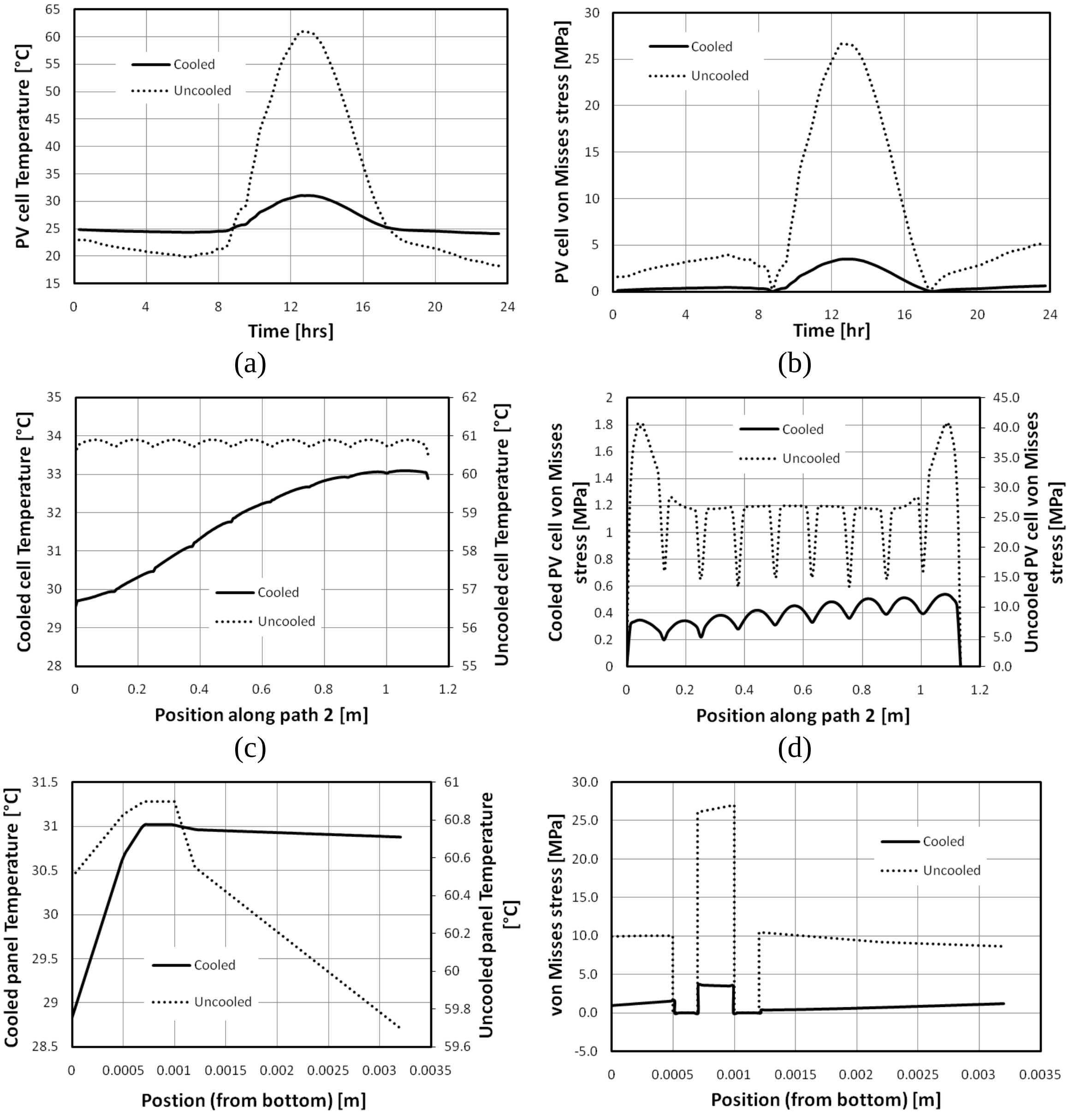

(a) (b)

(c) (d)

(e) (f)

Fig. 7.10. Temporal and spatial variation of temperature and stress in PV panel for January 17, 2000.

For October 15, 2000, the temporal and spatial variation of temperature and stress is shown in Fig. 7.11. The temporal variation, shown in Fig. 7.11(a) and Fig. 7.11(b) shows several temperature and stress cycles occurring during the day due to the variation of irradiance during the day. The maximum PV cell temperature occurred at 3:45 pm and was 84°C while the maximum stress in the PV cells was 44MPa for the panel without cooling. For cooled panel, the maximum temperature was 35°C and the maximum stress was 5MPa. Fig. 7.11(c) and Fig. 7.11(d) show the variation of temperature and stress along path P2. The PV cell temperature for panel without cooling was around 84°C while the PV cell temperature for the cooled panel increased from 32.3°C to 37°C. A similar situation was seen for PV cell von Mises stress. Away from the boundary, the stress in the uncooled panel was around 45MPa. The maximum stress for the cooled panel was 7.5MPa. Fig. 7.11(e) and Fig. 7.11(f) show the variation of temperature and stress across the thickness at point T1.

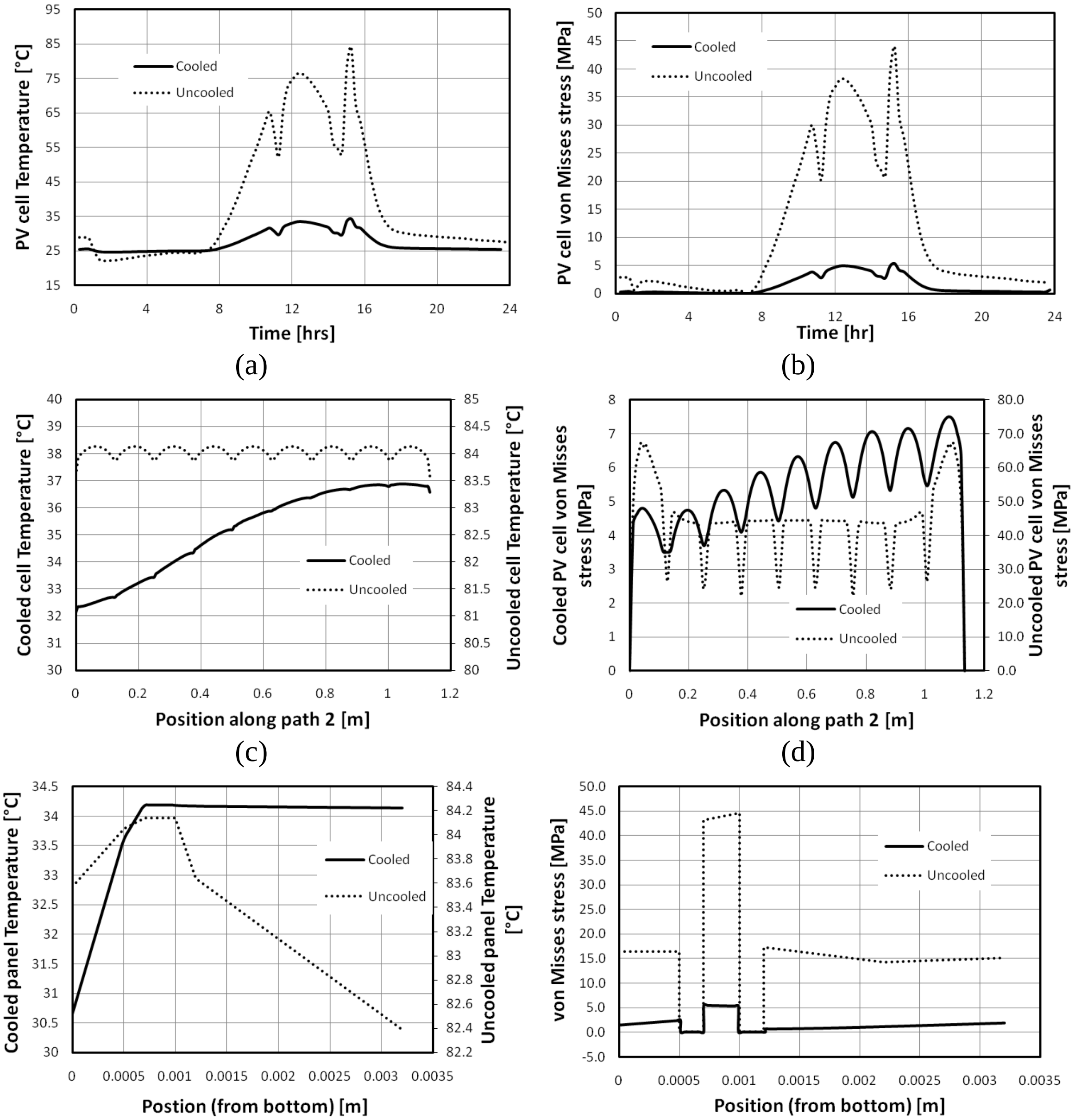

(a) (b)

(c) (d)

(e) (f)

Fig. 7.11. Temporal and spatial variation of temperature and stress in PV panel for October 15, 2000.

The temporal and spatial variation of temperature and stress for December 10, 2000 is shown in Fig. 7.12. Fig. 7.12(a) and Fig. 7.12(b) show the temporal variation of temperature and stress in PV cells. For this day, the panel without cooling showed lower cell temperature through most part of the day. This is because the inlet water temperature for the heat exchanger cooling the PV panel was set to 25°C throughout the day. The maximum PV cell temperature occurred was 29°C at 12:00 pm while the maximum stress was 5.5MPa for the panel without cooling. For cooled panel, the maximum temperature was 25.5°C and the maximum stress was 0.7MPa. Fig. 7.12(c) and Fig. 7.12(d) show the variation of temperature and stress along path P2. The PV cell temperature for uncooled panel was around 29°C while the increase in the PV cell temperature for the cooled panel was less than 1°C along the path. The PV cell von Mises stress away from the boundary, in the uncooled panel was 3MPa. The maximum stress for the cooled panel varied between 0.2MPa and 0.6MPa. Fig. 7.12(e) and Fig. 7.12(f) show the variation of temperature and stress across the thickness at point T1.

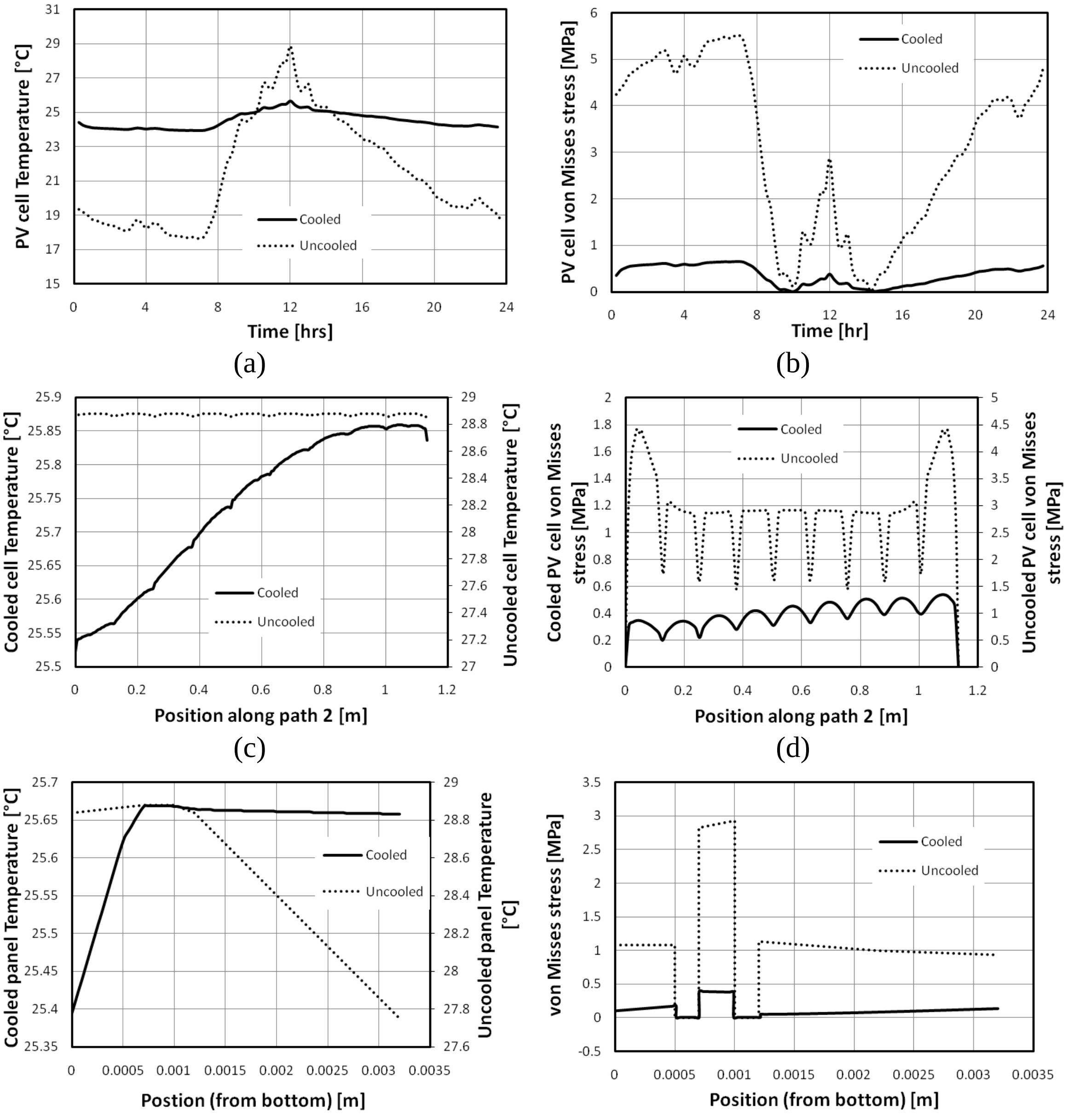

(a) (b)

(c) (d)

(e) (f)

Fig. 7.12. Temporal and spatial variation of temperature and stress in PV panel for December 10, 2000.

Using the measured irradiance and the average predicted PV cell temperature, the electrical performance of a crystalline silicon module (AstroPower AP-110) with and without cooling was simulated for the conditions of the four days considered in this study. The electrical power output of the PV module for the four days is shown in Fig. 7.13 and the variation of electrical efficiency is shown in Fig. 7.14. For the three days (January 17, 2000, July 17, 2000 and October 15, 2000) in which the difference between the PV cell temperature of panel with and without cooling was high, there is marked improved in the electrical performance of the PV panel as shown by Fig. 7.13(a), Fig. 7.13(b) and Fig. 7.13(c). For December 10, 2000, the maximum difference in PV cell temperatures of panels with and without cooling at any time during the day was 6°C. Within this temperature difference range, the electrical performance of the PV panel shows no appreciable variation.

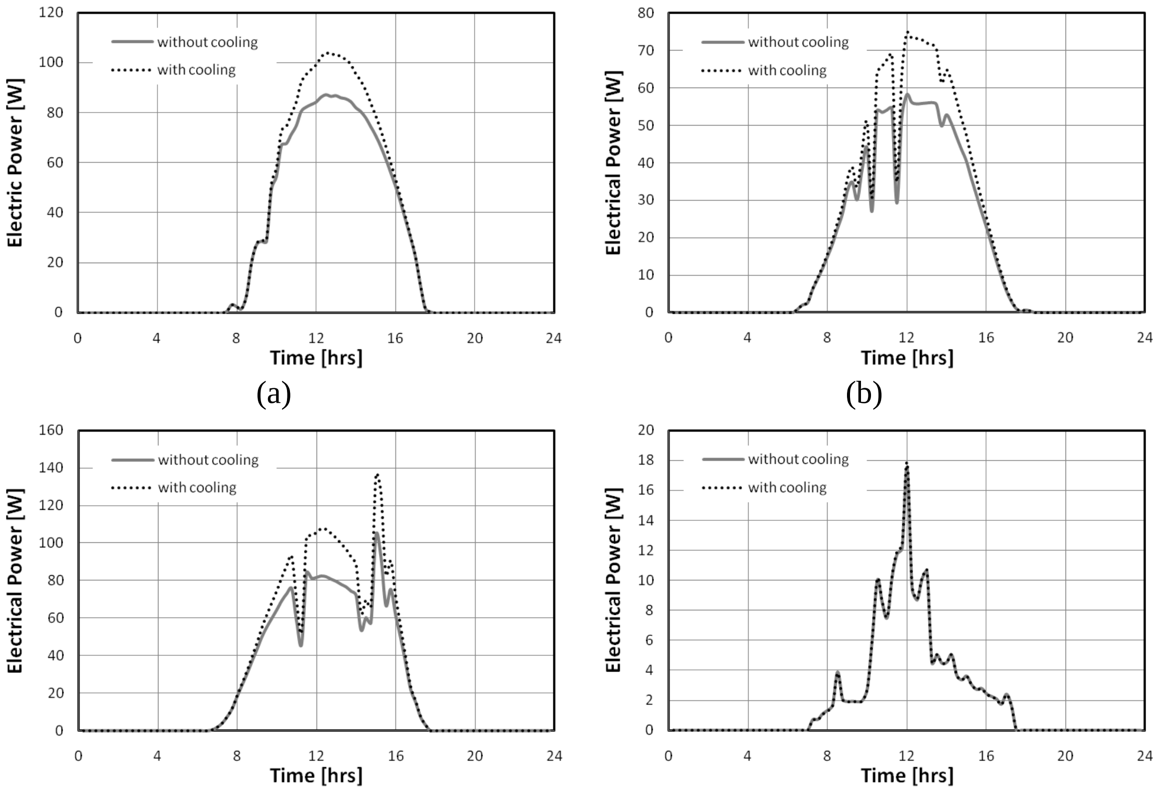

(a) (b)

(c) (d)

Fig. 7.13. Variation of electrical power with time in PV panel with cooling for (a) January 17, (b) July 17, (c) October 15 and (d) December 10

Fig. 7.14 shows variation of electrical efficiency with time during the four days considered in this study. As expected, the cooled PV panels showed higher efficiencies than the panels without cooling for the three days with higher difference between cooled and uncooled cell temperatures (January 17, 2000, July 17, 2000 and October 15, 2000) as shown in Fig. 7.14(a), Fig. 7.14(b) and Fig. 7.14(c). For December 10, 2000, the two panels show same efficiency throughout the day.

Fig. 7.14 also sheds light on the dependence of electrical efficiency upon irradiance and cell temperature. In general, increasing irradiance increases efficiency while increasing PV cell temperature decreases it. At low irradiance, the influence of irradiance is higher but as the cell temperature increases, the positive effect of increasing irradiance decreases until eventually the efficiency starts to drop with increasing cell temperature. This phenomenon is visible in Fig. 7.14(a), Fig. 7.14(b) and Fig. 7.14(c). During morning and evening, the efficiency increased with increasing irradiance. During the peak sunshine hours, the panel with cooling showed slight decrease in efficiency despite the increasing irradiance while the efficiency of the cooled panel completely followed the trend of irradiance.

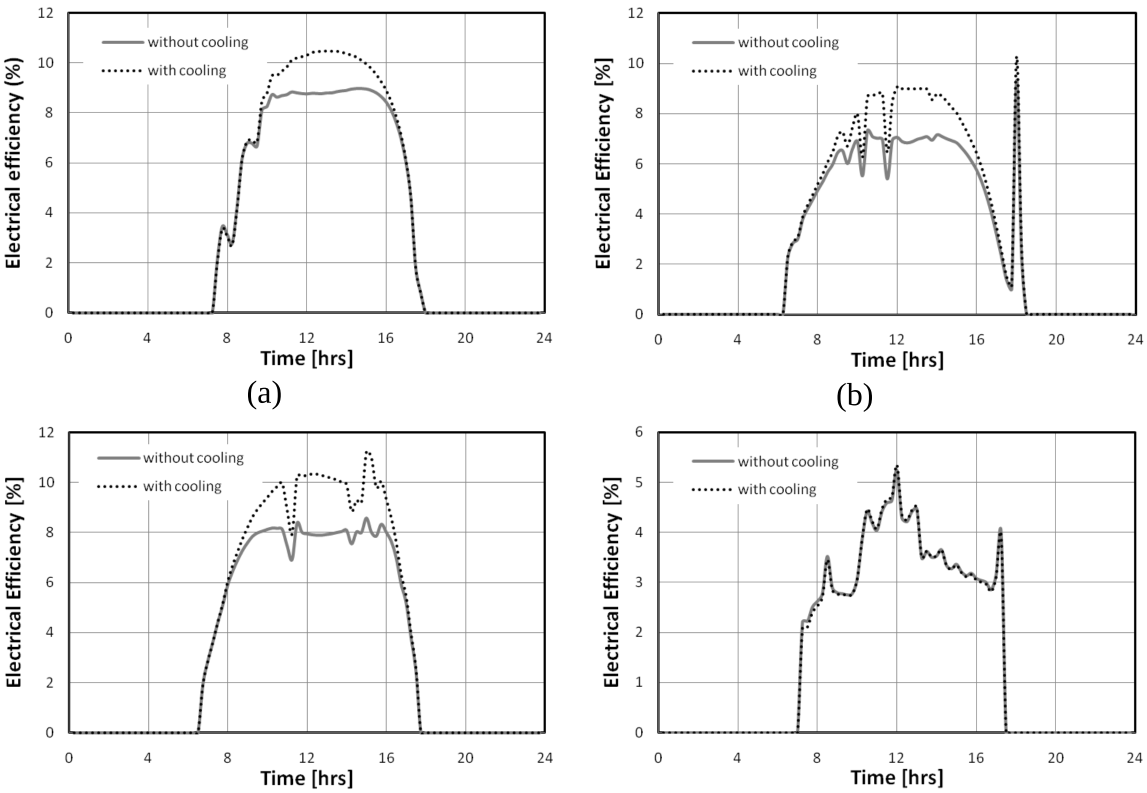

(a) (b)

(c) (d)

Fig. 7.14. Variation of electrical efficiency with time in PV panel with cooling for (a) January 17, (b) July 17, (c) October 15 and (d) December 10

7.2.2 Conclusions

In this study conducted, the developed multiphysics model for PV performance prediction was used to simulate the thermal, structural and electrical performance of a PV module under different types of atmospheric conditions. From the study, the following conclusions were drawn.

- Structural Aspects:
    - The time variation of stress shows the strong dependence of stress cycling on the meteorological conditions.
    - The stress magnitudes for cooled PV panel are one order of magnitude lower than those for panel without cooling.
    - Strong stress gradients are seen in the plane of the PV panel as well as across the thickness of the panel.
- Electrical Aspects:
    - The effectiveness of cooling in improving the electrical conversion efficiency is more strongly dependent on irradiance than ambient temperature.
    - In the future, there is a possibility to use the modeling methodology presented here to develop simple correlations to decide correct heat exchanger operating conditions as a function of irradiance, ambient temperature, wind speed, etc.

CHAPTER 8

AUXILIARY THERMAL COLLECTOR DESIGN FOR PHOTOVOLTAIC PANEL COOLING

8.1 INTRODUCTION

Cooling of Photovoltaic (PV) panels is important when solar concentration is being used or when the ambient temperatures are very high to ensure that the PV cells operate at high efficiencies and do not develop structural defects due to high thermal stresses and large stress cycles during day-to-day operation. The attached heat exchanger also serves the additional purpose of collecting thermal energy in the form of hot water which increases the overall energy collection efficiency of the system. A number of studies have been done to combine the photovoltaic panel with flat plate solar thermal collector into a single collector called the photovoltaic/thermal (PV/T) collector. These include studies in which off-the-shelf PV panels were cooled by heat exchangers and studies in which custom-made PV/T collectors specially designed for thermal energy collection along with electricity generation were developed. Teo et al. [38] designed and developed an air cooled PV/T system using a commercially available PV panel and a custom made air collector and found that the electrical efficiency of the PV panel was increased from 8.6% to 12.5% when the panel was cooled. Huang et al. [41] presented the design of a water-type PV/T collector called the Integrated PhotoVoltaic Thermal System (IPVTS) and did experimental study to measure its performance. In the present work, the approach used was to use a commercially available PV module and combine it with a heat exchanger that is attached to its back.

During the course of this work, it was observed that large temperature gradients develop in PV modules that are being cooled due to non-uniform flow within the heat exchanger. These temperatures gradients can lead to degradation of electrical performance due to cell-mismatch losses. Mismatched cells that are connected together in series do not perform at their individual maximum power point simultaneously; instead, the cells perform at a lesser, collective maximum, which is limited as a result of the mismatch within the module [73]. The temperature gradients also translate into stress gradients being developed in the module which may lead to reliability issues. Moreover, PV panels are usually mounted in a sloped configuration which further increases the temperature gradient. To solve the problem of high temperature gradients, the design of a heat exchanger for cooling PV modules was optimized to reduce the temperature gradient. The results of this work are presented in this chapter.

8.2 PERFORMANCE METRICS

In order to compare the various heat exchangers designs, some quantifiable performance metric were required. Alvarado et al. [74], in a study to compare flow patterns in micro-channel heat exchangers, presented several performance metrics for comparing heat exchangers. These included metric for comparing the thermal performance of the heat exchanger as well as uniformity of flow among the channels. Since the objective of the current work was to design heat exchanger for cooling commercially available PV panels, from an end-user point of view only the thermal characteristics were important. Therefore, the thermal characteristics of the various heat exchanger designs were compared by comparing the following three metrics.

8.2.1 Average surface temperature

The average temperature on the heat exchanger surface ($\bar{T}_s$) determines the average PV cell temperature that directly affects the characteristics of a PV module. Higher PV cell temperatures deteriorate PV electrical performance. Therefore, lower values of $\bar{T}_s$ are desirable. The average surface temperature was calculated using Eq. (8.1).

$$\bar{T}_s = \frac{1}{A}\int_A T_s dA \tag{8.1}$$

8.2.2 Surface Temperature Non-Uniformity

As was mentioned before, temperature gradients in PV modules are undesirable because of the adverse effects on the electrical and structural performance of the modules. Therefore, designs with lower values of surface temperature non-uniformity that is the difference between the maximum and minimum surface temperatures were considered better. Eq. (8.2) gives the surface temperature non-uniformity.

$$\Delta T_s = T_{s,\max} - T_{s,\min} \tag{8.2}$$

8.2.3 Heat Transfer per unit Pumping Power

The heat transfer per unit pumping power is ratio of the energy gained by the working fluid inside the heat exchanger to the pumping power required to operate the heat exchanger. The pumping power required is dependent on the flow rate of the working fluid and the pressure drop in the heat exchanger and is given by Eq. (8.3). Eq. (8.4) is used to calculate the energy gained by the working fluid and Eq. (8.5) gives the heat transfer per unit pumping power.

$$\dot{W}_{pump} = \frac{\dot{m}}{\rho} \Delta P \tag{8.3}$$

$$\dot{Q} = \dot{m} C_p (T_{f,out} - T_{f,in}) \tag{8.4}$$

$$\frac{\dot{Q}}{\dot{W}_{pump}} = \frac{\rho C_p \left(T_{f,out} - T_{f,in} \right)}{\Delta P} \tag{8.5}$$

8.3 BASIC HEAT EXCHANGER CONFIRUATION CONSIDERED

Before the design optimization task was carried out, the size and the basic configuration of the heat exchanger were selected. The heat exchanger was assumed to consist of two thin flat plates between which thin walls formed the flow channel layout. The thickness of the flat plates and the walls was assumed to be 5mm. The selected dimensions of the heat exchanger were such that it would be able to fit inside the frame of an Astro Power AP-110 module. The module was assumed to be mounted at an angle of 40° which resulted in the effect of buoyancy becoming important. The flow was assumed to enter from the right corner of the higher edge of the heat exchanger. A heat flux of 1000 W/m^2 was applied to the top surface of the heat exchanger.

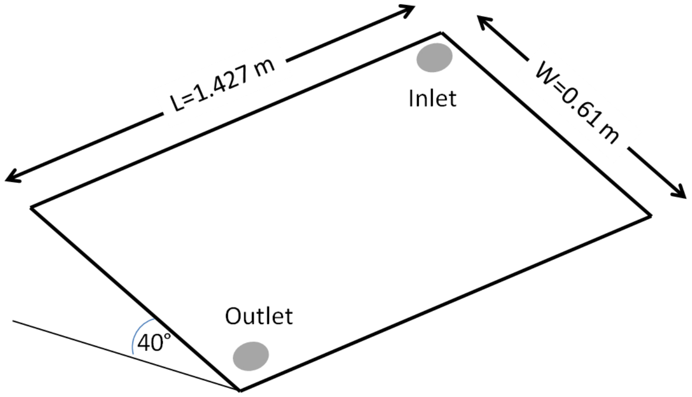

Fig. 8.1. Basic configuration of the heat exchanger

8.4 EFFECT OF VARIATION OF DESIGN PARAMETERS

To see the effect of variation of the heat exchanger design parameters and to optimize its design, a basic ten parallel channel layout was designed. All later modifications to the design were then compared with it. The geometry of the ten parallel channels layout is shown in Fig 8.2. The width of the header was kept equal to the pitch of the channels in the base design.

The parameters that were changed included the number of channels, width of the header, taper in the channel layout and positions of the inlet and outlet. Series-parallel combination channel layouts were also tested. In all the simulations, the inlet velocity of water was set to be 0.3 m/s which resulted in an inlet Reynolds number of around 6500 and turbulent flow. The following sections discuss the effects of various design changes that were made to the basic ten parallel channels design.

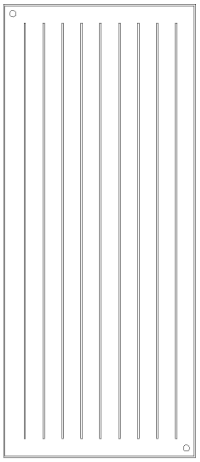

Fig 8.2. Channel Layout for Ten Parallel Channel Heat Exchanger

8.4.1 Effect of number of channels

The first parameter that was changed in the basic layout was the number of channels. Keeping size of the heat exchanger, width of the header and the position of the inlet and the outlet same, the number of channels were increased to twenty. A comparison of the two cases is shown in Fig. 8.3. The temperature contour plots in Fig. 8.3 show very similar temperature distribution on the heat exchanger surface for the ten and twenty channel layouts. The velocity vector plots show that most of the flow goes through the first and the last few channels while the middle channels show very little flow. The average surface temperature, $\overline{T}_s$, of the 10 channels and 20 channels layouts was 302.1K and 302K respectively. The surface temperature non-uniformity, ΔT_s, was 7.3K and 7.4K respectively while the heat transfer rate per unit pumping power, $\dot{Q}/\dot{W}_{pupm}$, was 21241.89 and 21389.47 respectively.

8.4.2 Effect of width of header

The width of the inlet header was doubled for both the ten and twenty parallel channels layouts. The results are shown in Fig. 8.4. As a result of the increase in header width, the flow through the middle channels increased thus decreasing the maximum temperature. The average surface temperature, $\overline{T}_s$, of the 10 channels and 20 channels layouts with wider header was 301.3 K and 301.6 K, respectively. The surface temperature non-uniformity, ΔT_s, was 5.1K and 6.3K while the heat transfer rate per unit pumping power, $\dot{Q}/\dot{W}_{pupm}$, was 38339.45 and 36840.74, respectively.

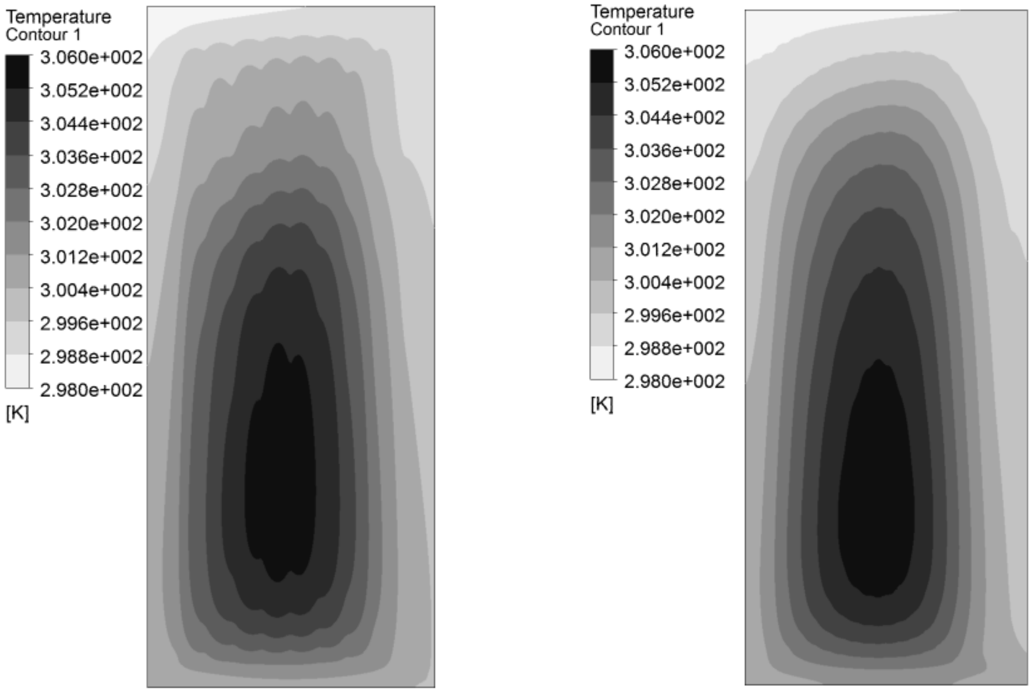

10 Channels Temperature Contour Plot 20 Channels Temperature Contour Plot

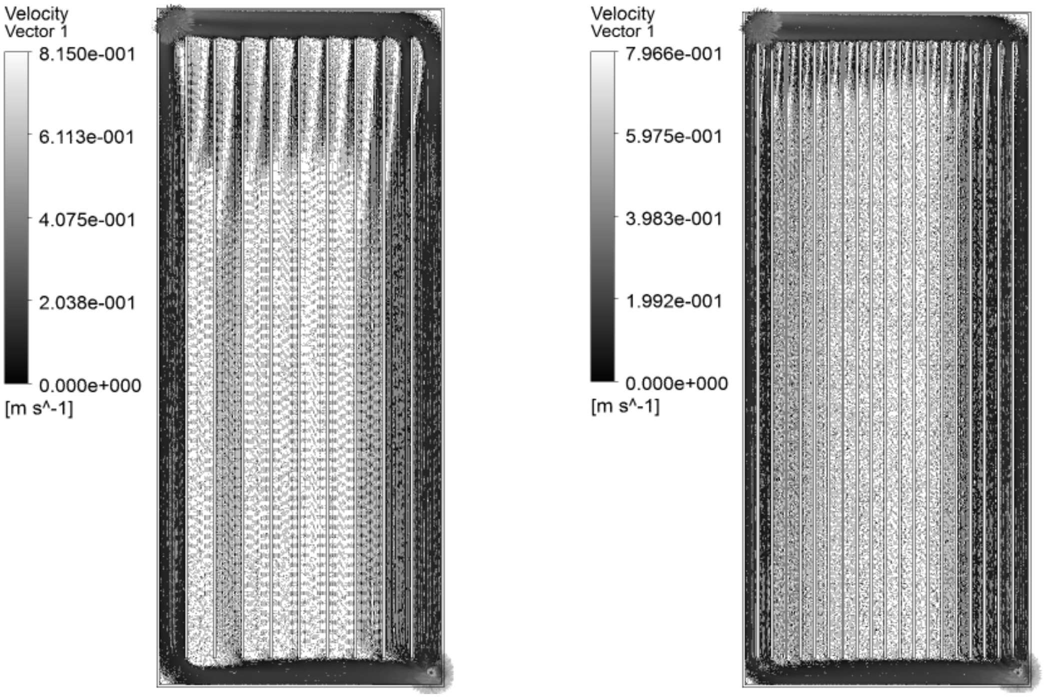

10 Channels Velocity Vector Plot 20 Channels Velocity Vector Plot

Fig. 8.3. Effect of Number of Channels

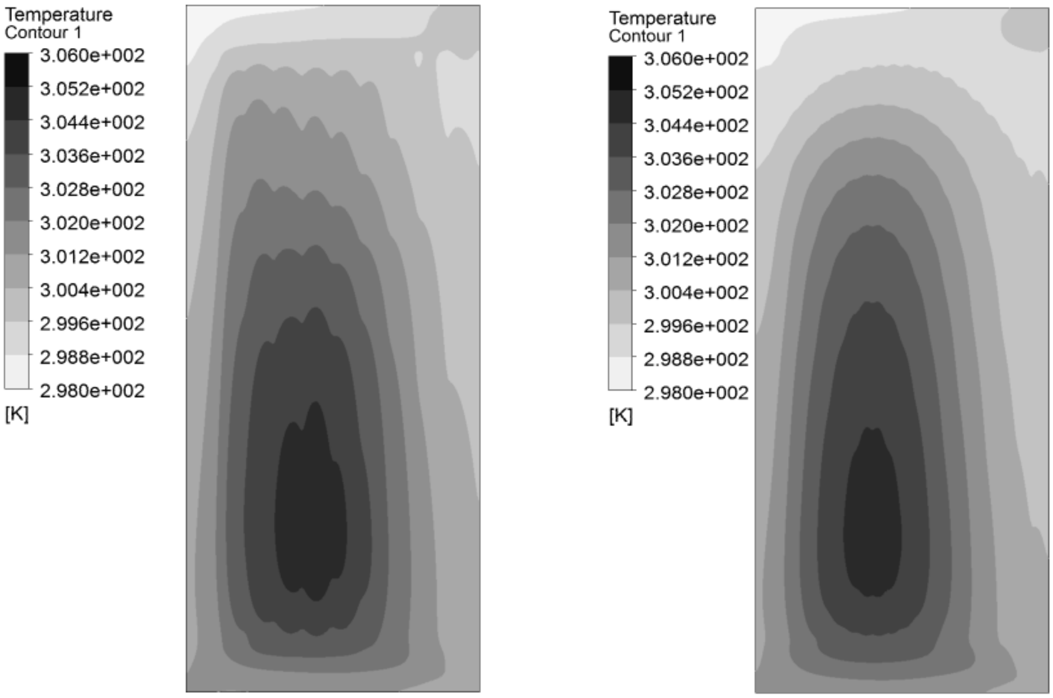

10 Channels (Wider Header) Temperature Contour Plot

20 Channels (Wider Header) Temperature Contour Plot

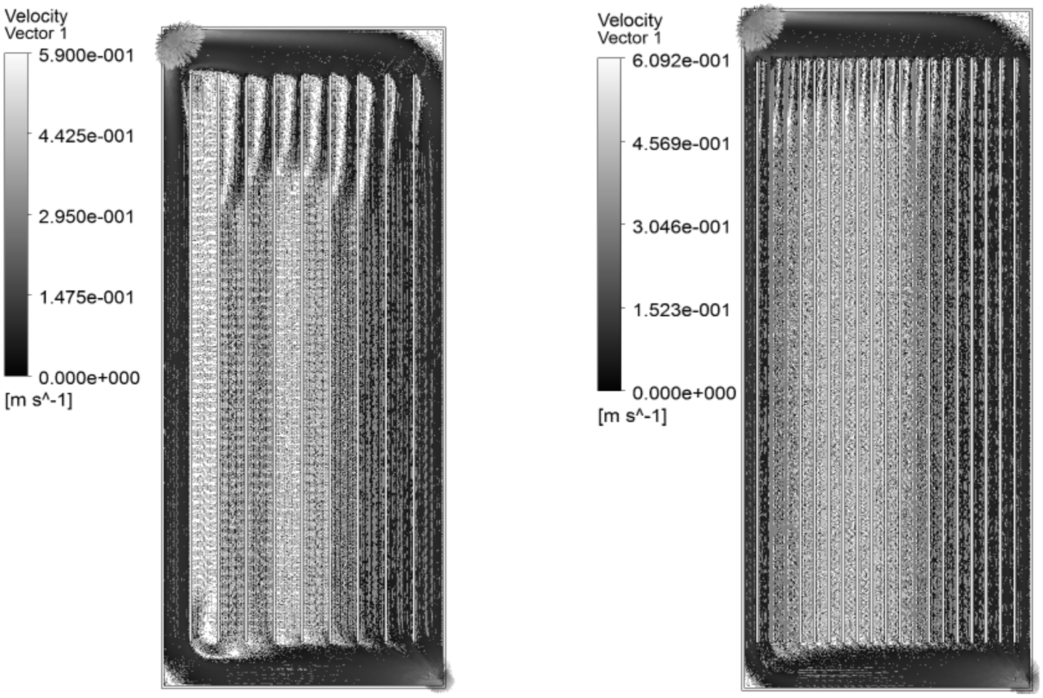

10 Channels (Wider Header) Velocity Vector Plot

20 Channels (Wider Header) Velocity Vector Plot

Fig. 8.4. Effect of Width of Header

8.4.3 Effect of tapered arrangement of channels

From the results shown in Fig. 8.3 and Fig. 8.4, it was observed that the water inside the header region finds no obstruction that can make it turn into the middle channels and therefore most of the water flow through the final channel. To enhance the uniformity of flow in all channels and thus improve the thermal performance of the heat exchanger, the channels were arranged in a tapered arrangement with the header width wider near to the inlet and narrowed down towards last of the channels. In total six tapered channels designs were tried with an objective to improve the uniformity of surface temperature. In the first design, the minimum and maximum widths of the header were equal to the pitch of the channels and twice of the pitch of the channels respectively. In the second design, the maximum width of the header was increased to two and a half times the pitch. The results showed that the average surface temperatures, $\bar{T}_s$, of the two tapered designs were both 302K, the surface temperature non-uniformity, ΔT_s, was 7.2K for both the case while the heat transfer rate per unit pumping power, $\dot{Q}/\dot{W}_{pupm}$, was 24440.26 and 24748.05, respectively. Therefore, the tapered section designs provided no significant performance improvement on their own.

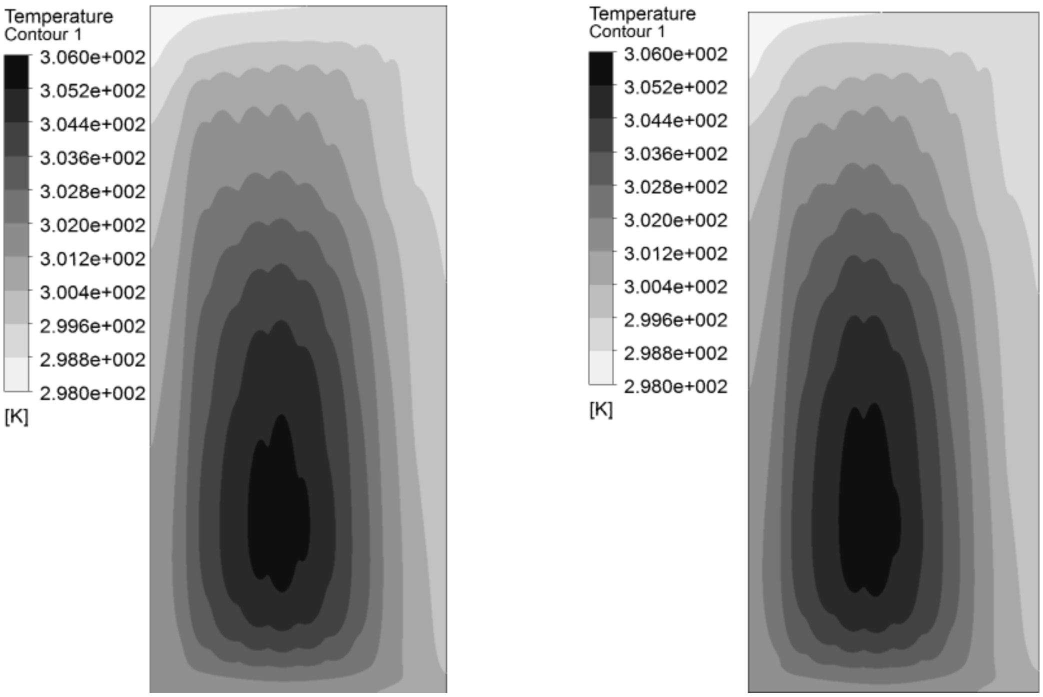

Tapered Channels Design 1 Temperature Contour Plot

Tapered Channels Design 2 Temperature Contour Plot

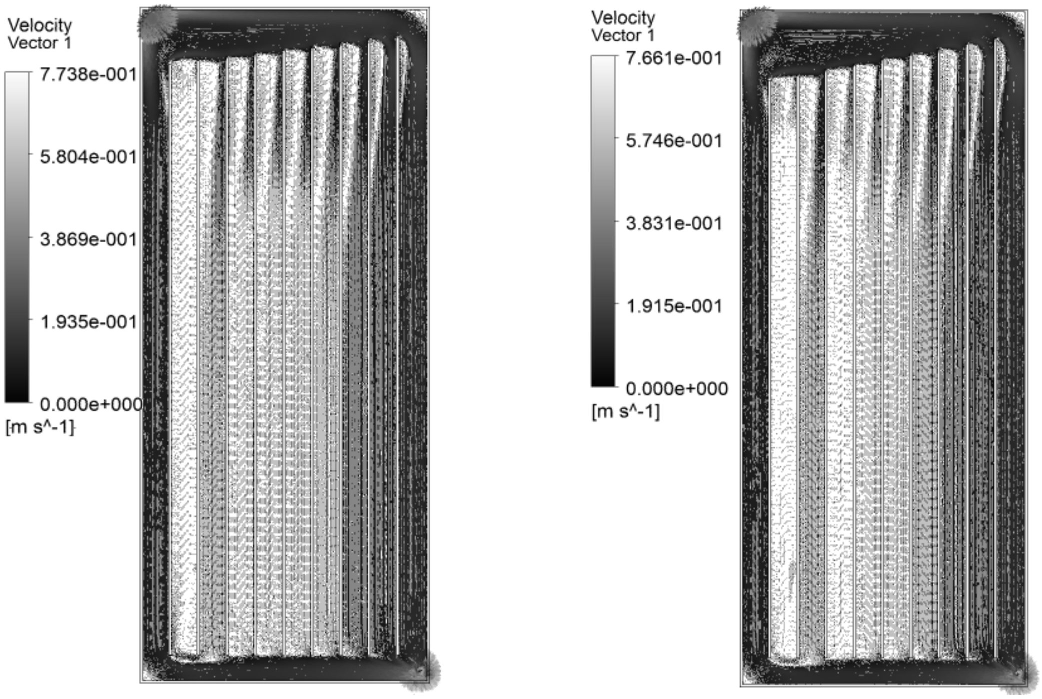

Tapered Channels Design 1 Velocity Vector Plot

Tapered Channels Design 2 Velocity Vector Plot

Fig. 8.5. Effect of Tapered Channel Arrangement (Designs 1 and 2)

8.4.4 Effect of position of inlet and outlet

In the layouts with tapered channel arrangements, the position of inlet as well as outlet were moved to study the effect it had on the flow and temperature distribution. The tapered channels design 2 was modified and the inlet was moved 8cm away from the side wall (to the left side in figure) and 5cm towards the channels (moved up in the figure). The results are shown in Fig. 8.6. The overall temperatures on the top surface were reduced but as the velocity vector plot shows, the flow in the middle channels was still very low. The results showed that the average surface temperatures, $\bar{T}_s$, was 301.9K, the surface temperature non-uniformity, ΔT_s, was 6.4K and the heat transfer rate per unit pumping power, $\dot{Q}/\dot{W}_{pump}$, was 27430.87. Therefore, compared to tapered channels designs 1 and 2, there was improvement in design 3 by moving the inlet.

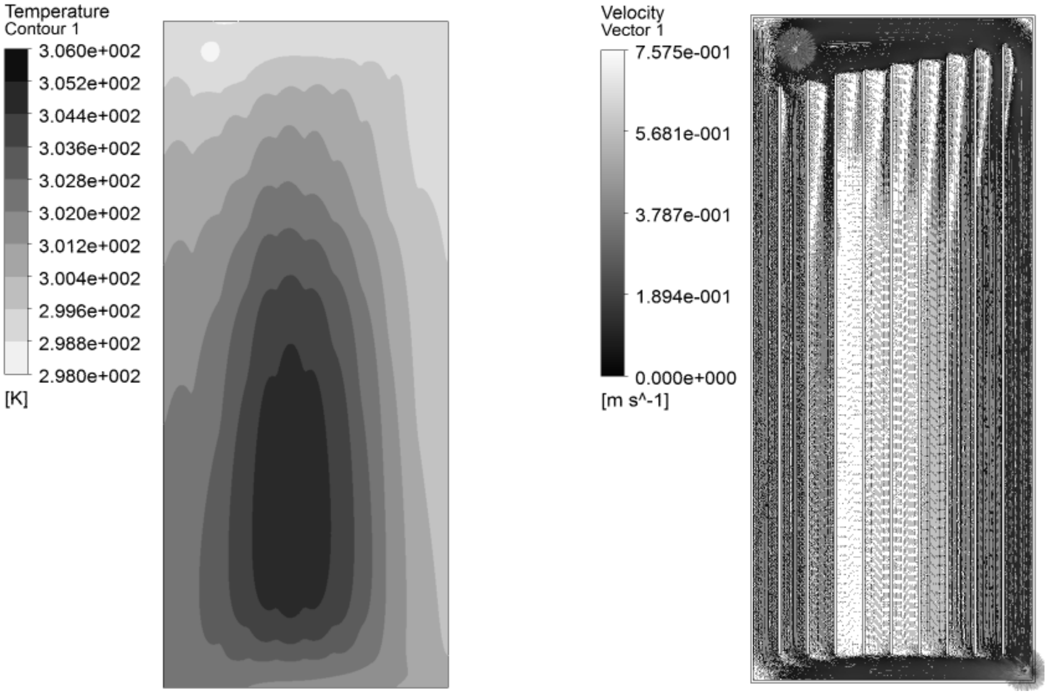

Tapered Channels Design 3 Temperature Contour Plot

Tapered Channels Design 3 Velocity Vector Plot

Fig. 8.6. Effect of Inlet and outlet position (Tapered Channel Arrangement Designs 3)

To further improve the performance, further modifications to the tapered channels designs were made in three iterations. First, in tapered channels design 4, the header sizes were increased. On the inlet side, header was varied between 15cm and 30cm and on the outlet side, the header was 15cm. Next, in tapered channels design 5, the header on the outlet side was tapered with a minimum thickness of 5cm and a maximum of 20cm to decrease the maximum temperature of design 4. Finally, the inlet and outlet were moved to a position 15 cm from the sides in tapered channels design 6. The outlet was moved to increase the resistance to flow for the water that passed through the final channel thus reducing the flow through it. The results showed that the average surface temperatures, $\bar{T}_s$, of the final tapered layout, design 6, was 301.4K, the surface temperature non-uniformity, ΔT_s, was 4.8K while the heat transfer rate per unit pumping power, $\dot{Q}/\dot{W}_{pupm}$, was 54923.33. All three performance metrics for tapered channels design 6 showed significant performance improvement over all other designs considered. Fig. 8.7 and Fig. 8.8 show the results for tapered channels designs 4, 5 and 6.

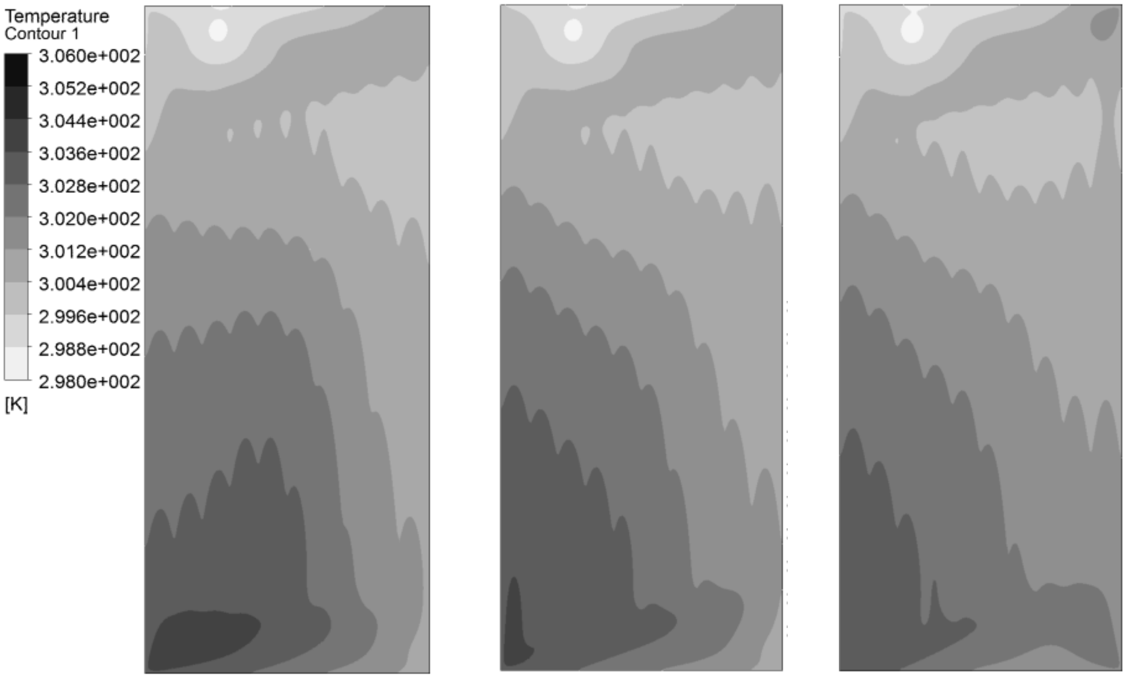

Tapered Design 4 Tapered Design 5 Tapered Design 6

Fig. 8.7. Temperature Contour Plots for Tapered Channels Designs 4, 5 and 6

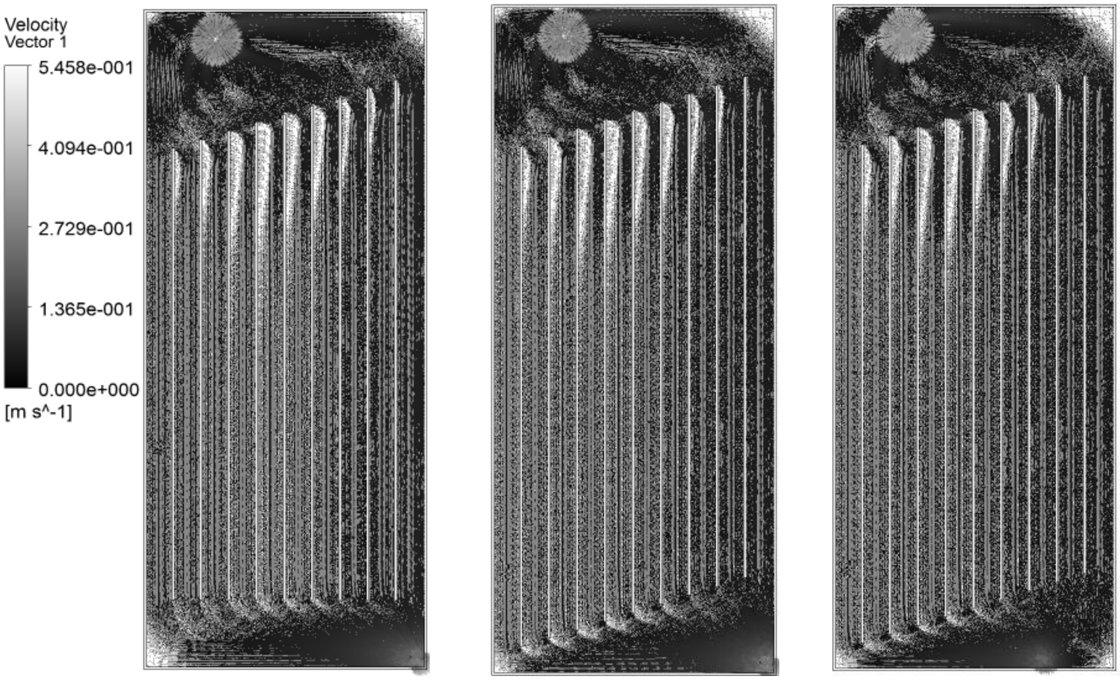

Tapered Design 4 Tapered Design 5 Tapered Design 6

Fig. 8.8. Velocity Vector Plots for Tapered Channels Designs 4, 5 and 6

Another approach that was tried by varying the position of the inlet and outlet was to place both the inlet and the outlet at middle of the heat exchanger width. First, a design was tried with no taper and inlet and outlet width of 20cm. The results for this design are presented in Fig. 8.9. The results for first center-to-center design showed that the average surface temperatures, $\overline{T}_s$, was 301.5K, the surface temperature non-uniformity, ΔT_s, was 5.4K while the heat transfer rate per unit pumping power, $\dot{Q}/\dot{W}_{pupm}$, was 58124.44.

Fig. 8.9 shows that the water going to the outlet did not flow through the entire header on the outlet side and therefore, temperatures there were higher. To reduce the gradient occurring on the outlet side header, the width of the outlet side header was reduced to 15cm. The results are shown in Fig. 8.10. With the new outlet header width, the average surface temperatures, $\overline{T}_s$, remained the same at 301.5K, the surface temperature non-uniformity, ΔT_s, decreased to 5.1K while the heat transfer rate per unit pumping power, $\dot{Q}/\dot{W}_{pupm}$, showed little variation and was 58234.39.

Finally, to further reduce the higher temperatures at the corners of the outlet side header, the outlet side header was tapered from both sides with a minimum header width of 10cm towards both corners and a maximum width of 20cm at the center. The results are shown in Fig. 8.11. These changes resulted in the average surface temperatures, $\overline{T}_s$, to remain the same at 301.5K, the surface temperature non-uniformity, ΔT_s, to decrease to 4.7K while the heat transfer rate per unit pumping power, $\dot{Q}/\dot{W}_{pupm}$, showed slight decrease to 57942.12.

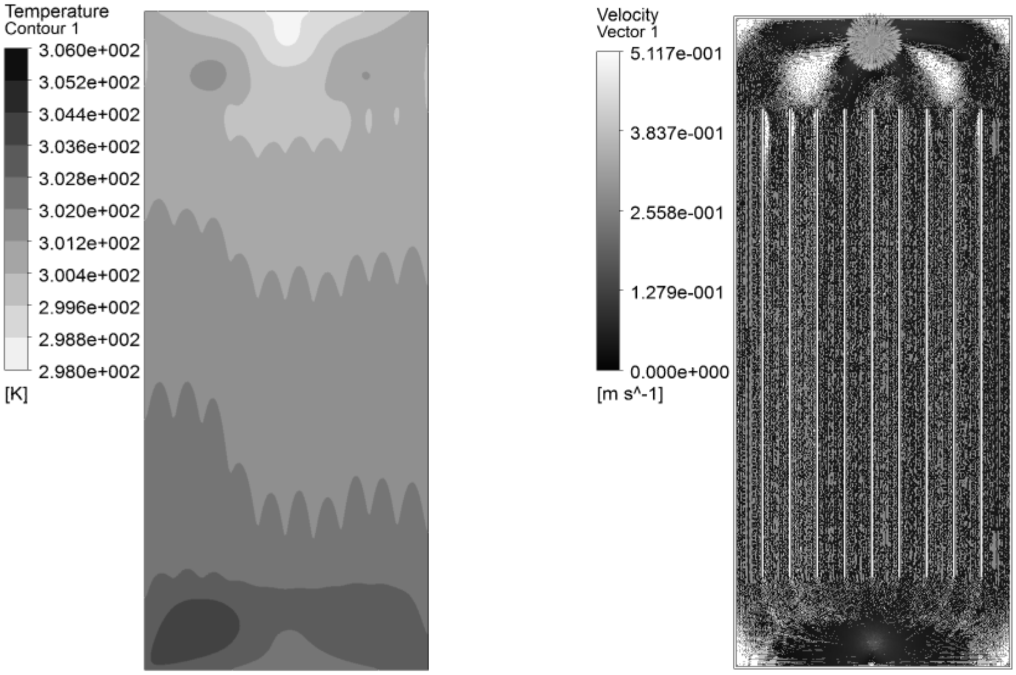

Center-to-Center Design 1 Temperature Contour Plot Center-to-Center Design 1 Velocity Vector Plot

Fig. 8.9. Results for Center-to-Center Design 1

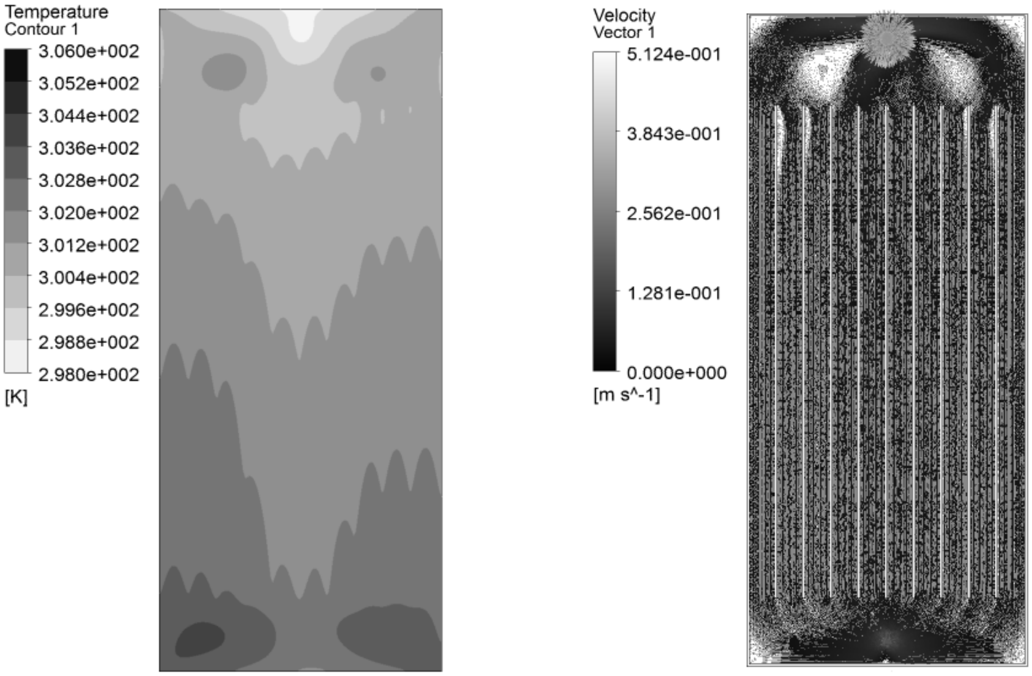

Center-to-Center Design 2 Temperature Contour Plot Center-to-Center Design 2 Velocity Vector Plot

Fig. 8.10. Results for Center-to-Center Design 2

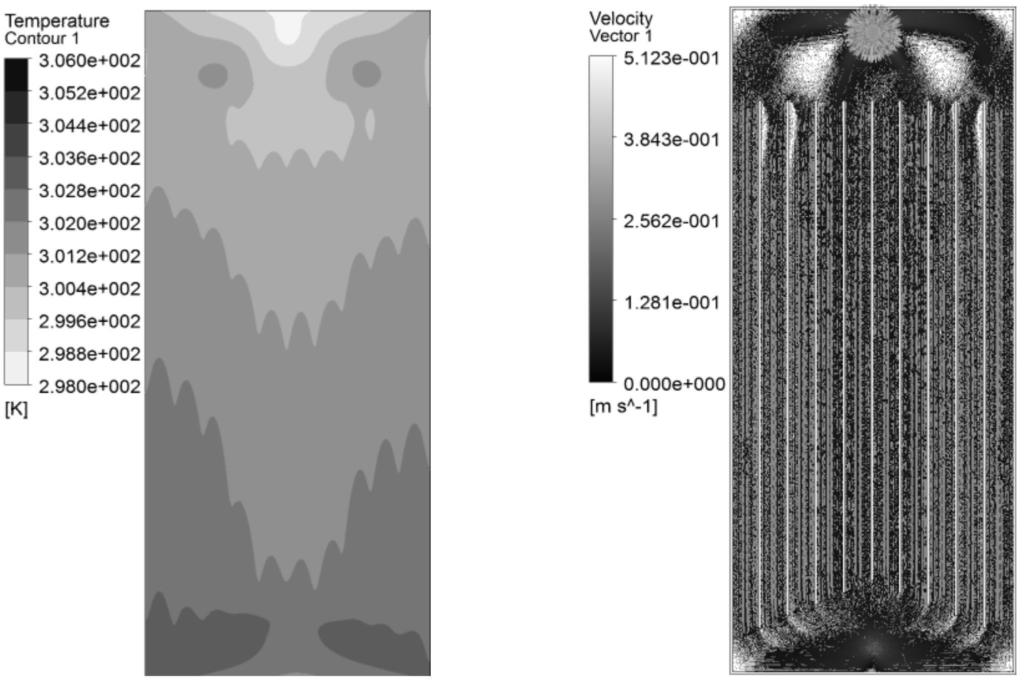

Center-to-Center Design 2 Temperature Contour Plot

Center-to-Center Design 2 Velocity Vector Plot

Fig. 8.11. Results for Center-to-Center Design 3

8.4.5 Effect of Series-Parallel Combinations

A different way to distribute flow inside a heat exchanger is to connect the channels in series. Such layouts ensure that all channels receive high and equal flow rate which increases turbulence which in turn improves the heat transfer. The downside of using series layouts is the high pumping power required due to the pressure drop in the heat exchanger. One way to decrease the pressure drop is to use series-parallel combinations which still ensure better flow distribution than parallel channels. In this study, two series-parallel layouts were simulated. One had two 5 channels series connected in parallel while the other had two 9 channels series connected in parallel. The results for both these layouts are shown in Fig. 8.12. The results showed that the average surface temperatures, $\bar{T}_s$, were 299.8K and 299.5K respectively which were the lowest among all designs considered. Similarly, the surface temperature non-uniformity, ΔT_s, for the 10 channels and 18 channels series-parallel layouts were 2.2K and 1.8K which were again the lowest of all designs. The main problem with the series parallel designs was the high pressure drop which resulted in very low values for the heat transfer rate per unit pumping power, $\dot{Q}/\dot{W}_{pupm}$, which was 10270.18 and 1836.91, respectively.

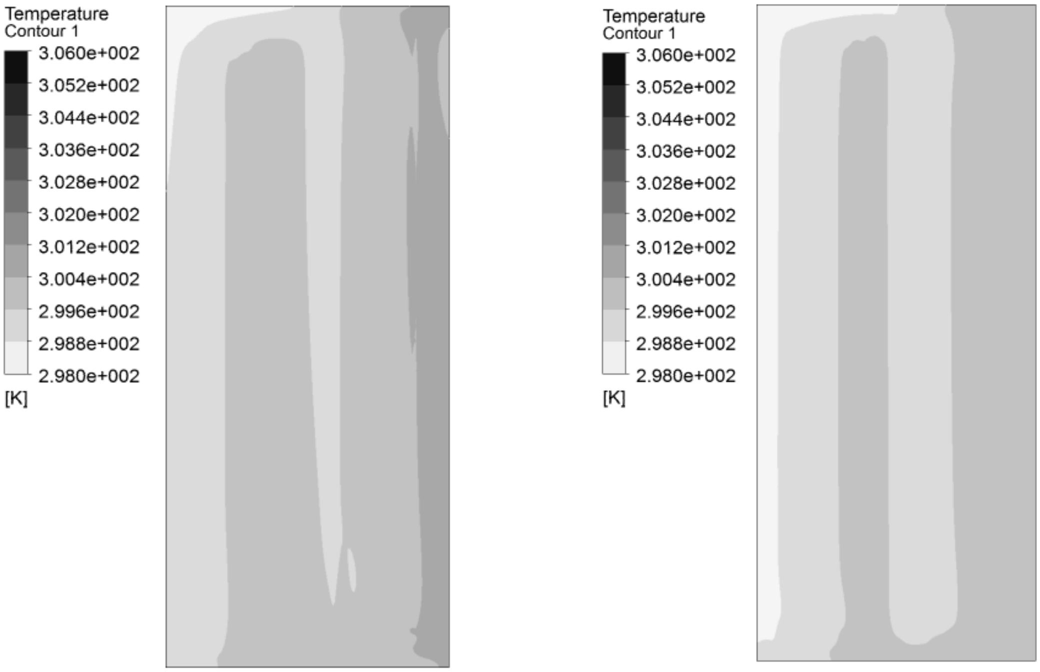

10 Channels Series-Parallel Layout Temperature Contour Plot

18 Channels Series-Parallel Layout Temperature Contour Plot

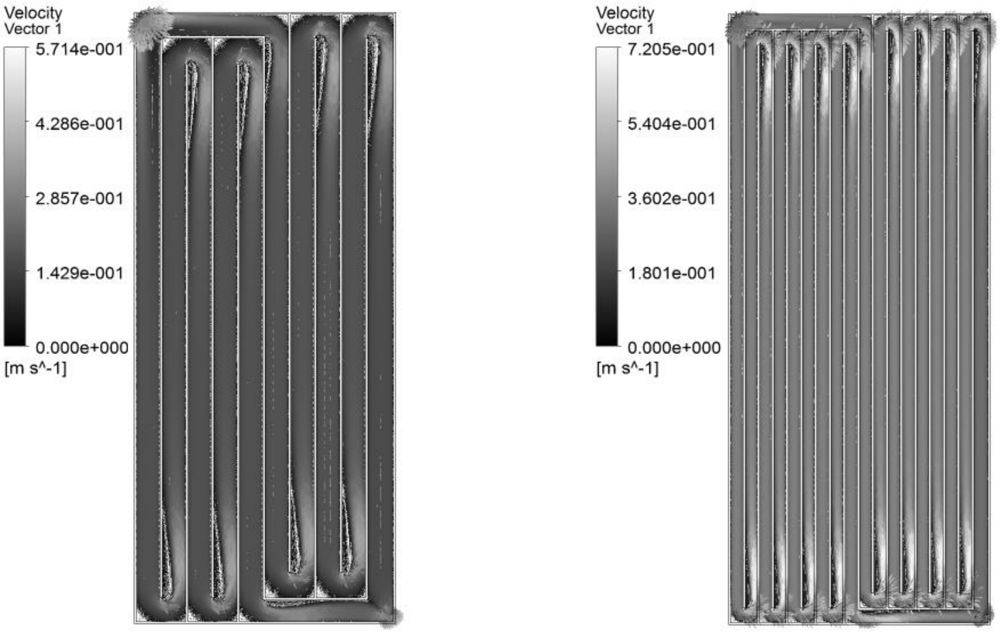

10 Channels Series-Parallel Layout Velocity Vector Plot

18 Channels Series-Parallel Layout Velocity Vector Plot

Fig. 8.12. Results for Series-Parallel Combination Layouts

8.5 SUMMARY OF RESULTS

In total fifteen channel layout designs were simulated. These included modifications to the number of channels, width of the header, positions of the inlet and outlet and positioning of the channel walls. Among all the modifications considered, the width of the header proved to be the most important. Wider headers on the inlet side resulted in better distribution of the flow among the channels as shown in Fig. 8.8 for tapered channels designs 4, 5 and 6 as well as Figs. 8.9-8.11 for the center-to-center designs. Wider headers also resulted in lower pressure drop which improved the heat transfer per unit pumping power for the heat exchanger.

The positioning of the inlet and outlet also proved to be important in controlling the amount of fluid that entered the middle channels. When the inlet and outlet were placed at corners as in ten and twenty parallel channels designs with and without wider headers and tapered channels design 1 and 2, almost the entire flow moved through the first and last channels. Fig. 8.13 shows the average channel velocities for the ten parallel channels layouts with and without wider headers. As can be seen from the figure, the flow through the first and the last channels was significantly more than through the middle channels. The effect of moving the inlet is shown in Fig. 8.14 which shows the average channel flow velocities for the tapered channel arrangements 2 and 3. These two layouts had the exact same design except the position of the inlet which was moved inward in tapered arrangement 3. The figure shows that when the inlet is moved inward, the flow in the middle channels is increased.

Varying the channel walls lengths to form a tapered arrangement of channels did not provide significant improvement to the thermal performance on its own. But it proved to be useful for refining the flow distribution after using modifications like variation of header width and inlet and outlet positioning. This was used in centered-inlet-and-outlet design 3, shown in Fig. 8.11, in which channel wall lengths were tapered on the outlet header side to reduce the temperature gradient there. Similarly when tapered arrangement was used together with header width and inlet and outlet position variation in tapered channel arrangement 6, shown in Fig. 8.7 and Fig. 8.8, the resulting layout design showed good thermal performance. The average channel velocity distributions for the centered-inlet-and-outlet layout 3 and tapered channel layout 6 are shown in Fig. 8.15.

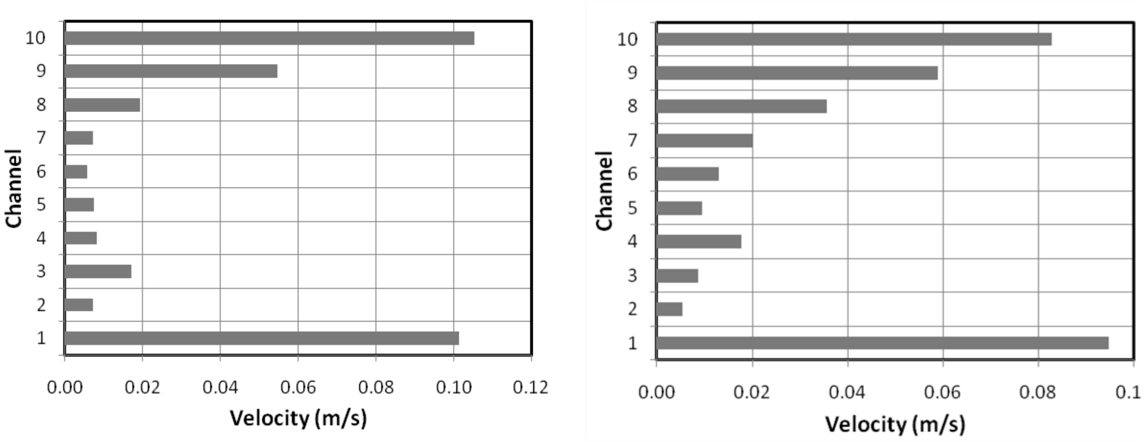

10 Parallel Channels Layout

10 Parallel Channels Layout with Wider Headers

Fig. 8.13 Average channel flow velocities for Ten Parallel Channels Layout with and without wider headers

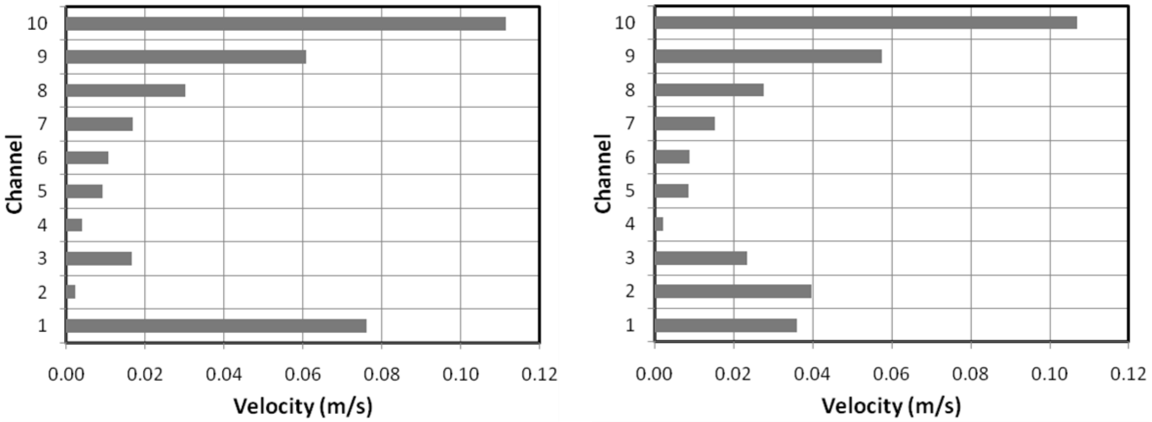

Tapered Channel Arrangement 2 Tapered Channel Arrangement 3

Fig. 8.14 Average channel flow velocities for Tapered Channel Arrangement 2 and 3

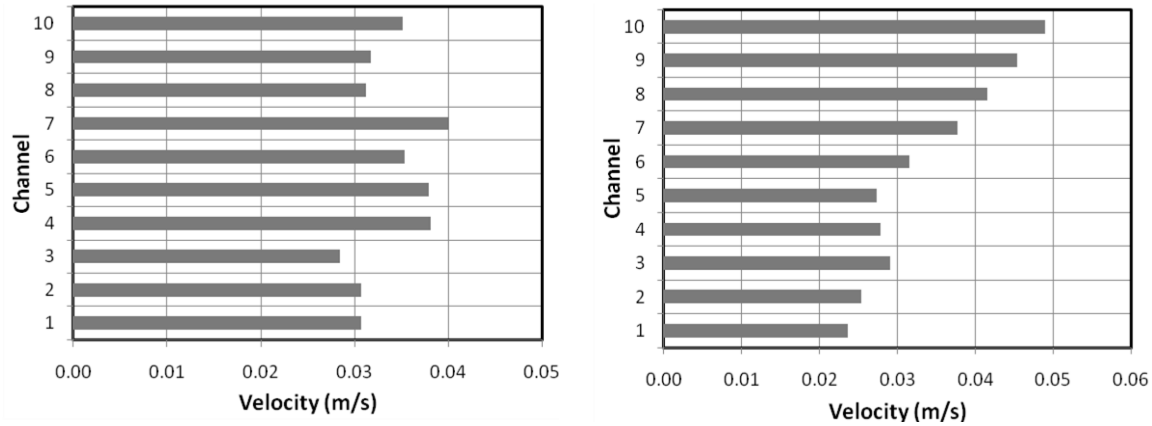

Centered-Inlet-and-Outlet layout 3 Tapered Channel Arrangement 6

Fig. 8.15 Average channel flow velocities for Centered-Inlet-and-Outlet layout 3 and Tapered Channel Arrangement 6

A summary of the simulation results for the fifteen layout designs considered is shown in Table 8.1. The average surface temperature, $\bar{T}_s$, varied from 299.5K and 302.1K between the fifteen designs. This small variation will not cause significant variation in the electrical performance of PV systems. The surface temperature non-uniformity, ΔT_s, showed a variation from 1.8K to 7.4K while the heat transfer per unit pumping power varied from 1836.91 to 58234.39. To compare all the layouts, the surface temperature non-uniformity and heat transfer per unit pumping power were plotted and are shown in Fig. 8.16. The figure shows that designs 8 and 10 to 13 showed both low surface temperature non-uniformity and high heat transfer per unit pumping power. These designs were tapered channel arrangements 4 and 6 and the three centered-inlet-and-outlet layouts.

Table 8.1. Summary of Heat Exchanger Layout Design Simulation Results

No.	**Channel Type**	**Number of Channels**	**$T_{f,out}$ (K)**	**$T_{s,avg}$ (K)**	**$T_{s,max}$ (K)**	**$T_{s,min}$ (K)**	**Pr. Drop (Pa)**	**ΔT_s (K)**	$\frac{\dot{Q}}{\dot{W}_{pump}}$
1	Parallel	10	300.1	302.1	305.7	298.4	434.8	7.30	21241.89
2	Parallel	20	300.1	302.0	305.8	298.4	431.8	7.40	21389.47
3	Wider header	10	300.2	301.3	303.5	298.4	240.9	5.10	38339.45
4	Wider header	20	300.1	301.6	304.7	298.4	250.7	6.30	36840.74
5	Tapered Channels 1	10	300.1	302.0	305.6	298.4	377.9	7.20	24440.26
6	Tapered Channels 2	10	300.1	302.0	305.6	298.4	373.2	7.20	24748.05
7	Tapered Channels 3	10	300.1	301.9	305.1	298.7	336.7	6.40	27430.87
8	Tapered Channels 4	10	300.2	301.5	304.0	298.7	178.1	5.30	51858.36
9	Tapered Channels 5	10	300.2	301.7	304.1	298.6	358.2	5.50	25784.40
10	Tapered Channels 6	10	300.2	301.4	303.5	298.7	168.1	4.80	54943.33
11	Centered Inlet and outlet 1	10	300.2	301.5	304.0	298.6	158.9	5.40	58124.44
12	Centered Inlet and outlet 2	10	300.2	301.5	303.7	298.6	158.6	5.10	58234.39
13	Centered Inlet and outlet 3	10	300.2	301.5	303.3	298.6	159.4	4.70	57942.12
14	Series-Parallel	10	300.1	299.8	300.6	298.4	899.3	2.20	10270.18
15	Series-Parallel	18	300.2	299.5	300.2	298.4	5028.0	1.80	1836.91

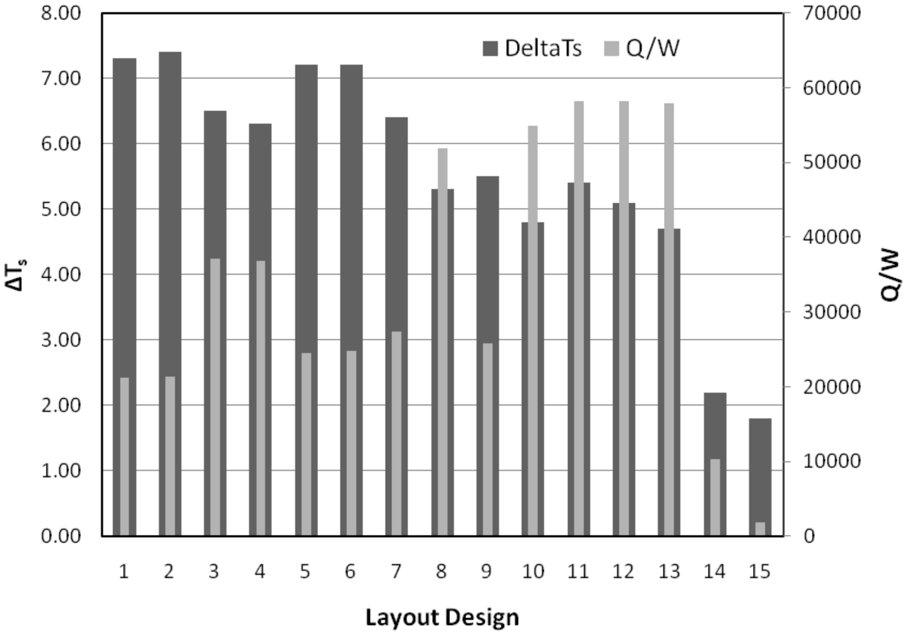

Fig. 8.16 Comparison of surface temperature non-uniformity and heat transfer per unit pumping power for the simulated design layouts

8.6 SELECTION OF BEST CHANNEL LAYOUT DESIGNS BASED ON PERFORMANCE METRICS

To select the best layout designs, the three performance metrics, average surface temperature, surface temperature non-uniformity and heat transfer per unit pumping power, were used. In the first step, five designs with the highest average temperature were discarded. The best ten layout designs sorted according to average surface temperature are listed in Table 8.2. Next, the five designs with lowest values of heat transfer per unit pumping power were discarded. The remaining five are tabulated in Table 8.3 in descending order of heat transfer per unit pumping power. Finally, the two designs with the lowest value of surface temperature non-uniformity, Centered Inlet and Outlet layout 3 and Tapered Channels Layout 6, were selected. Their simulation results summary is tabulated in Table 8.4 and the two layout designs are shown in Fig. 8.17. The two designs showed almost same values of average surface temperature and surface temperature non-uniformity. The heat transfer per unit pumping power of the center-to-center design was around 5.5% better than the tapered channels design. The flow distribution in the two designs is shown in Fig. 8.15.

Table 8.2. Best Ten Layout Designs according to Average Surface Temperature

No.	**Channel Type**	**Number of Channels**	**$T_{f,out}$ (K)**	**$T_{s,avg}$ (K)**	**$T_{s,max}$ (K)**	**$T_{s,min}$ (K)**	**Pr. Drop (Pa)**	**ΔT_s (K)**	$\frac{\dot{Q}}{\dot{W}_{pump}}$
1	Series-Parallel	18	300.1	299.5	300.2	298.4	5028.0	1.80	1836.91
2	Series-Parallel	10	300.2	299.8	300.6	298.4	899.3	2.20	10270.18
3	Tapered Channels 6	10	300.2	301.4	303.5	298.7	168.1	4.80	54943.33
4	Tapered Channels 4	10	300.2	301.5	304.0	298.7	178.1	5.30	51858.36
5	Centered Inlet and outlet 1	10	300.2	301.5	304.0	298.6	158.9	5.40	58124.44
6	Centered Inlet and outlet 2	10	300.2	301.5	303.7	298.6	158.6	5.10	58234.39
7	Centered Inlet and outlet 3	10	300.2	301.5	303.3	298.6	159.4	4.70	57942.12
8	Wider header	20	300.1	301.6	304.7	298.4	250.7	6.30	36840.74
9	Wider header	10	300.0	301.7	304.9	298.4	248.6	6.50	37151.95
10	Tapered Channels 5	10	300.2	301.7	304.1	298.6	358.2	5.50	25784.40

Table 8.3. Best Five Layout Designs according to Heat Transfer per Unit Pumping Power

No.	Channel Type	Number of Channels	$T_{f,out}$ (K)	$T_{s,avg}$ (K)	$T_{s,max}$ (K)	$T_{s,min}$ (K)	Pr. Drop (Pa)	ΔT_s (K)	$\frac{\dot{Q}}{\dot{W}_{pump}}$
1	Centered Inlet and outlet 2	10	300.2	301.5	303.7	298.6	158.6	5.10	58234.39
2	Centered Inlet and outlet 1	10	300.2	301.5	304.0	298.6	158.9	5.40	58124.44
3	Centered Inlet and outlet 3	10	300.2	301.5	303.3	298.6	159.4	4.70	57942.12
4	Tapered Channels 6	10	300.2	301.4	303.5	298.7	168.1	4.80	54943.33
5	Tapered Channels 4	10	300.2	301.5	304.0	298.7	178.1	5.30	51858.36

Table 8.4. Best Two Layout Designs according to Surface Temperature Non-Uniformity

No.	Channel Type	Number of Channels	$T_{f,out}$ (K)	$T_{s,avg}$ (K)	$T_{s,max}$ (K)	$T_{s,min}$ (K)	Pr. Drop (Pa)	ΔT_s (K)	$\frac{\dot{Q}}{\dot{W}_{pump}}$
1	Centered Inlet and outlet 3	10	300.2	301.5	303.3	298.6	159.4	4.70	57942.12
2	Tapered Channels 6	10	300.2	301.4	303.5	298.7	168.1	4.80	54943.33

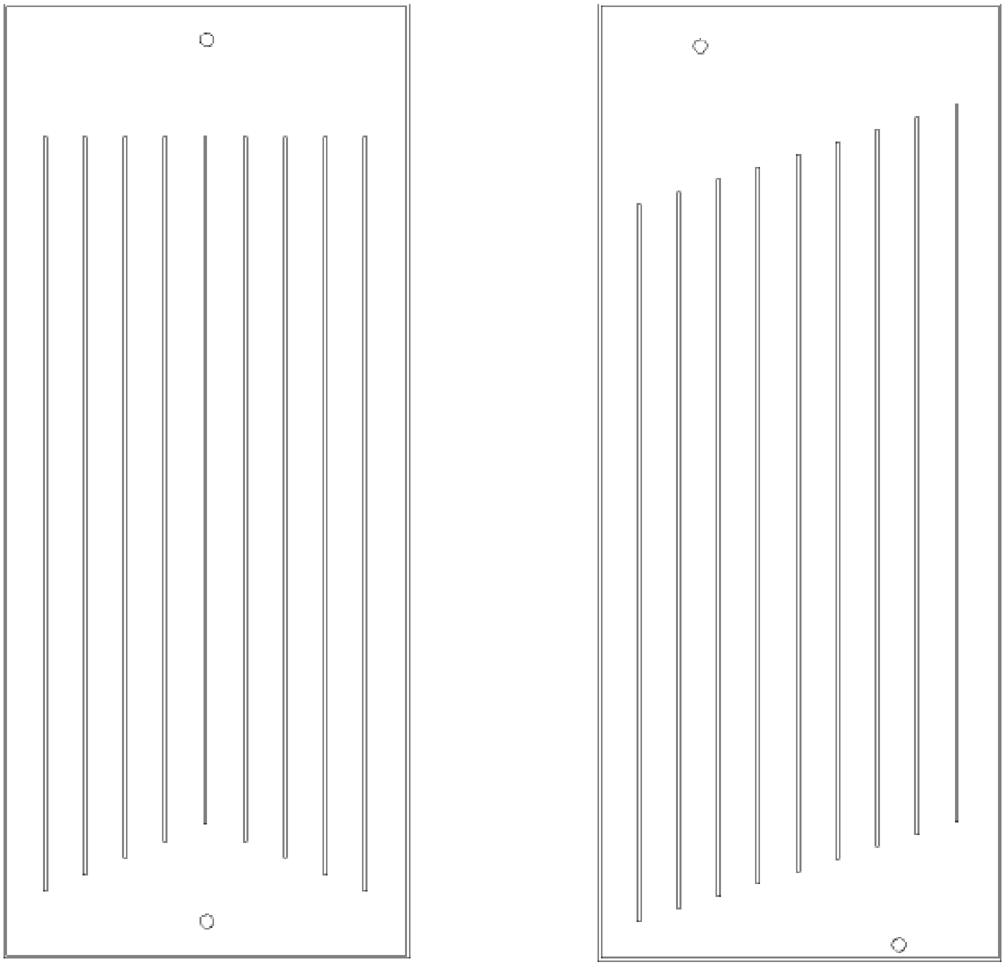

Centered Inlet and Outlet Layout 3

Tapered Channels layout 6

Fig. 8.17. Selected Heat Exchanger Channel Layout Designs

8.7 CONCLUSIONS

In this chapter, the process of optimizing the channel layout design of a heat exchanger for cooling PV panels was presented. Several design modifications were made to a basic ten parallel channels layout to study which of the changes provided improvements in the performance of the heat exchanger as measured by the considered performance metrics. From the work presented in this chapter, the following conclusions were drawn.

- Change in the number of channels did not cause any appreciable change in the thermal performance of the heat exchanger. In the series-parallel arrangements, increase in the number of channels from 10 to 18 resulted in the pressure drop to increase from 899.3 Pa to 5028 Pa without any significant improvement in performance.
- Width of the header proved to be the most crucial design parameter. In general, it was found that wider inlet header improved flow distribution. Though, too wide headers on the outlet side resulted in stagnation towards the corners which increased the temperature gradient.
- Tapered positioning of the channels proved useful in sending flows to channels and regions where it previously was not going. Tapered channels layouts provided best results with wide inlet headers.

- The positioning of the inlet and the outlet is also critical to ensure that sufficient quantity of flow enters the middle channels. Moving the inlet and outlet towards the center resulted in more flow entering the middle channels.
- From this work, it is proposed that the approach that should be used in designing channel layouts is to first vary the inlet and outlet headers until a reasonable temperature distribution is achieved. After this, tapers should be applied to the channel sizes to *fine-tune* this temperature distribution.

CHAPTER 9

CONCLUSIONS AND RECOMMENDATIONS

A detailed multi-physics model to predict the performance of photovoltaic modules was developed in this work. A novel electrical model was proposed and validated and three-dimensional thermal and structural models capable of calculating the temperature and stress distributions in the PV panel were developed. Various studies were conducted using this developed model from which the following conclusions are drawn:

- A sensitivity analysis carried out to study the influence of the five model parameters on the output of the electrical model showed that the model is several orders of magnitude more sensitive to the parameters I_L and a than the remaining three parameters.
- In the study conducted to see the effect of PV cell technology of developed electrical model accuracy and its comparison with the accuracy of other models, the proposed seven parameter model showed improvement in the prediction accuracy for modules of all PV cell type considered in the study. Among the other models, Sandia Labs model showed the best results.

- In the future, there is a need to test the proposed seven parameter model with experimental data to further validate its accuracy.
- From the comparative study of the effect of the selected radiation model on the accuracy of the electrical model showed that the minimum bias is shown by the HDKR model and the maximum bias is shown by the Isotropic model. When the objective is system design, Isotropic model is the most suitable choice because of its conservative nature. For system studies, HDKR model is the most suitable choice because its prediction is the closest to actual value. Additional, an attempt to improve accuracy by the inclusion of an additional set of reference parameters at lower reference irradiance in the electrical model showed no improvement. Instead, it resulted in more conservative predictions.
- Within the absorbed radiation range of 400-3000 W/m2 at an ambient temperature of 25°C, PV panel with cooling maintains its efficiency (9.5-10.5%) with almost linearly increasing electrical power from 50W to 300W. Whereas, for the same range, efficiency reduces from 10% to 4% for panel without any cooling.
- The parametric study to see the effect of changing atmospheric and operating conditions showed that the electrical performance of the PV panel with cooling remained almost constant independent of the changing atmospheric conditions. It was observed that the effect of cooling is more pronounced in hot environments like Saudi Arabia having high solar irradiance and ambient temperature.
- The effectiveness of cooling in reducing the thermal stress in the module was found to increase as the solar radiation or the ambient temperature increases. This

implies that cooling is more effective in areas like the Middle East which have high solar resource and hot environments.

- From the transient analysis carried out it was found that there is a strong dependence of stress cycling on the meteorological conditions. Also, it was found that the effectiveness of cooling in improving the electrical conversion efficiency is more strongly dependent on irradiance than ambient temperature.
- In the future, there is a possibility to use the modeling methodology presented here to develop simple correlations to decide correct heat exchanger operating conditions as a function of irradiance, ambient temperature, wind speed, etc.
- In the work done on designing of heat exchanger for PV panel cooling, it was found that the width of the header and tapered arrangement of channels were important parameters in modifying the overall thermal performance of the heat exchanger.

NOMENCLATURE

a	Modified diode ideality factor (V)
A	Diode ideality factor
A_i	Anisotropy index
A_{panel}	Area of PV panel (m^2)
AM	Air mass
AOI	Angle of incidence
$[B]$	Dispalcement gradient matrix
C_p	Specific heat capacity (J/kg.K)
C_μ, $C_{\varepsilon 1}$, $C_{\varepsilon 2}$	Constants for turbulence model
$[D]$	Material properties matrix (Pa)
E	Irradiance (W/m^2)
E_g	Band-gap energy of PV cell material (eV)
FF	Fill factor
f_d	Fraction of diffuse radiation absorbed in the module
$\{F^{th}\}$	Thermal force vector (N)
G	Total horizontal radiation (W/m^2)
G_o	Extraterrestrial radiation (W/m^2)
G_b	Horizontal beam radiation (W/m^2)
G_d	Horizontal diffuse radiation (W/m^2)
G_{ref}	Reference condition (STC) incident radiation (W/m^2)
h	Heat loss coefficient (W/m^2.K)
I	PV module output current (A)
I_L	Light current (A)
I_o	Diode reverse saturation current (A)
$[K]$	Stiffness matrix (N/m)
k	Boltzmann's constant, 1.38066E-23 (J/K)
k	Thermal conductivity (W/m.K)

k	Turbulent kinetic energy (m^2/s^2)
K	Extinction coefficient
$K_{\tau\alpha,b}$	Incidence angle modifier for beam radiation
$K_{\tau\alpha,d}$	Incidence angle modifier for diffuse radiation
$K_{\tau\alpha,g}$	Incidence angle modifier for ground reflected radiation
L_{glass}	Thickness of front glass layer (m)
m	Irradiance dependence parameter for I_L
M	Air mass modifier
n	Temperature dependence parameter for a
n	Surface normal
NCS	Number of cells in series in a module's cell-string
N_p	Number of cell-strings in parallel in module
N_s	Number of cells in series in a module's cell-string
NSC	Normalized sensitivity coefficient
P	Electrical power (W)
P_k	Production term
q	Heat conduction (W)
q	Elementary charge, $1.60218\text{x}10^{-19}$ (coulomb)
Q	Volumetric heat generation (W/m^3)
$\dot{Q}$	Heat transferred to working fluid in heat exchanger (W)
Q_{vh}	Viscous energy dissipation (W/m^3)
R_{beam}	Geometric factor for beam radiation
R_s	Series resistance (Ω)
R_{sh}	Shunt resistance (Ω)
S	Plane-of-array absorbed solar radiation at operating conditions (W/m^2)
S_{ref}	Absorbed solar radiation at STC (W/m^2)
t	time (s)
T	Temperature (K)
T_{amb}	Ambient temperature (K)
$\bar{T}_s$	Heat exchanger average surface temperature (K)

S	Plane-of-array absorbed solar radiation at operating conditions (W/m^2)
S_{ref}	Absorbed solar radiation at STC (W/m^2)
t	time (s)
$T_{f,in}$	Inlet water temperature (K)
T_s	Panel surface temperature (K)
u	Fluid Velocity (m/s)
$\{u\}$	Displacement vector (m)
V	Voltage (V)
$V_{f,in}$	Inlet water velocity (m/s)
$V_{pv,cell}$	Volume of PV cells inside the module (m^3)
$\dot{W}_{pump}$	Pumping power required for heat exchanger
WS	Wind speed over PV panel (m/s)
$\bar{X}_i$	Nominal value of model parameters in sensitivity analysis
$\bar{Y}$	Nominal value of function in sensitivity analysis

Greek Symbols

α	Coefficient of thermal expansion (K^{-1})
α_{imp}	Temperature coefficient of maximum power point current (A/K)
α_{isc}	Temperature coefficient of short circuit current (A/K)
β	Slope of PV panel
β_{voc}	Temperature coefficient of open circuit voltage (V/K)
β_{vmp}	Temperature coefficient of maximum power point voltage (V/K)
γ	Overall diode ideality factor of PV module
δu	Virtual displacement (m)
$\delta(T_c)$	Thermal voltage per cell at temperature Tc
ΔT_s	Heat exchanger surface non-uniformity (K)
ΔX_i	Change in model parameters in sensitivity analysis
ΔY	Change in $^{\text{function}}$ value due to ΔX_i change in model parameters
η_{pv}	Electrical efficiency of PV panel

ε	Turbulent dissipation rate (m^2/s^3)
$\{\varepsilon\}$	Elastic strain vector
$\{\varepsilon^{th}\}$	Thermal strain vector
$\{\varepsilon_T\}$	Total strain vector
ρ	Reflectivity of ground
ρ	Density (kg/m^3)
θ	Incidence angle of solar radiation
θ_r	Refracted angle of solar radiation
σ	Stefen-Boltzmann's constant
σ_ε	Turbulent Prandtl number for ε
σ_k	Turbulent Prandtl number for k
μ	Dynamic viscosity (Pa.s)
μ_T	Turbulent viscosity (Pa.s)
μ_{Voc}	Temperature coefficient of open circuit voltage (V/K)
μ_{Isc}	Temperature coefficient of short circuit current (A/K)
$(\tau\alpha)_b$	Transmitivity-Absorptivity product for beam radiation
$(\tau\alpha)_d$	Transmitivity-Absorptivity product for beam radiation
$(\tau\alpha)_g$	Transmitivity-Absorptivity product for diffuse radiation
$(\tau\alpha)_n$	Transmitivity-Absorptivity product for ground reflected radiation

Subscripts

0	Reference cell condition
10	Cell temperature 10°C higher than reference
amb	Ambient
b	Beam radiation
c, cell	PV cell
diff	Diffuse radiation
e	Effective radiation; experimental
m	Module back surface; modeled
mp	Maximum power point
oc	Open circuit point

ref	Reference cell condition
sc	Short circuit point
x	IV point at module voltage equal to half of open circuit voltage
xx	IV point at module voltage equal to average of max. power and open circuit voltages

REFERENCES

[1] Soto W. De, Klein S. A., and Beckman W. A., 2006, "Improvement and validation of a model for photovoltaic array performance," Solar Energy, 80(1), pp. 78-88.

[2] King D. L., Boyson W. E., and Kratochvil J. A., 2004, Photovoltaic Array Performance Model, Sandia National Laboratories, Albuquerque,, New Mexico.

[3] Marion B., Rummel S., and Anderberg A., 2004, "Current-voltage curve translation by bilinear interpolation," Progress in Photovoltaics: Research and Applications, 12(8), pp. 593-607.

[4] Jones A. D., and Underwood C. P., 2001, "A thermal model for photovoltaic systems," Solar Energy, 70(4), pp. 349-359.

[5] Acciani G., Falcone O., and Vergura S., 2010, "Analysis of the thermal heating of poly-Si and a-Si photovoltaic cell by means of FEM," International Conference on Renewable Energies and Power Quality.

[6] Armstrong S., and Hurley W. G., 2010, "A thermal model for photovoltaic panels under varying atmospheric conditions," Applied Thermal Engineering, 30(11-12), pp. 1488-1495.

[7] Tina G., 2010, "A Coupled Electrical and Thermal Model for Photovoltaic Modules," Journal of Solar Energy Engineering, 132(2), p. 02450.

[8] Liu B. Y. H., and Jordan R. C., 1961, "Daily insolation on surfaces tilted toward the equator," ASHRAE J., 3(10), pp. 53-59.

[9] Klutcher T. M., 1979, "Evaluation of models to predict insolation on tilted surfaces," Solar Energy, 23, pp. 111-114.

[10] Reindl D. T., Beckman W. A., and Duffie J. A., 1990, "Evaluation of hourly tilted surface radiation models," Solar Energy, 45(1), pp. 9-17.

[11] Perez R., Stewart R., Arbogast C., Seals R., and Scott J., 1986, "An anisotropic hourly diffuse radiation model for sloping surfaces : description , performance validation , site dependency evaluation," Solar Energy, 36(6), pp. 481-497.

[12] Boyd M. T., Klein S. a., Reindl D. T., and Dougherty B. P., 2011, "Evaluation and Validation of Equivalent Circuit Photovoltaic Solar Cell Performance Models," Journal of Solar Energy Engineering, 133(2), p. 021005.

[13] Hay J. E., and Davies J. A., 1980, "Calculation of solar radiation incident on an inclined surface," First Canadian solar radiation data workshop, p. 59.

[14] Sjerps-Koomen E. A., Alsema E. A., and Turkenburg W. C., 1996, "A simple model for PV module reflection losses under field conditions," Solar Energy, 57(6), pp. 421-432.

[15] Cameron C. P., Boyson W. E., and Riley D. M., 2008, "Comparison of PV system performance-model predictions with measured PV system performance," Photovoltaic Specialists Conference, 2008. Conference Record of the Thirty-THird IEEE, pp. 2-7.

[16] Mondol J., Yohanis Y., and Norton B., 2008, "Solar radiation modelling for the simulation of photovoltaic systems," Renewable Energy, 33(5), pp. 1109-1120.

[17] Hishikawa Y., Imura Y., and Oshiro T., 2000, "Irradiance-dependence and translation of the I-V characteristics of crystalline silicon solar cells," Photovoltaic Specialists Conference (PVSC), 2000 28th IEEE, pp. 1464-1467.

[18] Townsend T. U., 1989, "A method for predicting the long-term performance of directly-coupled photovoltaic systems," University of Wisconsin, Madison.

[19] Chenni R., Makhlouf M., Kerbache T., and Bouzid A., 2007, "A detailed modeling method for photovoltaic cells," Energy, 32(9), pp. 1724-1730.

[20] Villalva M. G., Gazoli J. R., and Filho E. R., 2009, "Comprehensive Approach to Modeling and Simulation of Photovoltaic Arrays," IEEE Transactions on Power Electronics, 24(5), pp. 1198-1208.

[21] Valerio L. B., Orioli A., Ciulla G., and Gangi A. D., 2010, "An improved five-parameter model for photovoltaic modules," Solar Energy Materials and Solar Cells, 94(8), pp. 1358-1370.

[22] Merten J., Asensi J. M., Voz C., Shah A. V., Platz R., and Andreu J., 1998, "Improved equivalent circuit and analytical model for amorphous silicon solar cells and modules," Electron Devices, IEEE Transactions on, 45(2), pp. 423-429.

[23] Campbell R. C., 2007, "A Circuit-based Photovoltaic Array Model for Power System Studies," Power Symposium, 2007. NAPS '07. 39th North American, pp. 97-101.

[24] Carrero C., Ramírez D., Rodríguez J., and Platero C. a., 2011, “Accurate and fast convergence method for parameter estimation of PV generators based on three main points of the I–V curve,” Renewable Energy, 36(11), pp. 2972-2977.

[25] Ikegami T., Maezono T., Nakanishi F., Yamagata Y., and Ebihara K., 2001, “Estimation of equivalent circuit parameters of PV module and its application to optimal operation of PV system,” Solar Energy Materials and Solar Cells, 67, pp. 389-395.

[26] Zagrouba M., Sellami A., Bouaïcha M., and Ksouri M., 2010, “Identification of PV solar cells and modules parameters using the genetic algorithms: Application to maximum power extraction,” Solar Energy, 84(5), pp. 860-866.

[27] Chouder A., and Silvestre S., 2009, “Analysis Model of Mismatch Power Losses in PV Systems,” Journal of Solar Energy Engineering, 131(May), pp. 1-5.

[28] Kaushika N., and Rai a, 2007, “An investigation of mismatch losses in solar photovoltaic cell networks,” Energy, 32(5), pp. 755-759.

[29] Karatepe E., Boztepe M., and Colak M., 2007, “Development of a suitable model for characterizing photovoltaic arrays with shaded solar cells,” Solar Energy, 81(8), pp. 977-992.

[30] Patel H., and Agarwal V., 2008, “MATLAB-Based Modeling to Study the Effects of Partial Shading on PV Array Characteristics,” IEEE transactions on energy conversion, 23(1), pp. 302-310.

[31] Grabitz P. O., Rau U., and Werner J. H., 2005, “A multi-diode model for spatially inhomogeneous solar cells,” Thin Solid Films, 487(1-2), pp. 14-18.

[32] Skoplaki E., and Palyvos J. A., 2009, “On the temperature dependence of photovoltaic module electrical performance: A review of efficiency/power correlations,” Solar Energy, 83(5), pp. 614-624.

[33] Notton G., Cristofari C., Mattei M., and Poggi P., 2005, “Modelling of a double-glass photovoltaic module using finite differences,” Applied Thermal Engineering, 25(17-18), pp. 2854-2877.

[34] Tina G. M., and Scrofani S., 2008, “Electrical and Thermal Model for PV Module Temperature Evaluation,” Electrotechnical Conference, 2008. MELECON 2008. The 14th IEEE Mediterranean, pp. 585-590.

[35] Bigot D., Miranville F., Fakra A. H., and Boyer H., 2009, “A nodal thermal model for photovoltaic systems : Impact on building temperature fields and elements of validation for tropical and humid climatic conditions,” Energy and Buildings, 41, pp. 1117-1126.

[36] Skoplaki E., and Palyvos J., 2009, “Operating temperature of photovoltaic modules: A survey of pertinent correlations,” Renewable Energy, 34(1), pp. 23-29.

[37] “SunPower E20 Module Datasheet.”

[38] Teo H. G., Lee P. S., and Hawlader M. N. A., 2011, “An active cooling system for photovoltaic modules,” Applied Energy, 90(1), pp. 309-315.

[39] Shahsavar A., and Ameri M., 2010, “Experimental investigation and modeling of a direct-coupled PV/T air collector,” Solar Energy, 84(11), pp. 1938-1958.

[40] Tiwari A., Sodha M., Chandra A., and Joshi J., 2006, “Performance evaluation of photovoltaic thermal solar air collector for composite climate of India,” Solar Energy Materials and Solar Cells, 90(2), pp. 175-189.

[41] Huang B. J., Lin T. H., Hung W. C., and Sun F. S., 2001, “Performance evaluation of solar photovoltaic / thermal systems,” Solar Energy, 70(5), pp. 443-448.

[42] Tonui J., and Tripanagnostopoulos Y., 2007, “Air-cooled PV/T solar collectors with low cost performance improvements,” Solar Energy, 81(4), pp. 498-511.

[43] Tonui J., and Tripanagnostopoulos Y., 2007, “Improved PV/T solar collectors with heat extraction by forced or natural air circulation,” Renewable Energy, 32(4), pp. 623-637.

[44] Tiwari A., and Sodha M. S., 2006, “Performance evaluation of solar PV/T system: An experimental validation,” Solar Energy, 80(7), pp. 751-759.

[45] Sarhaddi F., Farahat S., Ajam H., Behzadmehr A., and Mahdavi Adeli M., 2010, “An improved thermal and electrical model for a solar photovoltaic thermal (PV/T) air collector,” Applied Energy, 87(7), pp. 2328-2339.

[46] Joshi A. S., Tiwari A., Tiwari G. N., Dincer I., and Reddy B. V., 2009, “Performance evaluation of a hybrid photovoltaic thermal (PV / T) (glass-to-glass) system,” International Journal of Thermal Sciences, 48(1), pp. 154-164.

[47] Dubey S., and Tiwari G. N., 2008, “Thermal modeling of a combined system of photovoltaic thermal (PV/T) solar water heater,” Solar Energy, 82(7), pp. 602-612.

[48] Dubey S., and Tiwari G. N., 2009, “Analysis of PV / T flat plate water collectors connected in series,” Solar Energy, 83(9), pp. 1485-1498.

[49] Kalogirou S. A., 2001, “Use of TRNSYS for modelling and simulation of a hybrid pv – thermal solar system for Cyprus,” Renewable Energy, 23, pp. 247-260.

[50] Zondag H. A., Vries D. W. de, Helden W. G. J. van, Zolingen R. J. C. van, and Steenhoven A. A. van, 2002, “The thermal and electrical yield of a pv-thermal collector,” Solar Energy, 72(2), pp. 113-128.

[51] Charalambous P., Maidment G., Kalogirou S., and Yiakoumetti K., 2007, “Photovoltaic thermal (PV/T) collectors: A review,” Applied Thermal Engineering, 27(2-3), pp. 275-286.

[52] Zondag H., 2008, “Flat-plate PV-Thermal collectors and systems: A review,” Renewable and Sustainable Energy Reviews, 12(4), pp. 891-959.

[53] Ibrahim A., Othman M. Y., Ruslan M. H., Mat S., and Sopian K., 2011, “Recent advances in flat plate photovoltaic / thermal (PV / T) solar collectors,” Renewable and Sustainable Energy Reviews, 15(1), pp. 352-365.

[54] Othman M. Y. H., Yatim B., Sopian K., and Abu Bakar M., 2005, “Performance analysis of a double-pass photovoltaic/thermal (PV/T) solar collector with CPC and fins,” Renewable Energy, 30(13), pp. 2005-2017.

[55] Coventry J., 2005, “Performance of a concentrating photovoltaic/thermal solar collector,” Solar Energy, 78(2), pp. 211-222.

[56] Royne A., Dey C., and Mills D., 2005, “Cooling of photovoltaic cells under concentrated illumination: a critical review,” Solar Energy Materials and Solar Cells, 86(4), pp. 451-483.

[57] Eitner U., Altermatt P. P., Köntges M., Meyer R., and Brendel R., 2008, “A modeling approach to the optimization of interconnects for back contact cells by thermomechanical simulations of photovoltaic modules,” 23rd European Photovoltaic Solar Energy Conference, Valencia, Spain, pp. 258-260.

[58] Gonzalez M., Govaerts J., Labie R., Wolf I. De, and Baert K., 2011, “Thermo-mechanical challenges of advanced solar cell modules,” 12th. Int. Conf on Thermal, Mechanical and Multiphysics Simulation and Experiments in Microelectronics and Microsystems, EuroSimE 2011, pp. 1-7.

[59] Meuwissen M., Nieuwenhof M. V. D., and Steijvers H., 2006, "Simulation assisted design of a PV module incorporating electrically conductive adhesive interconnects," 21st European Photovoltaic Solar Energy Conference and Exhibition,, Dresden, Germany, pp. 2485-2490.

[60] Dietrich S., Pander M., Sander M., Schulze S. H., and Ebert M., 2010, "Mechanical and thermomechanical assessment of encapsulated solar cells by finite-element-simulation," Reliability of Photovoltaic Cells, Modules, Components, and Systems III, N.G. Dhere, J.H. Wohlgemuth, and K. Lynn, eds., SPIE, pp. 77730F1-10.

[61] Eitner U., Kajari-schroder S., Marc K., and Altenbach H., 2011, "Thermal Stress and Strain of Solar Cells in PhotovoltaicModules," Shell-like Structures, H. Altenbach, and V.A. Eremeyev, eds., Springer Berlin Heidelberg, Berlin, Heidelberg, pp. 453-468.

[62] Marion B., 2008, "Comparison of predictive models for photovoltaic module performance," Photovoltaic Specialists Conference, 2008. PVSC'08. 33rd IEEE, IEEE, pp. 1–6.

[63] Duffie J. A., and Beckman W. A., 1991, Solar Engineering of thermal processes, John Wiley & Sons, Inc., New York.

[64] Nelder J. A., and Mead R., 1965, "A simplex method for function minimization," The Computer Journal, 7(4), pp. 308-311.

[65] Masi M., Fogliani S., and Carra S., 1999, "Sensitivity Analysis on Indium Phosphide Liquid Encapsulated Czochralski Growth," Crystal Research and Technology, 34(9), pp. 1157-1167.

[66] Duffie J. A., and Beckman W. A., 2006, Solar Engineering of thermal processes, John Wiley & Sons, Inc., Hoboken, New Jersey.

[67] "Florida Solar Energy Center PV Performance Database." Available at: http://www.logger.fsec.ucf.edu/cgi-bin/wg40.exe?user=pvgroup [Accessed November 10, 2010].

[68] Incropera F. P., and DeWitt D. P., 1996, Fundamentals of Heat and Mass Transfer, John Wiley & Sons, Inc.

[69] Wilcox D. C., 1998, Turbulence Modeling for CFD, DCW Industries.

[70] "Wolfram Mathematica Weather Data." Available at: http://www.wolframalpha.com/input/?i=wind+speed+tallahassee+florida+may+15+2005 [Accessed September 28, 2011].

[71] Bahrami M., Yovanovich M. M., and Marotta E. E., 2006, "Thermal Joint Resistance of Polymer-Metal Rough Interfaces," Journal of Electronic Packaging, 128(1), pp. 23-29.

[72] Yilbas B. S., Arif A. F. M., and Abdul Aleem B. J., 2010, "Laser welding of low carbon steel and thermal stress analysis," Optics & Laser Technology, 42(5), pp. 760-768.

[73] Wilson K., Ceuster D. De, and Sinton R. A., 2006, "Measuring the effect of cell mismatch on module output," Photovoltaic Energy Conversion, Conference Record of the 2006 IEEE 4th World Conference on, IEEE, pp. 916–919.

[74] Ramos-Alvarado B., Li P., Liu H., and Hernandez-Guerrero A., 2011, "CFD study of liquid-cooled heat sinks with microchannel flow field configurations for electronics, fuel cells, and concentrated solar cells," Applied Thermal Engineering, 31(14-15), pp. 2494-2507.

VITAE

Name: Muhammad Usama Siddiqui

Date of Birth: August 9, 1985

Present Address: KFUPM P. O. Box 8642, King Fahd University of Petroleum and Mineral, Dhahran-31261, Saudi Arabia

Permanent Address: H. No. 129/3, Street 22, Model Colony, Karachi-75100, Pakistan

Email Address: musiddiqui@kfupm.edu.sa
musiddiqui@gmail.com

Educational Qualification:

M.S (Mechanical Engineering)
December, 2011
King Fahd University of Petroleum & Minerals,
Dhahran, Saudi Arabia.

B.E. (Mechanical Engineering)
June, 2008
National University of Sciences & Technology,
Karachi, Pakistan.